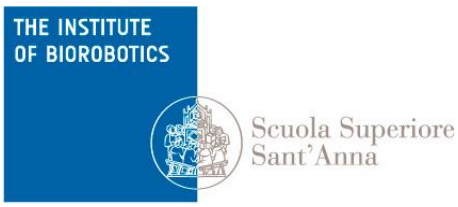

The BioRobotics Institute – Scuola Superiore Sant'Anna

PhD Programme in BioRobotics

Controlled ultrasound exposure for innovative therapeutic applications

PhD Candidate: ***Andrea Cafarelli***

Tutor: ***Prof. Arianna Menciassi***

Supervisor: ***Dr. Leonardo Ricotti***

XXIX Doctoral Cycle

June 21st, 2017

Summary

1 Motivation of the work

Medical technology paradigms continuously evolved in the last decades, leading towards more and more effective therapeutic solutions [1]. Recent efforts have been focused on personalized treatments that selectively and efficiently target specific pathological areas, thus minimizing side effects on healthy tissues. Minimally invasive procedures [2] have been developed in this regards. Such procedures are continuously being developed and are rapidly gaining acceptance in the clinics, especially when controllability is produced by robot-assisted methods [3].

The epitome of minimally invasive procedures consists of delivering the therapy in a completely non-invasive manner, *e.g*. by means of **therapeutic ultrasound**.

Ultrasound (US) based therapeutic tools consist of a non-invasive exposure of a non-ionizing, mechanical energy deep within the body without harming the healthy tissues. US can completely overturn the paradigms of current medicine and surgical interventions. Considering cancer treatment, for example, there are nowadays three main approaches, namely: chemotherapy, surgery and radiation therapy. However, none of these solutions can be considered free of side effects, such as non-specific targeting treatment, invasive incisions and use of ionizing radiation, respectively.

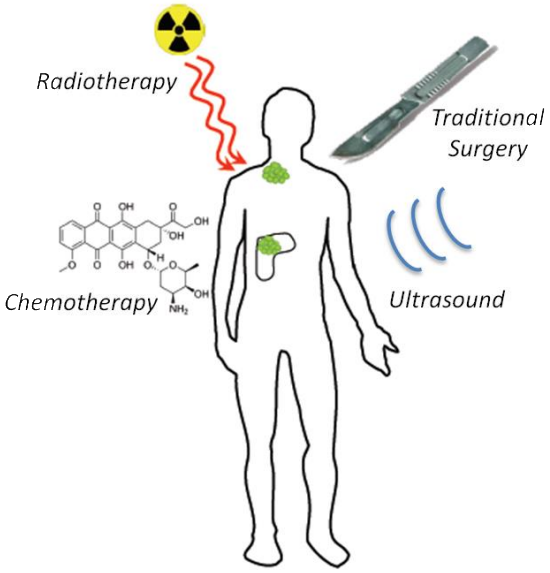

Figure 1.1. *Schematic representation of the three current main pillars in fighting cancer: chemotherapy, surgery and radiation therapy. The emerging technology of therapeutic US is also represented. Figure adapted from the lecture of Prof. Holger Grüll at the Winter School on Therapeutic Ultrasound 2015.*

Image-guided Focused Ultrasound (FUS) has the potential to guarantee a totally non-invasive treatment. This can concern ablative procedures, or a method to delivery drugs in a localized area in the body, hence avoiding standard systemic administration of chemotherapeutic drugs. Treatments can be performed with the US source external to the patient, without ionizing radiation, general anesthesia, incisions or scars, thus resulting in minimal pain, short recovery time and fewer complications compared with conventional surgery or radiation therapy [4].

While several medical applications of therapeutic US have been clinically demonstrated (*www.fusfoundation.org*, Figure 5.3), the underlying mechanisms of the interaction between **US and cells**, **US and tissues** and **US and materials** are often not well understood, yet.

Therefore, research efforts have been devoted to both *in vitro* and *in vivo* tests aimed at better understanding the correlation between the cause (US stimulation) and the effect (biological or material response). The major open problems, which hamper further development and impact of therapies based on US, can be summarized as follows:

1) ***Optimization of acoustic stimulation***. Many efforts still have to be made in this direction, in order to optimize treatments by providing the correct US dose at the target that causes the desired biological effect.

2) ***Understanding the influence of interactions between US-cells, US-tissue and US-materials*****.** Understanding such interactions occurring between acoustic energy, cells, tissues and materials, can lead to the achievement of the desired physical effect (thermal, mechanical, etc.) and the resulting bioeffect, hence improving US-based interventions. Such knowledge is largely missing at present. On the other hand, it is also crucial to improve treatments safety and efficiency, as well as to devise future therapies based on analogue paradigms.

3) ***Measuring and reporting of US exposure conditions*****.** The use of smart experimental systems, an accurate measurement system of the US field and an

accurate reporting of the data is a time-consuming and not always easy task. However it is of fundamental importance. Such systems could speed up a wider diffusion of therapeutic US among researchers and physicians.

4) ***Formulation of US-responsive materials***. Further research and technical efforts will be needed to achieve suitable materials, with finely tuned physio-chemical properties and responsiveness, thus allowing proper response to an US stimulation (*e.g.* drug delivery vectors, US responsive piezoelectric nanocomposites).

As briefly highlighted in point 3), unfortunately many users and researches in this field exploit US by using non standardized configurations both *in vitro* and *in vivo* conditions, vulnerable to errors during calibration and use [5]. Therefore, the results available in the state-of-the-art are hardly comparable, slowing down the progress of this technology.

Any attempt to determine a quantitative relationship between US exposure and observed effect, in fact, should be based on reliable measurements of the US field that is used and on a proper design of the test bench [6].

The work which led to the preparation of this document was based on, and driven by, these considerations.

All the activities described in this manuscript, dealing with different aspects of therapeutic US (Effects mediated by acoustically tuned and responsible materials in *Chapter* 3, Low Intensity Pulsed Ultrasound for regenerative medicine in *Chapter 4*, High Intensity Focused Ultrasound for cancer treatment in *Chapter 5* and Ultrasound-induced Blood Brain Barrier opening in *Chapter* 6) were investigated from an engineering point of view, trying to follow the same scientific approach and the aforementioned considerations.

1.1 Thesis outline

The contents of this PhD thesis are organized as follows.

In Chapter 2 Therapeutic Ultrasound is introduced, with a brief mathematical presentation of wave propagation and a delineation of the main parameters describing both propagation and interaction of US through tissue (Section 2.1). In Section 2.2 the main physical effects (thermal and mechanical) induced by US on tissues are described, focusing on the associated biological effects and the clinical indications where these phenomena can be exploited. Section 2.3 reports a best practice approach for studying and reporting exposure conditions used in therapeutic US studies for a wider and more rapid diffusion of therapeutic US application in clinics. This approach was then used for the studies conducted and described in the next chapters.

Chapter 3 describes the acoustic characterization of different materials and how this knowledge can be used to build tissue-mimicking phantoms which exhibit analogue echogenicity to real tissues for US-based medical procedures and to estimate the real US dose delivered to the target (*i.e.* cells exposed to US during *in vitro* experiments). First, in Section 3.1 the relevance in developing biomaterials with tuned acoustic - and mechanical - properties with a focus on agarose, polyacrylamide and polydimethylsiloxane is reported. The experimental set-up used to measure acoustic properties of these materials is detailed in Section 3.2, while the development of custom tissue-mimicking phantoms and smart materials (*e.g.* piezoelectric nanocomposites) for stimulating cells with a highly controlled US dose are reported in Section 3.3 and Section 3.4, respectively.

In Chapter 4 an experimental system for in vitro cell stimulation is described. After exploring the state of the art of Low Intensity Pulsed Ultrasound (LIPUS) stimulation (Section 4.1), the characterization of the US field in terms of pressure field maps and intensity of each transducer at several frequencies of interest (Section 4.2) are presented. The consequent system design is also reported (Section 4.3). The system was exploited to investigate the effects of controlled LIPUS exposures at different frequencies and intensities, on C2C12 muscle cells (Section 4.4).

Chapter 5 is devoted to High Intensity Focused Ultrasound (HIFU) surgery for cancer treatment. An innovative robotic system that merges HIFU technology with US guidance and robotic control is described (Section 5.2), after briefly exploring the main principles of HIFU and highlighting the main limitations of current systems (Section 5.1). A 16 channels annular array transducer has been integrated in the platform, properly characterized (Section 5.3) and exploited for an *in vivo* and *ex vivo* validation of the procedure both in static and dynamic conditions (Section 5.4).

Chapter 6 reports the results of a six-month experience at the Neurospin Lab (Commissariat à l'énergie atomique, Saclay, France) where a controlled US exposure was used *in vivo* for a safe permeabilization of the Blood Brain Barrier (BBB) has been used. After exploring the state of the art of FUS-induced BBB opening (Section 6.1) a procedure for a safe and effective transient BBB permeabilization based on passive cavitation on rats is presented (Section 6.2). Results are reported in Section 6.3.

Finally, Chapter 7 reports the conclusions of the work, the achieved objectives and the future perspectives.

2 Introduction to Therapeutic Ultrasound

Besides the well-known use of US in diagnostics, the use of US as therapeutic tool has recently emerged. Thanks to its intrinsic non-invasive nature (no incisions and no ionizing radiation) and the capability to localize the effects of a treatment with extreme precision (use of a focused beam), therapeutic US is rapidly gaining clinical acceptance for a wide range of pathologies.

However, there are a number of challenges to overcome which obstruct the widespread development of applications of therapeutic US in clinics. Examples range from an accurate knowledge of the underlying mechanisms to treatment optimization and safety issues.

In this Chapter the basic physical principles of US are introduced in Section 2.1 with a brief mathematical introduction of elastic wave propagation and a delineation of the main parameters useful to describe the propagation of US through tissue. In Section 2.2 the main physical effects, *i.e.* thermal and mechanical effects, induced by US propagation in tissues are described, paying particular attention to the associated biological effects. The clinical indications where these phenomena can be exploited are also described. Section 2.3 reports a best practice approach for studying and reporting exposure conditions used in therapeutic US studies for a wider and more rapid diffusion of therapeutic US applications in clinics.

2.1 Physical principles of medical ultrasound

US waves are mechanical vibrations that propagate through a medium with frequencies higher than 20 kHz (upper limit of the human hearing range). Unlike electromagnetic waves, which can propagate in vacuum, sound and US waves need a medium to propagate.

Even though a thorough mathematical description of US propagation is far from the main aim of this work, the basic definitions of acoustic waves are described as follows for the sake of completeness.

The simplest starting point to analytically describe the propagation of a pressure wave is by considering the medium stationary [7]. When a stable state is perturbed by a propagating acoustic wave, the total pressure p_T, at the position x and time t, can be written as follows:

$$p_T(x,t) = p_0 + p(x,t) \qquad \text{Eq. 2.1}$$

where the subscript *0* denotes an unperturbed condition. An analogous equation can also be written for the density of the medium ρ_T.

The wave equation can be derived from the continuity equation, the momentum equation, considering the approximation of small perturbations ($p/p_0 \ll 1$ and $\rho/\rho_0 \ll 1$) and the constitutive equation which relates p and ρ:

$$\begin{cases} -\frac{\partial \rho}{\partial t} = \rho_0 \frac{\partial u}{\partial x} \\ -\frac{\partial p}{\partial x} = \rho_0 \frac{\partial u}{\partial t} \\ \rho = \rho_0 \beta_0 p = \left[\frac{\partial \rho}{\partial p}\right]_{ad} \end{cases} \qquad \text{Eq. 2.2}$$

where u is the particle velocity and the subscript *ad* indicates an adiabatic transformation (β_0 is the adiabatic compressibility).

Combining the three equations described in Eq. 2.2 the wave equation can be derived:

$$\frac{\partial^2 p}{\partial x^2} - \frac{1}{c^2}\frac{\partial^2 p}{\partial t^2} = \left(\frac{\partial}{\partial x}\log \rho_0\right)\frac{\partial p}{\partial x} \qquad \text{Eq. 2.3}$$

where *c* is the speed of sound in the medium. Assuming constant density and compressibility and a homogeneous medium Eq. 2.3 simplifies as follows:

$$\nabla^2 p - \frac{1}{c^2}\frac{\partial^2 p}{\partial t^2} = 0 \qquad \text{Eq. 2.4}$$

In the case of harmonic wave it is possible to express all the variables using complex notation ($A=A_\omega \cdot e^{i\omega t}$) where $\omega=2\pi f$ is the angular frequency at the frequency *f* in a time-independent expression:

$$\nabla^2 p_\omega + \frac{\omega^2}{c^2} p_\omega = 0 \qquad \text{Eq. 2.5}$$

A travelling acoustic wave transports energy, which can be calculated by the scalar product of the momentum equation and the particle velocity. Using Eq. 2.4 it is possible to obtain the relation:

$$\nabla(pu) = -\left(\frac{1}{2}\frac{\partial u^2}{\partial t} + \frac{p}{\rho_0 c^2}\frac{\partial p}{\partial t}\right) \qquad \text{Eq. 2.6}$$

Eq. 2.6 implies that the flux of energy density is equal to the variation of the kinetic energy and the potential energy (first and second term on the right hand side of the equation respectively). The time variation can be eliminated by performing a time average, thus introducing the Intensity *I(t)*, a very important parameter for medical US and their effect on tissue.

$$I(t) = \frac{1}{\tau}\int_0^\tau (p(t)u(t))dt \qquad \text{Eq. 2.7}$$

Assuming linear wave approximation, Eq 2.7 simplifies as follows:

$$I = \frac{p^2}{\rho_0 c} \qquad \text{Eq. 2.8}$$

By using the local maximum pressure value, the corresponding intensity is called spatial peak temporal-peak intensity (I_{SPTP}). Combination of spatial and time averages provides further definitions. Some examples are the spatial-average time-average intensity (I_{SATA}) and spatial-peak time-average intensity (I_{SPTA}). When referring to

pulsed waves, pulse-average values are also introduced, namely the spatial-peak pulse-average intensity (I_{SPPA}) and the spatial-average pulse-average intensity (I_{SAPA}).

PPP and *PNP* respectively denote the Peaks of Positive and Negative Pressure in Figure 2.1. $1/t$ is the US wave frequency (f), T_P is the pulse length and T is the pulse repetition period; its reciprocal $1/T$ is known as Pulse Repetition Frequency (*PRF*). Duty cycle (*DC*) is defined as T_P/T.

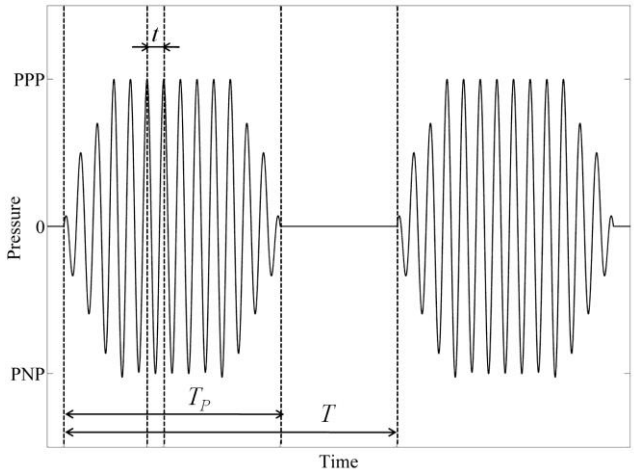

Figure 2.1. *Typical shape of an ultrasonic wave with some parameters highlighted.*

2.1.1 Transmission/reflection between different interfaces

The acoustic impedance (Z) is another important acoustic parameter that needs to be introduced. The concept of impedance is particularly valuable in characterizing wave propagation in the presence of boundaries between media with differing acoustical properties. The simplest case is that of the propagation of a plane wave in an inviscid fluid medium, where the acoustic impedance can be simply expressed as:

$$Z = \rho c \qquad \text{Eq. 2.9}$$

Whenever an ultrasonic wave front of energy E hits a boundary between two media characterized by different acoustic impedances (Z_1 and Z_2) only a part of the wave is transmitted through to the second medium, while a fraction is reflected.

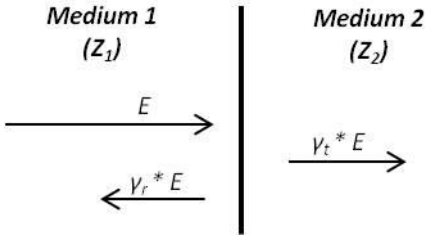

Figure 2.2. *Typical transmission and reflection phenomena at the interface between two materials with different acoustic impedance.*

The reflection coefficient γ_r is given by the following equation:

$$\gamma_r = \left(\frac{Z_1 - Z_2}{Z_1 + Z_2} \right)^2 \qquad \text{Eq. 2.10}$$

while the transmission coefficient γ_t can be expressed as follows:

$$\gamma_t = \frac{4Z_1 Z_2}{(Z_1 + Z_2)^2} \qquad \text{Eq. 2.11}$$

It is therefore clear that if acoustic impedances at one interface are equal, the transmitted intensity is equal to the incident intensity and there is no echo. If instead there is a large difference between them, there will be nearly total reflection, for example at the air-soft tissue interface. Typical reflection percentage intensities at the interface between some tissues are reported in Table 2.1.

Boundary	% Reflection
Muscle / Fat	0,5
Kidney / Fat	0,6
Soft tissue / Water	0,2
Bone / Muscle	41
Bone / Fat	49
Soft tissue / Air	99,9
Kidney / Fat	1

Table 2.1. *Percentage reflection of US at boundaries*

2.1.2 Attenuation

Attenuation is another important parameter to be considered when studying the propagation of US waves through tissues. When a pressure wave passes through a medium, particles are forced to move with respect to each other. The medium viscosity opposes this motion and part of the wave energy is converted into heat. The

conversion in turn causes the intensity and the pressure of the wave to decay, with the following exponential relation:

$$I = I_0 e^{-\mu x} \qquad p = p_0 e^{-\alpha x} \qquad \text{Eq. 2.12}$$

where μ is the attenuation coefficient and in the linear approximation it is related to α by a factor 2. Attenuation coefficient is the sum of the absorption coefficient and the scattering coefficient. The total loss of acoustic energy due to the wave travelling inside a tissue is therefore given by different factors: refraction, reflection, scattering and absorption. For a first approximation, however, absorption is the highest contribution and it is common to consider that all the energy loss is absorbed by the medium.

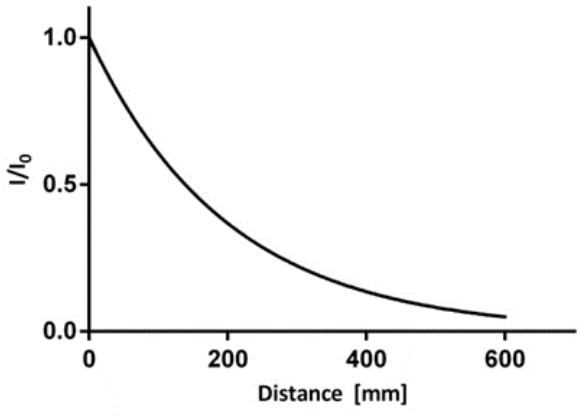

Figure 2.3. *Example of the effect of attenuation on US intensity in relation to the depth in the body. I_0 is the original intensity.*

Furthermore it is worth mentioning that the attenuation is related to frequency, expressed by the equation, where the exponent *b* is commonly between 1 and 2.

$$\mu = af^b \qquad \text{Eq. 2.13}$$

2.1.3 Main acoustic properties of natural tissues

In Table 2.2 the main acoustic (and mechanical) properties of some human tissues are reported. The knowledge of these properties is extremely important to predict, by using the before-mentioned equations, the propagation of US inside the body and therefore precisely control the dose at the target site. This knowledge, as will be

explained in Chapter 3, is also important in the development of US phantoms which show analogue echogenicity of real tissues.

Tissue	Young's Modulus [kPa]	Density [kg/m^3]	Speed of Sound [m/s]	Acoustic Impedance [MRayl]	Attenuation Coefficient [dB/(cm MHz)]
Blood	/	1060	1584	1.68	0.2
Brain	1-4	1040	1560	1.62	0.6
Breast	1-3	1020	1510	1.54	0.75
Cardiac	10-15	1060	1576	1.67	0.52
Fat	0.5-3	950	1478	1.40	0.48
Liver	8-12	1060	1595	1.69	0.50
Diseased Liver	6-25	1050	1527	1.60	0.58
Marrow	0.5-1.5	/	1435	/	0.5
Muscle	10-20	1050	1547	1.62	1.09
Tendon	1300-1700	1670	1750	1.84	4.7
Air	/	1.2	330	0.0004	/
Water	/	1000	1480	1.48	0.0022

Table 2.2. *Acoustic and mechanical properties of some human tissues.*

2.2 Physical effects, biological effects and clinical indications of therapeutic ultrasound

When an US wave interacts with biological tissues, there are mainly two different physical effects as a result: thermal and mechanical effects. These effects depend on the nature of the tissue (attenuation coefficient, percentage of gas, etc.) and the US parameters (intensity, therapy duration, duty cycle, etc.). If correctly tuned, this interaction can produce certain desired biological effects that can be exploited in many clinical indication.

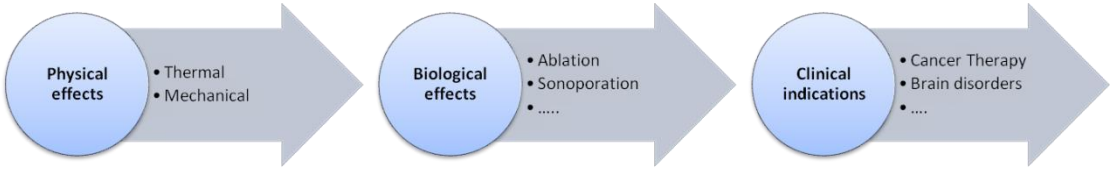

Figure 2.4. *US-tissue interaction. The direct application of US can cause mainly two different physical effects within the tissues: thermal and mechanical ones. If correctly tuned, these mechanisms produce multiple biological effects that enable the potential use of US in many clinical indications.*

As reported in a recent FUS Foundation's white paper [8], focused US is capable of inducing 17 different biological effects that highlights the potential use of US for treating different pathologies.

APPLICATION	RATE OF ENERGY DEPOSITION	ENERGY INTENSITY	MECHANISM	BIOLOGICAL EFFECT
Thermal ablation	Continuous	High	Hyperthermia (high)	Coagulative necrosis
Physiotherapy	Pulsed/Continous	Low	Cavitation (stable) / Hyperthermia (low)	Tissue repair enhancement
Histotripsy	Pulsed	High	Cavitation (inertial)	Destruction of cell membrane
Clot lysis	Pulsed	High	Cavitation (inertial)	Disruption of the fibrin matrix
Sonodynamic therapy	Pulsed	High	Cavitation (inertial)	Formation of ROS (reactive oxygen species)
Radiosensitization	Continuous	Low	Hyperthermia (low)	Prevents DNA repair
Neuromodulation	Pulsed	Low	Mechanical	Neurons excitation or inhibition
Blood-brain barrier opening	Pulsed	Low	Cavitation (stable)	Disruption of tight junctions
Immunomodulation	Continuous or pulsed	High	Mechanical or thermal (low)	Presentation of tumor-specific antigens and cytokine secretion
Enhanced drug uptake	Pulsed	Low	Cavitation (stable)	Sonoporation
Drug delivery from vehicles	Pulsed or Continous	Low	Cavitation or hyperthermia	Drug delivery from vectors

Table 2.3. *Main therapeutic applications of US.*

Cancer treatment, in particular, has become a major area of interest [9], but clinical applications of therapeutic US includes other procedures such as lithotripsy, thrombolysis, targeted US drug delivery, transdermal US drug delivery, and US hemostasis [10].

2.2.1 Thermal and mechanical effects on tissues induced by US

The thermal and mechanical effects of US are detailed in this section.

Thermal effects.

Thermal effects are associated with a absorption of part of the energy carried by the US wave in the tissue. As anticipated by Eq. 2.12, while US wave travels in a viscous medium, it loses part of its energy. In the absence of heat losses by conduction, convection or radiation, it is possible to relate the heat deposition rate per unit volume to the US intensity and the temperature variation as follows:

$$\dot{Q} = \mu I = \rho C \frac{\partial T}{\partial t} \qquad \text{Eq. 2.14}$$

where *C* is the heat capacity of the medium. In practical cases, at least diffusion and cooling must be considered. The well-known Pennes' bio-heat equation takes into account the conduction heat transfer and the cooling from blood vessels which act as heat exchanger [11]:

$$\rho C \frac{\partial T}{\partial t} = \nabla(k\, \nabla T) - m_b C_b (T - T_b) + \mu I \qquad \text{Eq. 2.15}$$

where *k* is the thermal diffusivity, subscript *b* indicates blood and *m* is the blood mass in the considered region. The thermal tissue damage caused by US depends on a number of factors, related to acoustic tissue properties and acoustic parameters of the stimulation. The overall thermal effect is mainly dependent on a combination of temperature increment and duration of heating. Sapareto and Dewey [12] proposed the cumulative equivalent minutes at 43°C (CEM_{43}) as a model to calculate the thermal dose from the knowledge of temperature history:

$$CEM_{43} = \int_{t_0}^{t_f} R^{(43-T)} \partial t \qquad \text{Eq. 2.16}$$

where $R = 0.25$ for $T \leq 43°C$ and $R = 0.5$ for $T > 43°C$. The commonly accepted threshold for tissue thermal ablation (thermal ablation) is 240 CEM_{43}, although there is

some variation based on the tissue type. Figure 2.5 shows different levels of thermal dose and their biological effects.

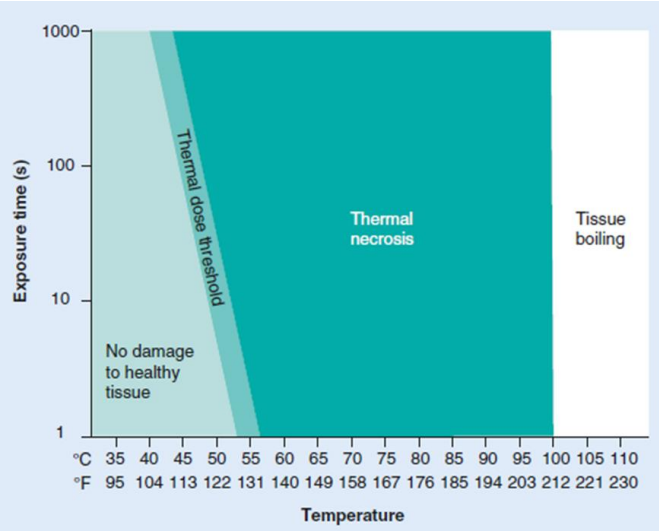

Figure 2.5. *Correlation between thermal dose and biological effects in tissues [4]. Thermal effects are mainly dependent on a combination of temperature elevation and duration of heating. Below the thermal dose threshold, no tissue damage occurs; beyond the threshold tissue experiences thermal necrosis. Tissue boiling occurs over 100°C regardless the exposure time.*

The Thermal Index (*ThI*), which is defined as the ratio between the transducer output power (W_p) and the power required to raise the tissue temperature by 1 °C (W_{deg}), provides a simplified way to estimate the temperature rise in tissue during exposure.

$$ThI = \frac{W_p}{W_{deg}} \qquad \text{Eq. 2.17}$$

Mechanical effects

Among mechanical effects induced by US on tissues, the most common effects relate due to radiation force, acoustic streaming and **acoustic cavitation**. This last phenomenon involves the formation, oscillation, growth, and possible collapse of gas bubbles within the tissues.

The dynamics of a single spherical bubble in a free liquid field can be described by a simplified model (Rayleigh-Plesset equation [13]) as follows:

$$R\ddot{R} + \frac{3}{2}\dot{R}^2 = \frac{1}{\rho}\left[P_g - P_0 - P(t) - 4k\frac{\dot{R}}{R} - \frac{2\tau}{R}\right] \qquad \text{Eq. 2.18}$$

where *R* is the radius of the bubble, P_g is the gas pressure inside the bubble, P_0 is the static pressure in the liquid just outside the bubble wall, *P(t)* the applied driving pressure, τ is the surface tension and *k* the kinematic viscosity.

Two different cavitation regimes can be identified, bringing about different bubble dynamics [7]:

- ***stable (non-inertial) cavitation***, which is characterized by small and harmonic oscillation of the bubble radius around its equilibrium position, in response to a relatively low intensity pressure field;

- ***transient (inertial) cavitation***, which is characterized by strongly nonlinear oscillations leading to collapse in response to higher intensities. The violent collapse of bubbles can generate a local pressure of about 500 atm, a local temperature as high as 5000 K and a very strong shock wave and microstreaming [14].

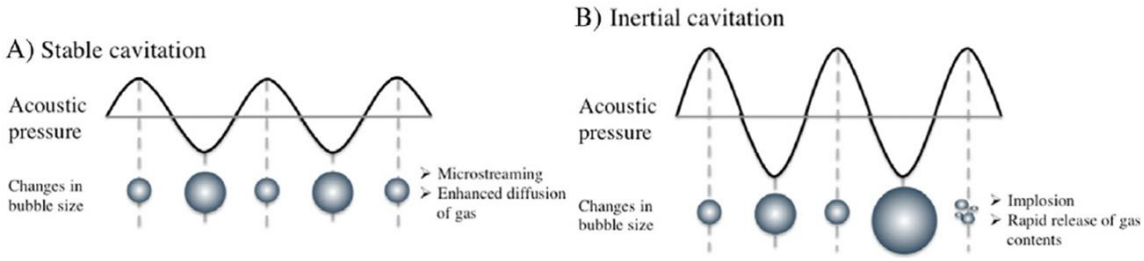

Figure 2.6. *Mechanism of acoustic cavitation: A) Stable caviation regime and B) Inertial cavitation regime. Figure readapted from Fix et al. [15].*

The Mechanical Index (*MI*), although represents a relative indicator of the likelihood of mechanical bioeffects, gives an indication of mechanical damage of tissue due to inertial cavitation. The mechanical index is defined as the ratio between the maximum value of peak negative pressure (P_{neg}) and the square root of the nominal frequency (*f*) of the acoustic beam.

$$MI = \frac{max\{P_{neg}\}}{\sqrt{f}} \qquad \text{Eq. 2.19}$$

Although there are several limitations to the use of the *MI* in certain applications, this number has been generally adopted as a safety index for medical US systems. It is now accepted that with *MI < 0.3* the probability that mechanical bioeffects occur is very low [16], while for *MI > 0.7* the risk of inertial cavitation events is very high [17].

2.2.2 A possible classification of therapeutic ultrasound

From an engineering viewpoint, a possible classification can be made by distinguishing applications in which US are used alone (direct effect on tissues) or in combination with US responsive agents (mediated effects on tissue). Considering destructive and non-destructive applications as well, four different categories can be therefore highlighted:

1. ***Stand-alone US for tissue destruction****:* High Intensity Focused Ultrasound (HIFU) concentrates a large amount of energy in a small target volume deep in the body without harming the surrounding healthy tissue. A significant temperature rise (thermal ablation) and/or mechanical phenomena (inertial cavitation) can therefore cause tissue necrosis only in the focus area (protein denaturation [18] and histotripsy [19], respectively). This principle is mainly applied for treating malignancies such as breast, prostate, liver, kidney and bone tumors [9] or uterine fibroids [20], but it is recently gaining acceptance also for thrombolysis [21], brain tumours [22] and other neurological diseases [23].

   Also aesthetic applications in which inertial cavitation is exploited to selectively disrupt fat cells (lysis) play a major role in the therapeutic US market [24].

2. ***Stand-alone US for tissue modification:*** non lethal temperatures increase (39 to 42°C) in the range of moderate hyperthermia, far below the ablative threshold, can be induced by US to speed up the healing processes in physiotherapy applications [25] and for enhancing the efficacy of drug delivery

and uptake in targeted area. This is due to an increase of the blood flow and drug absorption in the target region [26].

Also non lethal mechanical effects can be exploited for physiotherapic and aesthetic applications (e.g. facial wrinkles treatment) [27] or to increase localized uptake of drugs in the body. Stable cavitation can modify the permeability of cell membranes, thus enhancing the absorption of drug molecules through the mechanism known as sonoporation [28] and increasing the vascular permeability at the target area [29].

Low intensity US can also be used for vasodilation and vasoconstriction in the vessels [30], stimulation or suppression of neural activity in US-induced neuromodulation applications [31], and enhancing sensitization to radiotherapy or chemotherapy [32] minimizing the treatment's adverse effects.

3. ***US in combination with US responsive materials for tissue destruction:*** specific vectors can be used in combination with US stimulation as HIFU enhancement tools for lethal thermal or mechanical effects. For example, the use of intravenously injected contranst agents (*e.g.* microbubbles (MB)) reduces the threshold level of inertial cavitation that results in mechanical tissue ablation, thus enhancing treatment efficiency and reducing the total time duration of cancer treatment [33]. Another example worth mentioning is sonothrombolysis, where the use of MB in combination with focused US is established to enhance the lysis of clots that occlude blood vessels [34].

4. ***US in combination with US responsive materials for tissue modification:*** US contrast agents can be used in combination with US to enhance some non lethal biological phenomena. For example, the interaction between US and oscillating MB is widely investigated to overcome the natural barriers for a targeted drug delivery [35]. A particular attention in this field is dedicated to MB-assisted US for drug delivery in the brain, described in Chapter 6, that was

demonstrated to be an effective and safe method to momentarily open the blood brain barrier.

US can be used also as a trigger for the lethal or non-lethal drug release from specific micro/nano materials (*e.g.* MB, liposomes, polimeric micelles and nanobubbles) responsive to a certain ultrasonic regime [36]. Even if there are few examples of thermosensitive vectors designed to release drugs (*e.g.* thermo-sensitive micelles and temperature-sensitive liposomes), the main physical mechanisms used to trigger drug release from US-sensitive carriers are mechanical [37].

In addition, as will be explained in Section 3.4, it has been recently shown that piezoelectric nanomaterials stimulated by US can provide beneficial stimuli for the differentiation/regeneration of cells and tissues [38].

2.3 Controlled ultrasound exposure and the problem of reporting exposure conditions

In any study that attempts to show a quantitative relationship between US exposure and the observed effect, the authors should measure or correctly estimate the exposure level in situ where the effects are observed and report it in a correct manner. In fact, a wrong reporting of the exposure conditions causes a considerable slowing down in the advancement of the understanding of the phenomena and its application to the clinical scenario. One of the main problems in the therapeutic US field to reproduce is in fact comparing and analysing data sets from different groups [39].

Moreover it is worth mentioning that the most common indices available in clinical devices, namely the Thermal Index (*TI*) and Mechanical Index (*MI*) described in Eq. 2.17 and Eq. 2.19, suffer from strong limitations. In 2011 Prof. ter Haar wrote a guideline for encouraging a best practice approach among researchers in the field of US for studying and reporting exposure conditions used in their studies [6]. The main recommendation is the following:

"Any study that attempts to demonstrate a correlation or lack of correlation between exposure to ultrasound and an observed or postulated physical or biological effect must include acoustic output data for each ultrasound field based on the maximum values in the field (Level 2) or, preferably, the acoustic pressure and intensity distributions (Level 3). Ideally, each field used should be measured but it is acceptable to measure a subset of the fields and determine the data for other fields by interpolation or, exceptionally, by extrapolation provided that the method is described. The need to make these measurements should be considered in the early planning stages of the study."

However, this is neither straightforward nor common in many studies. In fact, there is a huge variability in the devices and parameters used, in terms of temporal, spatial and intensity distribution that are often not properly considered. Both diagnostic and therapeutic US field often have a very high degree of spatial non uniformity thus requiring very difficult measurements for complete characterization. Furthermore, most off-the-shelf devices do not possess accurate description of their acoustic field since it is not an important information for the usual medical instrument. Of course this consideration is no longer valid if the same device is used as a research tool.

Even if there are a lot of instances in literature of studies seeking to correlate the observed effect in some way to the nature of US exposure, a good reporting practice is still not widespread in literature, bringing incomplete information, wrong assumptions and lack of reproducibility between different groups.

Another important issue is the design of the experimental system used for US experiments. As described more extensively in Chapter 3, inappropriate set-ups generate uncertainty in the exposure that for *in vitro* cell stimulation can exceed 700% [5]. For example, a vast majority of current systems used in this field use non-transparent materials (*e.g.* plastic Petri dishes) along the path of the US beam that reflect part of the energy and may produce some hardly predictable effects, such as standing wave formation.

All the activities described in this work, dealing with different applications of therapeutic US, were conducted taking into account these points. In particular, well-

characterized and reproducible systems for US studies were developed following the following steps:

1. ***Characterization of the US sources***: All the transducers used were characterized, for all frequencies under investigation, in terms of pressure field maps and intensity calibration, in free field conditions.

2. ***Design of the US stimulation set-up:*** The experimental set-ups were designed and built up trying to minimize the typical exposure errors that normally affect the vast majority of current systems used for US stimulation and to achieve an exposure as much as possible similar to the one measured in free field conditions. For this purpose, particular attention has been devoted to the knowledge of the acoustic properties of materials that interact with US waves in the stimulation path.

3. ***Report of the exposure conditions:*** The characteristics of the US sources, the experimental set-up features and the stimulation parameters (frequency, intensity, therapy duration, and duty cycle) have been carefully reported.

This aforementioned approach was applied to all the activities presented in this work based on the author's strong belief that an improvement in the knowledge of the biological effects of US, together with a smart experimental design and an appropriate reporting of the data, is fundamental for a wider diffusion of US therapies.

3 Acoustic characterization of materials

The knowledge of acoustic properties of materials such as speed of sound, acoustic impedance and attenuation coefficient is of great importance for any applications in which materials interact with acoustic or ultrasonic waves.

In particular an accurate knowledge of combination of acoustic and mechanical properties of materials is of great interest for both the development of tissue-mimicking phantoms for US tests and for the development of smart scaffolds for US mediated tissue engineering and regenerative medicine.

Regarding US phantoms, this knowledge can be used to build tissue-mimicking phantoms which show similar echogenicity to real tissues for US-based medical procedures and that can be used different purposes.

Furthermore, a proper knowledge of acoustic properties of materials allows to estimate the real US dose delivered to the target (*i.e.* cells exposed to US during *in vitro* experiments). As an example, in the field of therapeutic US for tissue engineering, scaffolds are commonly used to support cells during US stimulation experiments, both *in vitro* and *in vivo*. Therefore, whenever an acoustic wave interacts with materials positioned within the propagation path, the material acoustic properties deeply influence the US propagation due to attenuation or reflection and thus the US dose actually delivered to the target.

In Section 3.1 the relevance to develop materials with tuned acoustic - and mechanical - properties, with a focus on agarose (AG), polyacrylamide (PAA) and polydimethylsiloxane (PDMS), is reported.

The experimental system used to measure acoustic properties of materials is detailed and the results of acoustic and mechanical characterization of AG, PAA and PDMS at different concentrations and doped with different concentrations of nanoparticles (*i.e.* barium titanate nanoparticles) are reported in Section 3.2. These data were used to develop custom tissue-mimicking phantoms (Section 3.3) and to fabricate smart materials for stimulating cells with a highly controlled US dose (Section 3.4).

3.1 Tuned materials for ultrasound applications: agarose, polyacrylamide and polydimethylsiloxane

Tuning material physical properties is an effective way to engineer artificial or bioartificial systems for a wide range of biomedical applications. Materials with finely tuned features can indeed play a key role as synthetic replacements for biological tissues, substrates for tissue engineering, components of medical/surgical devices, drug delivery systems, diagnostic and array technologies and tissue-mimicking systems [40, 41]. In particular, material properties play a key role in two specific and rather distinct application domains, namely the development of tissue-mimicking phantoms for ultrasound (US) tests and the development of scaffolds for tissue engineering and regenerative medicine.

Tissue-mimicking phantoms are an important tool for performance testing and optimization of medical US systems and photoacoustic devices, as well as for medical training [42]. US phantoms must closely reflect the typical acoustic properties, such as speed of sound (c), acoustic impedance (Z) and attenuation coefficient (α) of natural tissues in order to reproduce US images similar to those obtained *in vivo* conditions.

US stimulation of cells and cell-seeded scaffolds has recently emerged as an intriguing tool to enhance certain cell responses in tissue engineering and regenerative medicine fields, by exploiting either direct mechanical effects [43, 44] or smart materials-based mediated ones [45, 46]. In this context, smart substrates can be defined as materials that are able to produce different types of stimuli (electrical, mechanical, thermal, chemical, etc.) and convey them to cells, once they are invested by a US wave.

Whenever an acoustic wave is used in combination with materials, their acoustic properties deeply influence the US attenuation or reflection and thus the US dose actually delivered to cells. Therefore, an accurate knowledge of the acoustic properties (such as c, Z and α) of different materials is extremely useful both for the development of tissue-mimicking US phantoms and for the estimation of the effective dose to cells in US mediated tissue engineering applications.

In this work the attention was focused on three polymers: agarose (AG), polyacrylamide (PAA) and polydimethylsiloxane (PDMS). These materials have been

extensively used in both tissue-mimicking phantoms and tissue engineering/regenerative medicine fields, but a systematic acoustic characterization has been not performed yet. The selected materials were characterized in terms of acoustic properties (*c*, *Z* and *α* measurements) at different concentrations or cross-linking levels and doped with different concentrations of barium titanate ceramic nanoparticles ($BaTiO_3$).

In the field of tissue-mimicking phantoms, several materials were designed and characterized to be used as tissue-mimicking materials (TMMs) with the aim to tailor acoustic properties of tissues for specific applications in US-related medical fields [41].

The use of PDMS in this domain implies several advantages including stability, long-term duration and the possibility to mimic elastic properties of different tissues, making this material a valid solution for US phantoms in general and for elastography in particular. PDMS phantoms can be useful for surgical training, to simulate procedures such as biopsies and needle insertions and also for the development of new diagnostic strategies. However, silicone-like materials are usually discarded as TMMs for US phantoms, due to their high *α* (usually >2 dB/cm), low *c* (around 1000 m/s) and low *Z* (around 1 MRayl) [47] that make them rather different from natural soft tissues [48]. For the RT601 silicone, Zell *et al.* found a longitudinal *c* of 1030 m/s, a *Z* of 1.10 MRayl and an *α* of 14 dB/cm (at 7MHz) [42]. In a study focused on the estimation of ultrasonic shear rate in vascular applications, Tsou *et al.* [49] reported the longitudinal *c* and the *α* of PDMS at different formulations. It was found that PDMS acoustic properties are very different from biological tissues, but they can be adjusted by changing the monomer/curing agent ratio (*e.g.* by changing the ratio from 1:10 to 1:5, the *c* increased from 1076,5 up to 1119.5 m/s and the α decreased from 21.30 down to 14.86 dB/cm, at 5 MHz).

PAA shows very good acoustic properties and an acceptable stability over time, thus making it a good solution for US phantoms. A 10% PAA gel was used by Zell *et al.* [42]. The measured *c* (1580 m/s), *Z* (1.7 MRayl) were within a suitable range for mimicking soft tissues, while α (0.7 dB/cm at 5 MHz) resulted lower with respect to values shown by natural tissues. Prokop *et al.* proposed PAA gels at different concentrations as

coupling media for FUS therapy [50]. Here, it was shown that acoustic properties varied linearly with acrylamyde concentration from 10% to 20% w/v: *c* ranged from 1546 to 1595 m/s, *Z* from 1.58 to 1.68 MRayl and α from 0.08 to 0.14 dB/cm, at 1 MHz.

PAA is also widely used for the fabrication of thermal phantoms, exploited, *e.g.*, in the evaluation of high intensity focused ultrasound (HIFU) procedures [51, 52]. In these studies, PAA is commonly mixed with a thermosensitive material, such as bovine serum albumin (BSA) or egg-white, in order to become optically opaque when denatured [53, 54].

As reported by Culjat *et al.*, AG-based materials are widely used for US phantoms, due to the ease of fabrication, good acoustic (and mechanical) properties and the possibility to easily incorporate additional ingredients [41]. Therefore, AG-based materials have been rather well characterized in the previous literature [55].

The main AG acoustic properties, which are anyhow strongly influenced by material formulation and manufacturing techniques, are the following: *c* in the range 1498–1600 m/s, α in the range 0.04–1.40 dB/cm and *Z* in the range 1.52–1.76 MRayls [56].

Cannon et al. developed AG-based materials for the production of a heterogeneous breast phantom, mimicking different anatomical structures of the breast (glandular tissue, subcutaneous fat, pectoral muscle, areola, malignant and benign lesions) under US [57]. In this study, the authors kept a constant concentration of AG (3% w/v) and modified the concentrations of different dopant agents (glycerol, silicon carbide and aluminum oxide) in order to slightly change the acoustic properties.

In addition to formulation, preparation conditions may play also an important role in determining the final properties of AG gels: Browne *et al.* found that AG *c* increases with increasing temperature by a rate of approximately 1.5 m s^{-1} $°C^{-1}$, while changes in α are negligible [58]; Ross and colleagues found that mixing conditions also strongly influence mechanical and acoustic properties of agar gels [59].

In the field of tissue engineering and regenerative medicine, PDMS, PAA and AG materials have been also extensively used, especially for mechanobiological studies. Substrate mechanical and (in some cases) surface chemical properties regulate in fact important cells behaviors such as adhesion, proliferation and differentiation [60-65].

Scaffolds are commonly used to support cells also during US stimulation experiments, both *in vitro* and *in vivo*. However, a proper knowledge of their acoustic properties is almost always lacking. This hampers to estimate the actual US dose delivered to the target and, as a consequence, makes US exposure poorly repeatable: it has been demonstrated that the uncertainty on US exposure, during *in vitro* experiments, can be up to 700% [5].

No insights on acoustic properties of PDMS, PAA and AG materials intended for the development of cells substrates were reported.

A systematic analysis of acoustic characterization of PDMS, AG, PAA at different concentrations and cross-linking extents and doped with different concentrations of barium titanate ($BaTiO_3$) nanoparticles, has been not performed yet. Ceramic $BaTiO_3$ nanoparticles were selected as filler because their presence in the matrix can modify the mechanical properties of the composite [66, 67]. In addition, although no specific data are available in the literature, they were expected to affect also the acoustic properties of the matrix, similarly to other ceramic materials [47, 56]. Finally, it is known that $BaTiO_3$ exhibits piezoelectric properties [68]. Therefore, when stimulated by US waves (mechanical inputs), they are able to generate local electrical charges that demonstrated to provide beneficial stimuli, thus enhancing cell adhesion, proliferation or differentiation [38]. A precise measurement of such properties enables the development of tissue-mimicking phantoms and a highly controlled US exposure of living cells, thus overcoming the uncertainties connected with US wave attenuation and reflection, due to the scaffold on which cells are seeded.

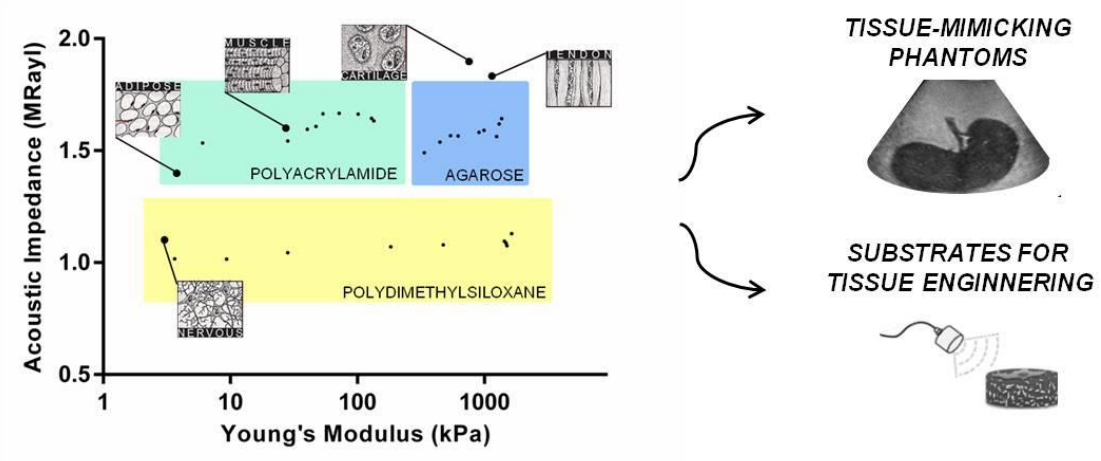

Figure 3.1. *Schematic representation of acoustic/mechanical properties of different tissue mimicking materials analyzed in this study. These results can be used to build tissue-mimicking phantoms, useful for many US-based medical procedures, and to fabricate smart materials for stimulating cells with a highly controlled US dose.*

3.2 Material characterization

Material preparation

Agarose (AG) samples were prepared by dissolving agarose powder (Sigma-Aldrich) in deionized and degassed water (dd-H2O) at 6 different concentrations (2, 3, 4, 5.5, 6.5, 7.5 % w/v). Solutions were kept at 90° C for 1 h under continuous stirring and then cooled down at room temperature to allow material reticulation.

Polyacrylamide (PAA) gels were produced at 6 different concentrations by varying the percentages of acrylamide (A) and Bis-acrylamide (B-A) (Sigma-Aldrich) in dd-H2O as follows: PAA5% (5%A, 0.1%B-A w/v), PAA7% (7%A, 0.2%B-A w/v), PAA9% (9%A, 0.3%B-A w/v), PAA11% (11%A, 0.4%B-A w/v), PAA13% (13%A, 0.5%B-A w/v) and PAA15% (15%A, 0.6%B-A w/v). All samples were supplemented with 1/200 v/v of 10% ammonium persulfate (Sigma-Aldrich) and 0.15% v/v of N,N,N',N'-tetramethylethylenediamine (TEMED, Sigma-Aldrich) to promote crosslinking reactions.

PDMS samples (Sylgard 184, Dow Corning) were prepared in 6 different monomer/curing agent ratios (60:1, 50:1, 40:1, 30:1, 20:1, 10:1 w/w); the mixture was degassed under vacuum for 30 min, poured into proper molds and then thermally treated at 65°C, overnight.

Three additional formulations for each class of material were produced by doping the stiffest formulation (AG 7,5%, PAA 13% and PDMS 10:1) with barium titanate nanoparticles (BaTiO3, 99.9% barium titanate, 100 nm of nominal size, Nanostructured & Amorphous Materials, Inc). BaTiO3 nanoparticles were added in solution at 3 different concentrations (0.1, 1 and 10% w/v) before the reticulation process completed, to obtain homogeneous nanocomposites.

To overcome the issue of a rather poor nanoparticle dispersibility in aqueous solutions (for PAA and AG gels), they were first mixed with a 0.1% w/v glycol chitosan (Sigma-Aldrich) solution and sonicated overnight (2510, Bransonic sonicator). This treatment guaranteed a polymer wrapping around nanoparticles, which enhanced their dispersibility and long-term stability [69]. Then, the glycol chitosan-wrapped nanoparticles were used to prepare the composite samples. Figure 3.2 summarizes the different sample types prepared and tested in this study.

All material types were obtained through properly designed Teflon molds. Cylindrical specimens of diameter (d) = 30 mm and height (h) = 20 mm were used for acoustic tests.

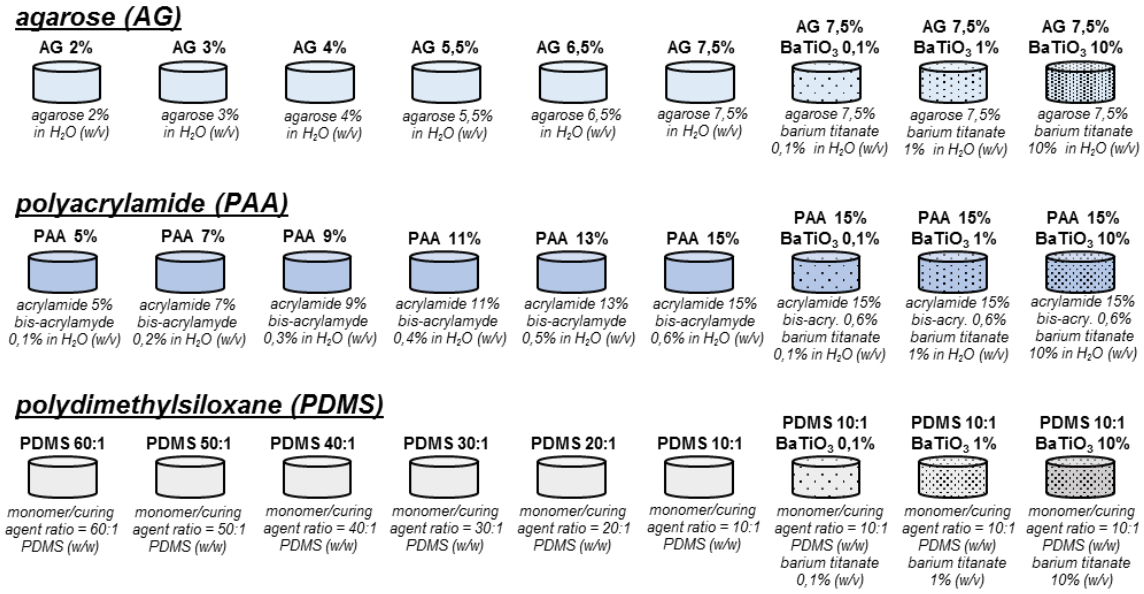

Figure 3.2. *Schematic representation of material formulations used for preparing the different sample types analyzed in this work.*

3.2.1 Acoustic characterization

Material speed of sound (c) and attenuation coefficient (α) were measured by using an insertion technique (also referred as through-transmission technique), in which the unknown acoustic properties of the material under investigation were obtained from comparison with the properties of a reference material (*i.e.* water) [70]. The used experimental set-up is depicted in Figure 3.3-a. The sample was positioned between a US transducer used as transmitter (WS75-2 or WS75-5, Ultran Group) and a needle hydrophone (0.2 mm, Precision Acoustics Ltd) used as receiver. dd-H_2O was used as coupling medium and reference material. Sample and hydrophone were aligned along the main axis of the US transducer in order to maximize the acquired signal.

The US transducer was driven by a wave generator (33220A, Agilent Technologies), connected in series with a 50 dB power amplifier (240L, Electronics & Innovation). A dedicated LabVIEW graphic user interface allowed the remote control of the wave generator and its synchronization with an oscilloscope (7034B, InfiniiVision, Agilent Technologies), from which the hydrophone signal was acquired at a 40 MHz sampling frequency. For all measurements, signals were mediated 10 times in order to significantly reduce noise. At least 3 independent samples for each formulation were tested.

Material c was calculated according to Equation 6.1, where h is the sample thickness, Δt is the delay between the time of flight measured in presence of the sample and the time of flight measured in absence of the sample. c in water (c_w) was calculated as a function of temperature, by using the polynomial interpolation proposed by Marzak [71]. For a simple evaluation of the time of flight, the US transducer (WS75-2) was driven with a pulse signal (250 ns width and 5 ns edge time) and the maximum peak of the acquired signal was considered for time of flight estimation. An example of the acquired signals for c measurements in presence and in absence of the sample is shown in Figure 3.3-b.

$$c = \frac{h}{\Delta t + \frac{h}{c_w}} \qquad \text{Eq. 3.1}$$

Acoustic Impedance (*Z*) was calculated by multiplying *c* by material density (*ρ*), calculated as the ratio between sample mass and volume (Equation 2.9, Section 2.1.1). Volume was assessed with a water-displacement technique [50], using a measurement sensitivity of 100 µL and using a Hirox microscope (Hi-scope KH-2700), mounted orthogonally to the liquid column in which the sample was immersed, to precisely discriminate volume changes.

α was evaluated at 5 different frequencies (1, 2, 3, 4 and 5 MHz) using Equation 6.2, where A_m and A_w are the root mean square of the acquired signal when the US transducer (WS75-2 for frequency f = 1, 2, 3 MHz and WS75-5 for f = 4, 5 MHz) was driven with a sinusoidal tone burst of 40 cycles at frequency f in presence and absence of the sample, respectively, and h is the sample thickness. Representative signals acquired in presence and absence of the sample and used for α estimation are shown in Figure 3.3-c.

$$\alpha = \frac{20}{h} log_{10}\left(\frac{A_m}{A_w}\right) \quad \text{Eq. 3.2}$$

To validate the system, the *c* of castor oil (Eur. Pharm. Grade, Acros Organics), featured by well-established properties and commonly used as acoustic reference material [72], was measured. The castor oil *c* value resulted 1508.8 ± 2.8 m/s at 28.8 °C, while α values were 0.85 ± 0.22, 2.68 ± 0.16, 5.02 ± 0.55, 8.90 ± 0.32 and 12.22 ± 0.79 dB/cm for f=1,2,3,4 and 5 MHz, respectively. These values were in line with those ones reported in previous studies [73, 74], thus confirming the reliability of the described set-up.

The results of *c* and *Z* measurements are reported in Table 3.1 (AG), Table 3.2 (PAA) and Table 3.3 (PDMS) and in Figure A.1 in the Appendix C. The average *c* values were in the range from 1490.0 to 1512.1 m/s for AG, from 1514.2 to 1555.4 m/s for PAA and from 1021.6 to 1054.7 m/s for PDMS.

There was a clear trend of *c* values, which increased in correspondence to more concentrated solutions or more cross-linked formulations for each class of material. By contrast, the presence of nanoparticles in the matrix generally resulted in a decrease of *c* values.

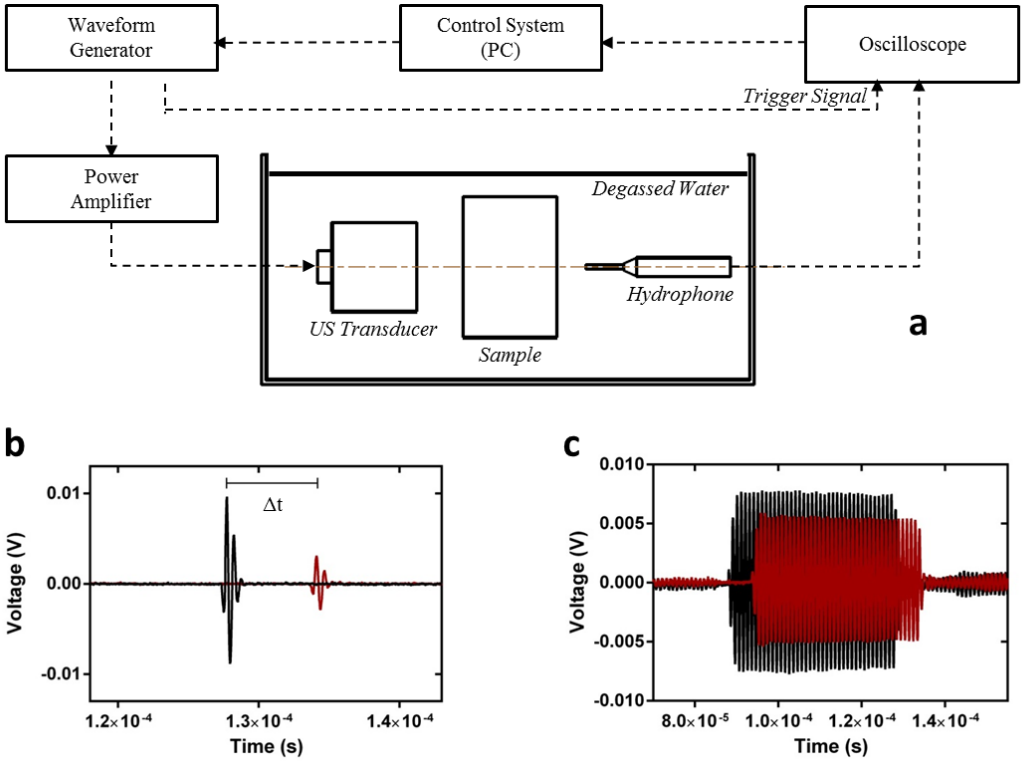

Figure 3.3. *Scheme of the experimental set-up used for speed of sound (c) and attenuation (α) measurements. Examples of signals acquired for c (b) and α (c) evaluation: reference signals (corresponding to water) and sample signals are represented with black and red lines, respectively.*

The average values of Z ranged from 1.490 to 1.643 MRayls for AG, from 1.535 to 1.667 MRayls for PAA and from 1.017 to 1.129 MRayls for PDMS, with greater values in correspondence to more concentrated or more cross-linked formulations, similarly to *c* results. Doped materials generally showed higher Z values in comparison with non-doped counterparts, with the exception of PAA samples.

Such results confirm previous findings [42, 48] and further expand the knowledge on acoustic properties of these material classes, by analyzing a broader formulation range and $BaTiO_3$ nanoparticle-based composites. The presence of $BaTiO_3$ reduced speed of sound. This may appear as counterintuitive, but it is confirmed by other studies reporting reduced *c* values for materials provided with metal or ceramic fillers, in comparison with non-doped controls [47]. A different trend can be observed for *Z* measurements, probably because the decreased speed of sound was compensated by the higher density values of nanocomposites.

Regarding *α* measurement, results are reported in Table 3.4 for AG, Table 3.5 for PAA and Table 3.6 for PDMS, for US frequencies ranging from 1 up to 5 MHz.

The measured α of non-doped AG and PAA materials are in-line with typical values of hydrogels [50, 56], with values smaller than 1 dB/cm. PDMS samples showed significantly higher α values in comparison with AG and PAA samples, up to 17.63 dB/cm (PDMS 20:1 @ 5MHz) and 36.48 dB/cm (PDMS 10:1 BaTiO3 10%, @5MHz). Although a trend was rather clear (α values increasing with material concentration), no statistically significant differences are always evident between different concentrations of non doped materials. Statistically significant differences were found almost between doped and non-doped materials, at high nanoparticle concentrations, demonstrating that the adjunction of $BaTiO_3$ statistically increases the attenuation coefficient of AG, PAA and PDMS. Doped materials showed in fact α values up to 10.46 dB/cm for AG (AG 7.5% $BaTiO_3$ 10%, @5MHz), 3.13 dB/cm for PAA (PAA 15% $BaTiO_3$ 10%, @5MHz) and 36.48 dB/cm (PDMS 10:1 $BaTiO_3$ 10%, @5MHz). The variation of acoustic properties due to $BaTiO_3$ nanoparticles had been never analyzed before. Figure A.2, Figure A.3, Figure A.4 in Appendix C show graphical representations of α measurements.

MATERIAL FORMULATION	*c* (m/s)	*Z* (MRayl)
AG 2%	1490.0 ± 2.0	1.490 ± 0.038
AG 3%	1491.9 ± 1.9	1.538 ± 0.037
AG 4%	1497.2 ± 1.2 (*)	1.567 ± 0.013
AG 5.5%	1503.3 ± 0.9 (**)	1.565 ± 0.028
AG 6.5%	1505.9 ± 0.7 (*)	1.582 ± 0.013
AG 7.5%	1512.1 ± 1.3 (**)	1.590 ± 0.024
AG 7.5% BaTiO3 0.1%	1511.8 ± 1.1	1.563 ± 0.026
AG 7.5% BaTiO3 1%	1511.5 ± 3.2	1.619 ± 0.042
AG 7.5% BaTiO3 10%	1507.8 ± 4.1	1.643 ± 0.040

Table 3.1. *Speed of Sound (c) and Acoustic Impedance (Z) (average ± SD) for AG and related nanocomposites. At least 3 independent samples were tested for each sample type. Statistical comparisons refer to values on each column: each sample is compared with the one reported in the row immediately above. *=p<0.05, **=p<0.01.*

MATERIAL FORMULATION	*c* (m/s)	*Z* (MRayl)
PAA 5%	1514.2 ± 3.1	1.535 ± 0.025
PAA 7%	1520.7 ± 2.5 (*)	1.543 ± 0.016
PAA 9%	1528.7 ± 1.2 (**)	1.596 ± 0.020 (*)
PAA 11%	1539.5 ± 2.7 (**)	1.608 ± 0.044
PAA 13%	1548.5 ± 2.9 (*)	1.664 ± 0.035
PAA 15%	1555.4 ± 1.2 (*)	1.667 ± 0.024
PAA 15% BaTiO3 0.1%	1553.8 ± 2.3	1.663 ± 0.030
PAA 15% BaTiO3 1%	1552.8 ± 2.2	1.644 ± 0.027
PAA 15% BaTiO3 10%	1541.5 ± 1.5 (**)	1.633 ± 0.012

Table 3.2. *Speed of Sound (c) and Acoustic Impedance (Z) (average ± SD) for PAA and related nanocomposites. At least 3 independent samples were tested for each sample type. Statistical comparisons refer to values on each column: each sample is compared with the one reported in the row immediately above. *=p<0.05, **=p<0.01.*

MATERIAL FORMULATION	*c* (m/s)	*Z* (MRayl)
PDMS 60:1	1021.6 ± 4.9	1.017 ± 0.005
PDMS 50:1	1023.6 ± 3.6	1.016 ± 0.004
PDMS 40:1	1026.5 ± 3.6	1.045 ± 0.003 (**)
PDMS 30:1	1033.6 ± 4.4	1.071 ± 0.005 (**)
PDMS 20:1	1040.6 ± 5.5	1.079 ± 0.006
PDMS 10:1	1054.7 ± 5.6 (*)	1.095 ± 0.006 (*)
PDMS 10:1 BaTiO3 0.1%	1051.0 ± 9.5	1.087 ± 0.010
PDMS 10:1 BaTiO3 1%	1040.5 ± 4.3	1.076 ± 0.005
PDMS 10:1 BaTiO3 10%	1031.5 ± 4.8	1.129 ± 0.005 (**)

Table 3.3. *Speed of Sound (c) and Acoustic Impedance (Z) (average ± SD) for PDMS and related nanocomposites. At least 3 independent samples were tested for each sample type. Statistical comparisons refer to values on each column: each sample is compared with the one reported in the row immediately above. *=p<0.05, **=p<0.01.*

MATERIAL FORMULATION	α (dB/cm)				
	1 MHz	2MHz	3MHz	4MHz	5MHz
AG 2%	0.18 ± 0.14	0.16 ± 0.12	0.23 ± 0.19	0.27 ± 0.11	0.26 ± 0.14
AG 3%	0.21 ± 0.16	0.22 ± 0.12	0.27 ± 0.11	0.43 ± 0.26	0.33 ± 0.22
AG 4%	0.27 ± 0.23	0.39 ± 0.25	0.35 ± 0.25	0.52 ± 0.30	0.32 ± 0.22
AG 5.5%	0.33 ± 0.22	0.40 ± 0.31	0.39 ± 0.18	0.62 ± 0.14	0.88 ± 0.30 (*)
AG 6.5%	0.28 ± 0.16	0.27 ± 0.20	0.33 ± 0.23	0.54 ± 0.20	0.78 ± 0.21
AG 7.5%	0.39 ± 0.19	0.47 ± 0.23	0.41 ± 0.17	0.76 ± 0.23	0.99 ± 0.16
AG 7.5% $BaTiO_3$ 0.1%	0.58 ± 0.32	0.55 ± 0.28	0.44 ± 0.32	0.97 ± 0.50	1.40 ± 0.35
AG 7.5% $BaTiO_3$ 1%	0.96 ± 0.61	1.48 ± 0.72 (*)	1.11 ± 0.62	1.75 ± 0.55 (*)	2.42 ± 0.93
AG 7.5% $BaTiO_3$ 10%	6.97 ± 1.03 (**)	6.76 ± 1.86 (**)	8.28 ± 2.15 (**)	9.38 ± 1.47 (**)	10.46 ± 1.22 (**)

Table 3.4. *Attenuation Coefficient α (average ± SD) for AG and related nanocomposites. At least 3 independent samples were tested for each sample type. Statistical comparisons refer to values on each column: each sample is compared with the one reported in the row immediately above. *=p<0.05, **=p<0.01.*

MATERIAL FORMULATION	α (dB/cm)				
	1 MHz	2MHz	3MHz	4MHz	5MHz
PAA 5%	0.17 ± 0.15	0.32 ± 0.26	0.26 ± 0.17	0.36 ± 0.30	0.39 ± 0.26
PAA 7%	0.17 ± 0.12	0.26 ± 0.21	0.23 ± 0.17	0.25 ± 0.16	0.47 ± 0.35
PAA 9%	0.13 ± 0.08	0.19 ± 0.13	0.24 ± 0.18	0.35 ± 0.24	0.53 ± 0.41
PAA 11%	0.19 ± 0.10	0.28 ± 0.19	0.18 ± 0.11	0.26 ± 0.22	0.65 ± 0.47
PAA 13%	0.21 ± 0.12	0.23 ± 0.17	0.30 ± 0.16	0.43 ±0.30	0.42 ± 0.22
PAA 15%	0.25 ± 0.17	0.25 ± 0.20	0.24 ± 0.16	0.36 ± 0.22	0.61 ± 0.36
PAA 15% $BaTiO_3$ 0.1%	0.47 ± 0.17	0.49 ± 0.20	0.55 ± 0.41	0.97 ±0.55 (*)	1.65 ± 0.58 (*)
PAA 15% $BaTiO_3$ 1%	0.64 ± 0.26	0.53 ± 0.24	0.91 ± 0.51	1.15 ± 0.55	2.16 ± 0.57
PAA 15% $BaTiO_3$ 10%	0.70 ± 0.30	0.85 ± 0.40	1.81 ± 0.61	1.78 ± 0.59	3.13 ± 0.62

Table 3.5. *Attenuation Coefficient α (average ± SD) for PAA and related nanocomposites. At least 3 independent samples were tested for each sample type. Statistical comparisons refer to values on each column: each sample is compared with the one reported in the row immediately above. *=p<0.05.*

MATERIAL FORMULATION	α (dB/cm)				
	1 MHz	2MHz	3MHz	4MHz	5MHz
PDMS 60:1	1.95 ± 0.31	3.88 ± 0.35	7.48 ± 0.84	11.12 ± 0.27	15.78 ± 0.39
PDMS 50:1	1.71 ± 0.39	4.56 ± 0.42	8.05 ± 0.56	11.52 ± 0.78	15.92 ± 1.12
PDMS 40:1	2.10 ± 0.42	4.94 ± 0.21	8.54 ± 0.54	12.49 ± 0.31	16.60 ± 0.51
PDMS 30:1	2.00 ± 0.36	4.78 ± 0.67	8.75 ± 0.73	12.60 ± 1.18	17.29 ± 1.04
PDMS 20:1	2.23 ± 0.21	5.55 ± 0.75	9.37 ± 0.53	13.57 ± 1.07	17.63 ± 0.89
PDMS10:1	2.35 ± 0.28	5.72 ± 0.48	9.53 ± 0.95	13.74 ± 1.02	16.58 ± 1.95
PDMS10:1 $BaTiO_3$ 0.1%	2.72 ± 0.55	6.19 ± 0.63	10.36 ± 0.59	14.20 ± 1.25	17.74 ± 1.53
PDMS 10:1 $BaTiO_3$ 1%	3.21 ± 0.22	7.52 ± 0.38 (*)	12.50 ± 0.35	17.34 ± 0.51 (*)	21.01 ± 1.40 (*)
PDMS10:1 $BaTiO_3$ 10%	6.73 ± 0.15 (**)	17.03 ± 0.31 (*)	22.99 ± 0.46 (**)	28.30 ± 2.00 (**)	36.48 ± 1.52 (**)

Table 3.6. *Attenuation Coefficient α (average ± SD) for PDMS and related nanocomposites. At least 3 independent samples were tested for each sample type. Statistical comparisons refer to values on each column: each sample is compared with the one reported in the row immediately above. *=p<0.05, **=p<0.01.*

3.2.2 Mechanical characterization

It is worth mentioning that the different material compositions and doping extents described in this work imply a significant tuning of matrix mechanical properties. This is relevant in the field of tissue-mimicking phantoms, since in some cases (such as US elastography [75] or US guided needle insertion procedures [76, 77]), mechanical properties play a key role. Mechanical properties are also of paramount importance in the field of tissue engineering and regenerative medicine. It is well-known, in fact, that matrix local stiffness strongly influences cell adhesion, proliferation and differentiation [78-80]: integrins, cadherins, and other adhesion molecules that form cell focal adhesions allow to transmit forces to substrates. However, a normal cell not only applies forces but also responds through cytoskeleton organization (and other cellular processes) to the resistance that the cell senses, with deep implications on the main cell functions.

Compression and traction Young's moduli were obtained by performing compression and traction tests respectively, by means of an INSTRON 4464 Mechanical Testing System (± 10 N load cell) on at least 7 independent samples for each material formulation. Cylindrical specimens of d = 15 mm and h = 5 mm were used for compression tests and rectangular specimens of 40 x 6 x 3 mm^3 were used for traction experiments. The imposed velocity was set at 5 mm/min, data were recorded at a frequency of 100 Hz, stress was obtained dividing the load by the cross-sectional area of the specimen and strain was calculated as the ratio between the deformation (extension or contraction) and the initial length of the specimen.

The compression and the traction Young's moduli were then calculated from the stress/strain curves (Figure 3.4) by means of a dedicated MatLab program; a linear fitting of the curve was performed in the initial linear region of the curve and the Young's modulus was consequently obtained as the linear angular coefficient [81].

The results of material characterization are reported in Table 3.7 (AG), Table 3.8 (PAA) and Table 3.9 (PDMS) and in Figure A.5 of Appendix C.

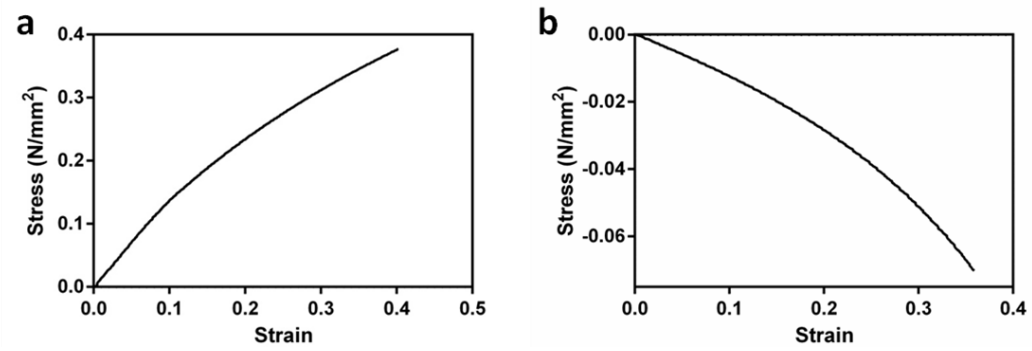

***Figure 3.4**. Examples of the acquired signals used for the estimation of traction (a) and compression (b) Young's moduli.*

MATERIAL FORMULATION	Et(kPa)	Ec(kPa)
AG 2%	335.4 ± 33.2	261.2 ± 30.7
AG 3%	445.0 ± 50.4 (**)	312.7 ± 41.5 (*)
AG 4%	538.7 ± 63.7 (**)	419.7 ± 67.4 (**)
AG 5.5%	618.0 ± 49.8 (*)	463.1 ± 52.0
AG 6.5%	902.1 ± 64.1 (**)	496.9 ± 63.4
AG 7.5%	990.8 ± 127.3	574.4 ± 34.8 (**)
AG 7.5% BaTiO3 0.1%	1240.1 ± 144.5 (**)	664.0 ± 36.4 (**)
AG 7.5% BaTiO3 1%	1299.0 ±113.8	655.0 ± 52.4
AG 7.5% BaTiO3 10%	1362.8 ± 122.5	692.4 ± 55.0

***Table 3.7.** Young's moduli (average ± SD), derived from traction and compression tests performed on AG and related nanocomposites. At least 7 independent samples were tested for each sample type. Statistical comparisons refer to values on each column: each sample is compared with the one reported in the row immediately above. *=p<0.05, **=p<0.01.*

MATERIAL FORMULATION	Et(kPa)	Ec(kPa)
PAA 5%	6.5 ± 0.7	47.4 ± 6.4
PAA 7%	28.2 ± 5.8 (**)	57.2 ± 5.1 (**)
PAA 9%	40.3 ± 3.2 (*)	77.0 ± 8.4 (**)
PAA 11%	47.1 ± 4.9 (*)	106.0 ± 5.6 (**)
PAA 13%	53.5 ± 3.7 (*)	110.0 ± 7.0
PAA 15%	71.7 ± 5.5 (**)	126.1 ± 6.8 (**)
PAA 15% BaTiO3 0.1%	101.0 ± 16.9 (**)	140.3 ± 8.8 (**)
PAA 15% BaTiO3 1%	128.7 ± 16.3 (**)	154.2 ± 8.5 (**)
PAA 15% BaTiO3 10%	134.2 ± 16.3	178.2 ± 7.2 (**)

***Table 3.8.** Young's moduli (average ± SD), derived from traction and compression tests performed on PAA and related nanocomposites. At least 7 independent samples were tested for each sample type. Statistical comparisons refer to values on each column: each sample is compared with the one reported in the row immediately above. *=p<0.05, **=p<0.01.*

MATERIAL FORMULATION	Et(kPa)	Ec(kPa)
PDMS 60:1	3.7 ± 0.8	42.1 ± 4.9
PDMS 50:1	9.3 ± 0.7 (**)	58.2 ± 9.8 (**)
PDMS 40:1	28.2 ± 4.0 (**)	112.1 ± 19.1 (**)
PDMS 30:1	183.0 ± 12.9 (**)	327.9 ± 23.7 (**)
PDMS 20:1	473.2 ± 75.3 (**)	634.9 ± 71.9 (**)
PDMS 10:1	1433.3 ± 126.2 (**)	790.8 ± 38.3 (**)
PDMS 10:1 BaTiO3 0.1%	1478.3 ± 141.3	819.6 ± 68.7
PDMS 10:1 BaTiO3 1%	1500.5 ± 119.8	828.0 ± 81.4
PDMS 10:1 BaTiO3 10%	1631.0 ± 175.0	864.7 ± 61.8

Table 3.9. *Young's moduli (average ± SD), derived from traction and compression tests performed on PDMS and related nanocomposites. At least 7 independent samples were tested for each sample type. Statistical comparisons refer to values on each column: each sample is compared with the one reported in the row immediately above. **=p<0.01.*

3.3 Development of ultrasound phantoms

In order to demonstrate the possible application of the tested materials as tissue-mimicking phantoms for US tests, a simplified cirrhotic liver phantom [82-84] was fabricated.

Typical echoes of US imaging are mainly caused by differences in the acoustic impedance of materials (Z_i) at their interfaces. Thus, in order to reproduce an echographic representation of the interface similar to that one of a real cirrhotic liver in presence of ascites, materials showing a reflection coefficient (γ_r, Eq. 2.10, Section 2.1.1) matching the one of the real tissues were selected.

The phantom was built by using two different AG formulations. The liver was made of AG 7.5% $BaTiO_3$ 10% and fabricated by reflecting the main anatomical features of the native tissues. To this aim, a dedicated mold developed through a 3D printer (3DSystem Projet HD 3000) was used. The upper layer of the phantom, mimicking the properties of the surrounding ascites, was made of AG 2% and obtained by dropping the agar solution on top of a AG 7.5% $BaTiO_3$ 10% substrate, previously casted in the mold. US images were acquired by using an Esaote CA430E conventional 2D imaging convex US probe (Esaote) with a curvature radius of 40 mm and a working frequency of 3.5–5 MHz, positioned perpendicular to the liver/ascites interface.

The phantom, fabricated with AG 2% and AG 7.5% BaTiO3 10% (Figure 3.5-a) showed a γ_r value (calculated by means of Eq. 2.10) of 0.0024, which was close to the one that

can be found at the liver/ascites interface (γ_r = 0.0013) [41, 82]. Therefore, the echo generated in correspondence to the boundary was expected to be similar to the in vivo one. Figure 3.5-b and Figure 3.5-c show echographic images obtained with natural tissues and with the phantom, respectively.

The two images appear very similar, thus qualitatively demonstrating that the tested materials can be used to effectively reproduce the echoes generated at certain tissues' boundaries and, more in general, the acoustic behavior of different anatomical structures.

As shown in Table 2.2 of Section 2.1.3, human tissues possess specific mechanical and acoustic features, showing in some cases minimal differences among them [41, 48, 64, 82, 83, 85, 86]. Materials used for the development of US phantoms should as much as possible faithfully replicate natural tissue acoustic properties. In addition, mechanical properties must be also reproduced in applications such as US elastography, needle insertion and other US-guided procedures.

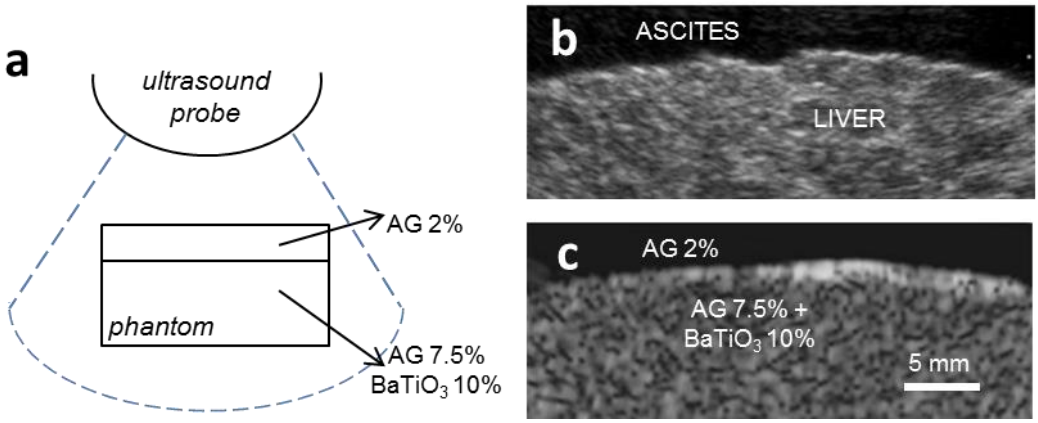

Figure 3.5. *a) Representation of the AG-based phantom and the US imaging acquisition system. US scanner images of a real cirrhotic liver [42] (b) and US images of the liver phantom made of AG 2% and AG 7.5% BaTiO3 10% (c).*

Although in recent years some US phantoms have been developed [41, 42], the majority of tissue substitutes have been modeled by means of homogeneous materials, which do not realistically mimic the *in vivo* scenario. The systematic analysis made in this work, concerning characterization of AG, PAA and PDMS samples at different concentrations and cross-linking extents and corresponding nanocomposites,

represents an added value in this field, since it allows to properly reproduce the features of a rather wide range of soft tissues.

3.4 Controlled in vitro ultrasound cell exposure

It is widely known that stiffness plays an important role in promoting/inhibiting cell processes [78] and substrates used for cell cultures in the field of tissue engineering are normally developed by properly taking into account such factor. However, when biomaterials are used in combination with US waves, acoustic properties must be also precisely known in order to stimulate cells with a highly controlled US dose. In fact, the interfaces between the US transducer and the cells can determine reflections or attenuations which must be estimated, to provide cells with a known US dose. This aspect is largely neglected in tissue engineering and related fields, but it is crucial to obtain reliable results, when US stimulation is involved [87].

Figure 3.6 shows the results obtained 24 h after stimulation of normal human dermal fibroblasts (nHDFs) in a highly controlled and reliable way, through the dedicated US set-up accurately described in Chapter 3. Cells were stimulated at 1 MHz for 3 min, at different US intensities (200 mW/cm^2, 800 mW/cm^2 and 1600 mW/cm^2). One sample type was stimulated at the maximum intensity (1600 mW/cm^2) but a 12 mm specimen made of PDMS 10:1 was interposed between the transducer and the cells. Due to the acoustic properties of the specimen (α = 2.35 db/cm @ 1MHz, Table 3.6), the predicted US signal should be attenuated at half of its intensity, thus resulting in a net US stimulation to cells equivalent to 800 mW/cm^2.

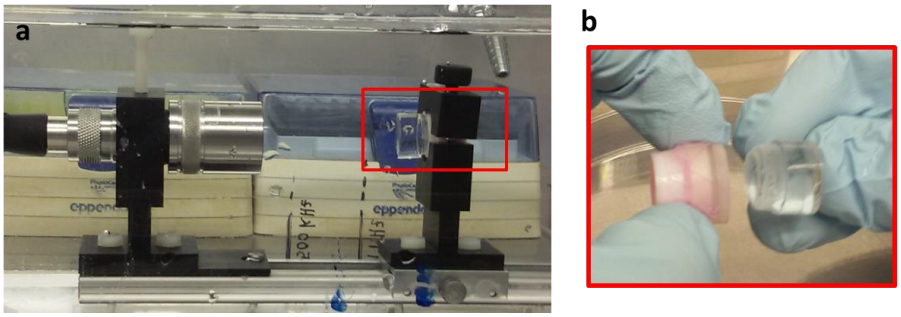

Figure 3.6. *a) Picture of the experimental set-up used for controlled nHDFs US stimulation. As shown in b) one sample type was stimulated with a 12mm specimen of PDMS 10:1 (attenuation of the 50%) interposed between the US source and the target.*

Fluorescence images (Figure 3.7-a) showed a clear positive correlation between US dose and fibroblast proliferation, while no evident differences were found between samples stimulated at 800 mW/cm^2 and the ones provided with the 12 mm - PDMS 10:1 specimen. This was confirmed by quantitative data on DNA content, shown in Figure 3.7-b.

As reported by ter Haar [88], pulsed US may produce transient cavitation effect as well as a change in volume and pressure caused by bubbles formed in the liquid medium, which when hitting one another release energy that may break chemical bonds, thereby producing reactive free radicals and provoking chemical changes in the cells. A pressure change due to this stimulation regime may modify the permeability of the cellular membrane to calcium and sodium ions, thus increasing protein synthesis. Furthermore, organelles may be altered due to irradiation forces. These alterations are thought to be responsible for the enhanced cell proliferation observed.

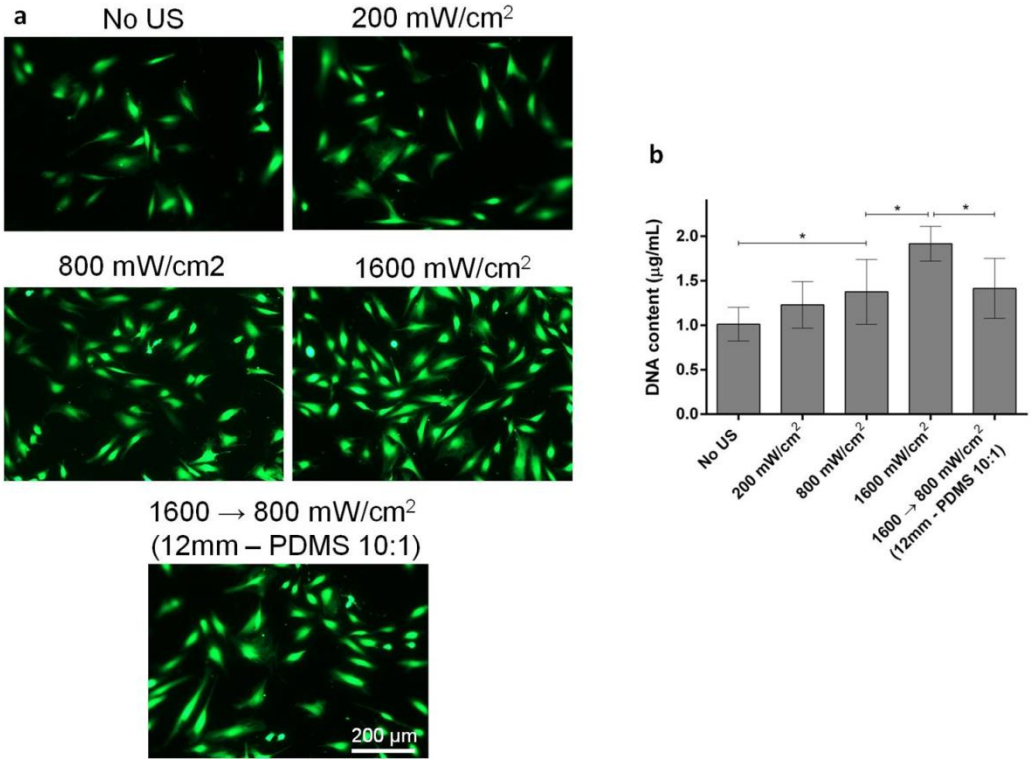

Figure 3.7. *a) Fluorescence images of nHDFs stimulated at different US intensities. Images were acquired 24 h after US stimulation. b) DNA content for the different sample types 24 h after US stimulation. *=p<0.05.*

The bioeffect triggered by US stimulation (enhanced proliferation, correlated with US intensity) matches with the evidences reported by de Oliveira and colleagues [89]. In

comparison with this study it was achieved more marked proliferation differences at 24 h, due to a wider stimulation intensity range. In addition, the mentioned study focused on I929 (murine) fibroblasts, while herein was analyzed the response of human dermal fibroblasts. Furthermore, it was demonstrated that the knowledge on the acoustic properties of the material interposed between the transducer and the cells allowed to correctly predict the actual intensity delivered, and thus the triggered bioeffect. In fact, the DNA content of the 800 mW/cm2 sample and the one of the 1600 → 800 mW/cm2 (12 mm – PDMS 10:1) were statistically equal and their average values were really close (1.375 and 1.414 μg/mL, respectively).

3.4.1 Ultrasound fibroblasts stimulation mediated by piezoelectric nanoparticles

Another experiment aimed at assessing the potential of $BaTiO_3$-based nanocomposites as smart responsive substrates for cell culture was performed. $BaTiO_3$ nanoparticles show piezoelectric properties that can convey the mechanical stimuli provided by US waves in electrical ones, thus targeting a series of possible intriguing bioeffects [90].

In fact, piezoelectric nanomaterials offer the exceptionally opportunity of delivering electrical stimulation within biological environments in a wireless mode by simple exposure to mechanical stimulation sources (*e.g.* US) [91]. The possibility of generating in situ small voltages in response to US stimulation (direct piezoelectric effect) represents an extremely attractive phenomenon in regenerative medicine, especially for electrically responsive tissues, such as nervous tissue [45], muscles [46] and bones [92].

A simple electro elastic model simulates this interaction [93] providing the maximum electric potential increment (φ_r) generated by US on the surface of a piezoelectric element in stress-free condition.

$$\varphi_r = -\frac{R(se_{rr}+2e_{r\theta})}{s\varepsilon_{rr}}\left(\frac{P_{US}}{s\gamma+2\alpha}\right) \qquad \text{Eq. 3.3}$$

where R is the radius of the piezoelectric element, e_{rr} and $e_{r\vartheta}$ the piezoelectric coefficients, and ε_{rr} the dielectric constant of the piezoelectric nanofiller. In addition,

α, γ and s are parameters depending on the Young modulus and Poisson ratio of the piezoelectric element, and P_{US} is the maximum pressure associated with the US wave.

With the aim to assess if the presence of piezoelectric nanoparticles could result in a different bioeffect on nHDFs, the sample type stimulated at 800 mW/cm^2 was compared with another one stimulated at 1600 mW/cm^2 but provided with a 4 mm specimen made of PDMS 10:1 BaTiO3 10% (α = 6.73 db/cm @ 1MHz, Table 3.6) interposed between the transducer and the cells. Due to the acoustic properties of the specimen, the US signal should be attenuated at half of its intensity, thus resulting in a net US stimulation to cells equivalent to 800 mW/cm^2. In addition, the piezoelectric nanoparticles entrapped in the top part of the specimen were in direct contact with the bottom side of the 20 µm polystyrene membrane (the opposite side respect to the one covered by cells).

Results are shown in Figure 3.8: interestingly, the proliferation effect was clearly enhanced in the presence of the interposed material, although the net US doses provided to the cells were the same. This was probably due to the piezoelectric effect and the electric field generation mediated by $BaTiO_3$ nanoparticles, which had a significant effect despite the nanocomposite was not in direct contact with the cells.

Few scientific evidences have been recently reported on this topic. A proliferation increase of H9c2 cardiac-like cells was observed by the authors on nanocomposites of poly(lactic-co-glycolic) acid and $BaTiO_3$ nanoparticles [94]. However, no US stimulation was performed in this study. More recently, Marino and colleagues reported enhanced osteoblast (Saos-2 cells) differentiation on a resin-based BaTiO3 nanoparticles-doped scaffold, due to US stimulation [92]. Genchi and colleagues demonstrated enhanced neuron (SH-SY5Y cells) differentiation on poly(vinylidene fluoride-trifluoroethylene) films doped with the same nanoparticle type and stimulated with US waves [95]. In all these studies, US stimulation was performed in a poorly controlled way and the actual dose reaching the cells was not accurately measured, making the triggered bioeffects poorly repeatable. The same consideration applies for different yet connected evidences, related to intracellular stimulation mediated by piezoelectric nanoparticles [45] [96]. This study quantifies for the first time the bioeffect triggered by piezoelectric

nanoparticles stimulated by US waves, by relating such bioeffect to a precise US dose delivered. From a biological viewpoint, the main mechanisms responsible for such biological responses are still rather unclear. In our case, the generation of electrical charges during US stimulation, due to the piezoelectric features of the composite substrate, probably influences voltage-gated channels on cell membranes, thus modifying the permeability of the cellular membrane to calcium and sodium ions, which alter protein synthesis and lately cell proliferation. The generated electrical charges may be also responsible for an enhanced adsorption of proteins (*e.g.* available in the culture medium) on the substrate, another event which may have a role in the marked enhancement of cell proliferation.

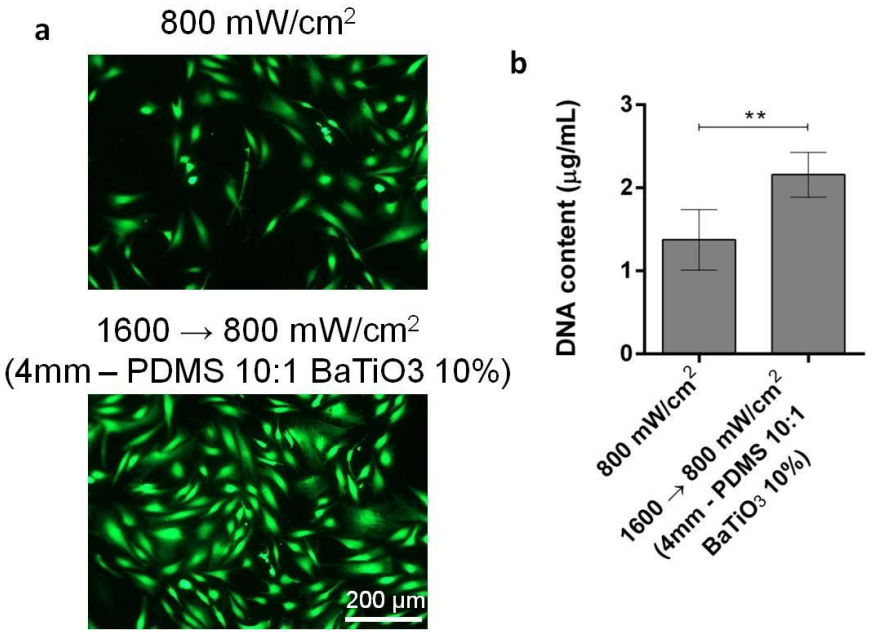

Figure 3.8. *a) Fluorescence images of nHDFs stimulated with an US dose of 800 mW/cm^2 (top image) and with a net dose of 800 mW/cm^2, due to the attenuation of a 4 mm specimen made of PDMS 10:1 BaTiO3 10% (bottom image). Images were taken 24 h after US stimulation; b) DNA content 24 h after US stimulation for the two sample types. **=p<0.01.*

Scientific production (Chapter 3)

Publications on Internationals journals

- **A. Cafarelli**, L.Ricotti, A. Verbeni, A: Poliziani, P. Dario, A. Menciassi. "Tuning mechanical and acoustic properties of materials for ultrasound phantoms and smart substrates for cell cultures". *Acta Biomaterialia, 2017*;

- **A. Cafarelli**, P. Miloro, A. Verbeni, M. Carbone, and A. Menciassi. "Speed of sound in rubber-based materials for ultrasonic phantoms". *Journal of Ultrasound, 2016;*

Papers presented at International conferences

- **A. Cafarelli**, A. Diodato, M. Mura, S. Tognarelli, L. Ricotti, G. Ciuti, A. Menciassi, "A tissue-mimicking phantom for in-vitro accuracy evaluation of USgHIFU procedures". 3rd European Symposium on Focused Ultrasound Therapy. London, October, 2015; Awarded as best oral presentation.

4 *In vitro* Low Intensity Ultrasound cell stimulation

Low Intensity Pulsed Ultrasound (LIPUS) is being widely used as an effective therapeutic tool for tissue healing (e.g. in the physiotherapy domain), but it is also emerging as an innovative strategy in the field of targeted therapies, especially concerning triggered drug delivery systems [36, 97]. However, some aspects dealing with optimal US exposure regimes for cell stimulation and the physical mechanisms involved in the interaction between US waves and biological tissues still have to be clarified [39].

Although *in vivo* experiments are mandatory to evaluate new therapeutic US applications and, more in general, to validate devices prior to clinical trials, *in vitro* experiments play anyhow an important role in the development of therapeutic platforms, especially for understanding basic mechanisms on which therapeutic effects can be grounded. Unfortunately, most of the research groups active in this field exploit US by using non standardized configurations, vulnerable to errors during calibration and use [5]. Consequently, several results that are available in the state of the art are hardly comparable and in many cases they suggest rather different conclusions, thus slowing down the transition to clinical application. As highlighted in Section 2.3, any attempt to determine a quantitative relationship between the exposure doses and the observed effects should be based on reliable measurements of the US field used during the study and on a proper design of the test bench [6].

In this Chapter, after briefly exploring the state of the art of LIPUS with particular attention to *in vitro* studies (Section 4.1), the characterization of the US field of each transducer used in this Chapter is reported (Section 4.2). Characterization was performed both in terms of pressure field maps and intensity, in free field conditions for each frequency of interest. Then, an advanced experimental set-up is described: its purpose was to allow an easy and reliable modulation of US stimulation parameters, such as intensity, therapy duration, duty cycle and frequency. The main purpose of these activities was to minimize the exposure errors that typically affect the vast majority of systems currently used for *in vitro* US cell stimulation (Section 4.3). For example, liquid-air interfaces and reflective obstacles along the wave propagation path

were avoided and a thin polystyrene membrane was used to minimize transmission losses and standing waves formation (thus preventing the typical drawback of plastic multi-well plates). The developed system was exploited to investigate the effects of controlled LIPUS exposures at different frequencies and intensities on C2C12 muscle cells (Section 4.4). The novelty of this study lies in a direct comparison of the effects (*i.e.* cell proliferation and differentiation) produced by different US stimulation conditions on muscle cells, by using a highly reliable set-up, thus minimizing possible exposure inaccuracies and shedding light on the optimal US exposure parameters needed to maximize C2C12 proliferation and differentiation processes.

Finally, an advanced LIPUS stimulation/monitoring platform, that enables a controlled *in vitro* US exposure with a real-time optical monitoring of the target, is also presented in Appendix D.

4.1 *In vitro* LIPUS stimulation: background

When US does not induce lethal effects on cells, it can be defined as low intensity US [39]. This technique is generally identified as Low Intensity Pulsed Ultrasound (LIPUS) stimulation. In fact, in order to reduce the total dose to the target and to minimize thermal effects, the stimulation is commonly pulsed. The typical frequency range of LIPUS is between 40 kHz to 5 MHz with intensity levels between 5 and 1000 mW/cm^2 (SATA, spatial average temporal average intensity), and the commonly burst excitation used is characterized by a pulse width of 200 μs and pulse repetition frequency (PRF) of 1 kHz [98], corresponding to a duty cycle of 20%.

LIPUS is used for promoting healing in different tissues, for a variety of applications, especially in rehabilitation medicine [99, 100], bone-fracture healing [101], soft-tissue regeneration [102], and inflammatory responses inhibition [103]. At a cellular level, LIPUS has been also observed to increase migration and proliferation of aortic endothelial cells, proliferation of fibroblasts, Schwann cells and other cell types [39].

Despite a significant number of evidences that LIPUS can be beneficial to cells and tissues, little attention has been invested in understanding the mechanisms underlying them. Thus, a clear correlation between physical effects and corresponding induced bioeffects is far from being fully understood.

Regarding the associated physical effects, thermal effects (temperature increases are typically below 1°C), as well as cavitational effects, play a minor role since they generally appear at higher intensities. However, other mechanical effects such as radiation force, acoustic streaming and strain gradients seem to play a major role in triggering cellular responses at LIPUS exposures. The US wave can directly affect the cellular mechanosensitive elements by inducing oscillatory strains and creating shear stresses on cell membranes at the driving frequency [98]. Also radiation force can induce a mechanical stimulus at the frequency corresponding to the PRF (typically 1 kHz) [104]. Finally, acoustic streaming or other fluid flow-related phenomena can be induced; they can be associated with a redistribution of elements in the cells environment, thus triggering different biological responses [105].

As previously mentioned, *in vitro* experiments cannot substitute the *in vivo* validation of therapeutic technologies. However, the *in vitro* setting allows to selectively study specific cellular mechanisms (*e.g.* by blocking other competing ones, within a cell), thus reducing the enormous complexity that features *in vivo* phenomena and allowing to verify hypotheses concerning the bioeffects induced by US. In recent years, several research groups focused on the interaction between US waves and cells, trying to analyze the biological outcomes associated with different exposure regimes. However, poorly standardized configurations, lack of proper calibration and lack of control on US wave reflections/attenuations, jeopardize the comparison between *in vitro* and *in vivo* studies, and even between different *in vitro* experiments made with different geometrical set-up configurations, therefore slowing down the translation of such efforts to the clinical reality.

In the state of the art of LIPUS studies, different US exposure set-up configurations can be found [106], *such as*, (a) direct coupling of the transducer to the bottom of the culture well via coupling gel (Figure 4.1-a), (b) immersion of the US transducer in the cell culture medium and (c) culture dish positioned at the water-air interface.

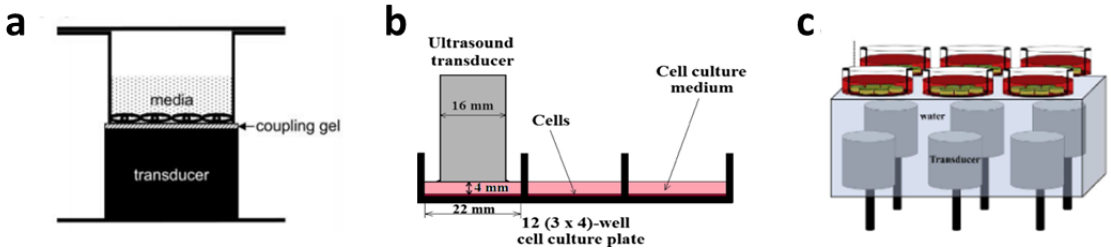

Figure 4.1. *Different set-up configurations typically used in the state of the art of in vitro LIPUS stimulation. a) Sena et al. 2005 [107], b) Katiyar et al. 2014 [108], c) Thakurta et al. 2014 [44].*

All these geometrical configurations significantly affect the propagation of US wave, compromising the attempt to precisely deliver a known US dose to a cell monolayer. In the (a) and (b) configurations shown in Figure 4.1, the transducer is placed very close (3-5 mm) to the cell layer; this distance is much smaller compared to the Rayleigh distance ($z_r=\pi r^2/\lambda$, where r is the transducer radius and λ the wavelength), and therefore the target is exposed to the typical inhomogeneities of the near-field. In configuration (a) the transducer is also directly coupled to the culture well bottom and significant temperature rises can be generated inside the dish (*e.g.* 3°C at 30 mW/cm^2

[5]) due to the US transducer heating. Furthermore, all the geometrical configurations represented in Figure 4.1 are subjected to reflections of the US wave due to the liquid/plastic, liquid/transducer and liquid/air interfaces along the acoustic propagation direction. Due to the mismatch of acoustic impedances, part of the energy is reflected and part is transmitted (Eq. 2.10 and Eq. 2.11), and due to the long pulse duration (at least 200 μs) other hardly predictable effects, such as the formation of standing waves inside the culture dish can occur. As demonstrated by Leskinen and Hynynen in 2012 [5] all of these combined factors can lead to uncertainties of up to the 700% in the US exposure of cells in traditionally employed *in vitro* configurations.

Therefore, as also described by Yddal *et al*. [109], a rational design of the acoustic exposure is crucial in achieving highly reproducible US exposure on cells.

The above considerations, together with the points highlighted in Section 2.3, were taken into account for the design and the development of an experimental set-up for LIPUS *in vitro* stimulation, enabling the opportunity to explore various US stimulation parameters, such as intensity, therapy duration, duty cycle and frequency, and minimizing the typical exposure errors of traditional *in vitro* US cell stimulation systems.

The stimulation platform was validated by studying the influence of LIPUS on skeletal muscle regeneration (by using the C2C12 myoblastic cell line as a model) and by paying particular attention to the frequencies and intensities that could leads towards an optimization of cell proliferation and differentiation. The developed system has the potential to be used also for other cell types and for *in vitro* drug delivery experiments.

A detailed state of the art of the use of LIPUS for skeletal muscle regeneration is reported in Salgarella *et al.* [110].

4.2 Ultrasound transducer characterization

As explained in Section 2.3, US transducer characterization is of primary importance for any rigorous study on therapeutic US.

In this study, three different transducers (Ultran Group) were used for exploring five different stimulation frequencies: WS75-0.5 for 500 kHz, WS75-2 for 1, 2 and 3 MHz and WS75-5 for 5 MHz. Each of the transducers used for the experimental test described in this Chapter (Section 4.4) was characterized in free field conditions both in terms of pressure field map and intensity at all investigated frequencies (Section 4.2.2). In order to maximize the energy transfer from the signal generator system to the piezoelectric US transducer and consequently maximize the acoustic energy generated by the piezoelectric element (reported in Section 4.2.1) required designing of electric impedance matching networks to be interposed between the source and the load in some cases. This is described in the following section.

4.2.1 Impedance matching circuits

Impedance matching is the practice of designing the input impedance of an electrical load to maximize the power transfer and consequently minimize signal reflection from the load [111]. The goal was to match the output impedance of the RF amplifier to a 50 Ω output load, adding passive electronic components between the source and the load. The real and the imaginary part of the transducer's electrical impedance (Z_l) was measured at all frequencies of interest with a vector network analyzer (DG8SAQ, SDR-Kits, Trowbridge, Wilts, UK). Results are reported in Table 4.1.

The source generation system was composed of a wave generator (33220A, Agilent Technologies) connected in series with a 50 dB power amplifier (240L, Electronics & Innovation Ltd). The output impedance of the RF amplifier is 50 Ω and a gain of 50 dB is guaranteed with a minimal variation (±1.5) for voltage standing wave ratio (VSWR) up to 2.5:1 (*i.e.* loads from 19 to 240 Ohm). Therefore for the WS75-2 (f = 1, 2 and 3 MHz) it was not strictly necessary to improve electrical matching between the source and the transducer. However due to a big mismatch between the output impedance of the signal generator system (Z_s = 50 Ω) and the piezoelectric US transducer (Z_l), in

other cases it was necessary to design impedance networks, with the goal to match the output of the RF amplifier to 50 Ω output load.

Transducer	f [MHz]	Re (Z_l) [Ω]	Im (Z_l) [Ω]	$\|Z_l\|$ [Ω]
WS75-0.5	0.50	64	-813	815,5
WS75-2	1	7	-130	130,2
	2	11	-67	67,9
	3	4	-46	46,2
WS75-5	5	3,5	-0,25	3,5

Table 4.1. *Real and imaginary components of transducer's electrical impedance.*

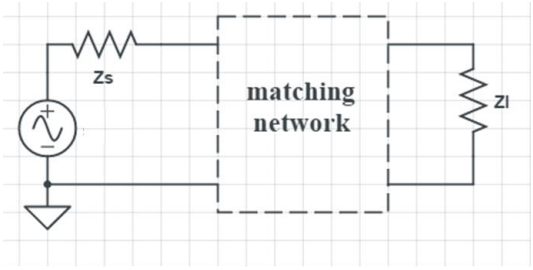

Figure 4.2. *Schematic diagram of a matching network circuit interposed between the source and the load.*

For the WS75-0.5 transducer experiments at 500 kHz, a low pass impedance matching electric circuit with an inductance of 122 µH and a capacitance of 443 pF (Figure 4.3) was designed and interposed between the RF amplifier and the WS75-0.5 transducer (Re(*Z*) = 64 Ω and Im(*Z*) = -813 Ω @500 kHz). This was done in order to maximize the power transferred to the transducer and to minimize the reflected signal.

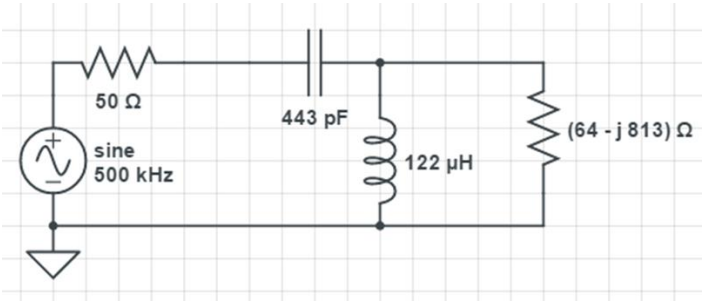

Figure 4.3. *Schematic diagram of the matching network circuit designed for transducer WS75-0.5 @ 500 kHz.*

Due to the very low electrical impedance of the WS75-5 transducer ($|Z_l|$ = 3.5 Ω @ 5 MHz), a linear 15 MHz bandwidth power amplifier, developed at the University of Florence (UNIFI), was used instead of the broadband RF amplifier for maximizing the power transfer to the ultrasonic transducer [112]. The latter amplifier, represented in Figure 4.4, was specifically designed for power ultrasonic applications, having very low output impedance and low distortion.

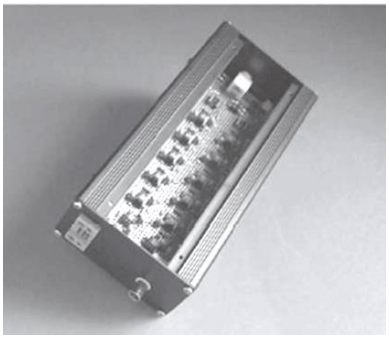

Figure 4.4. *Final assembly of the 15 MHz bandwidth, 60 V_{pp} (peak to peak voltage), low distortion power amplifier developed at UNIFI [112].*

4.2.2 Pressure mapping and Intensity characterization

After the realization of impedance matching networks, all transducers were characterized in free field conditions both in terms of pressure field map and intensity at all investigated frequencies.

Pressure mapping is a fundamental procedure for the definition of the geometrical properties of the acoustic field. The system used for the acoustic characterization of US transducers in terms of pressure field maps, previously developed at the BioRobotics Institute [113], is shown in Figure 4.5.

It consists of the following components:

- A tank built in house with 15 mm thick Plexiglas sheets. It is filled with degassed water and equipped with a rigid frame for holding the transducer under investigation. An acoustic absorber (AptFlex F28) has been fixed on the surface opposite to the transducer to minimize reflections;
- A 3 axis step-by-step motorized positioning frame/gantry (XXYZ BiSlide, Velmex), with a travel range of approximately 500x1000x500 mm^3 and a step length of 6 μm;

- A hydrophone, rigidly mounted to the positioning frame. A 0.2 mm PVDF needle hydrophone (1-30 MHz frequency range, Precision Acoustics Ltd) was used for the calibration of transducers in the MHz range and an ITC-6128 hydrophone (100-600 kHz, International Transducer Corporation) was used for calibration in the kHz range;
- A direct digital synthesis wave generator (33220A, Agilent Technologies) remotely controlled via USB connection, used to generate the electric signal that are sent to the transducer;
- A 50 dB RF power amplifier (240L, Electronics & Innovation Ltd) connected in series with the wave generator. For WS75-5 transducer (@ 5 MHz) the 15 MHz bandwidth power amplifier, developed at UNIFI [112], was used instead of the RF amplifier;
- An oscilloscope (7034B, InfiniiVision, Agilent Technologies) remotely controlled via USB connection;
- A user-friendly Graphical User Interface (GUI) developed in LabView to control the gantry, the wave generator and the oscilloscope in an automatic mode.

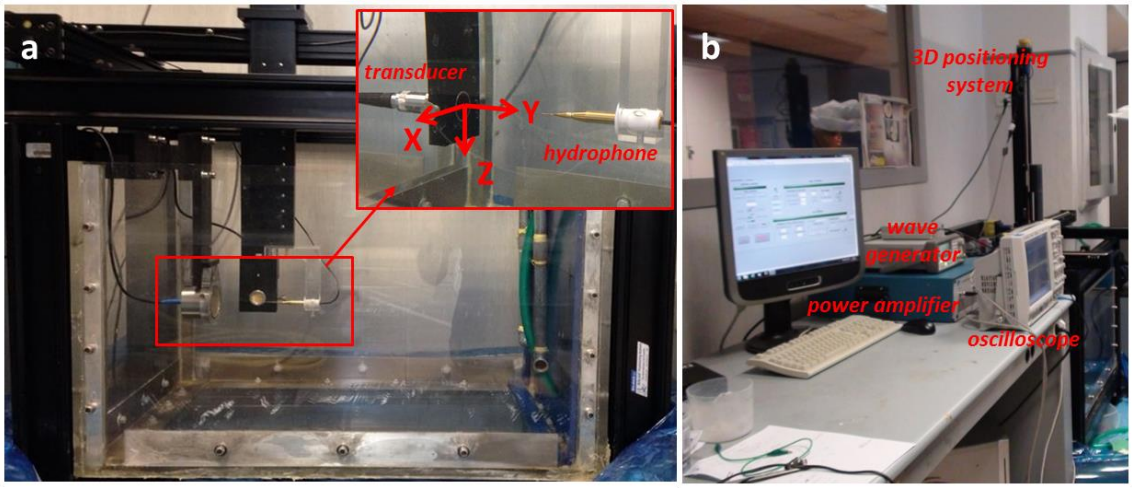

Figure 4.5. *Pressure mapping system used for acoustic characterization of transducers: a) mechanical components for positioning of the generation and measurement devices; b) electronic components for the generation, acquisition and storing of the signal.*

The workflow of the pressure mapping procedure is schematically represented in Figure 4.6.

Basically the hydrophone is positioned at a reasonable position to detect the signal, using manual movements of the motors. Transverse 1D scans are then performed

along the radial directions with respect to the transducer (X and Z, Figure 4.7-a and , Figure 4.7-b), finding the maximum point of pressure in both directions while paying attention to reject side lobes. Once the coordinate of the maximum in the X-Z plane is found, an axial (Y direction, , Figure 4.7-c) scan is performed in order to find the position of the focus and define the regions of near and far field.

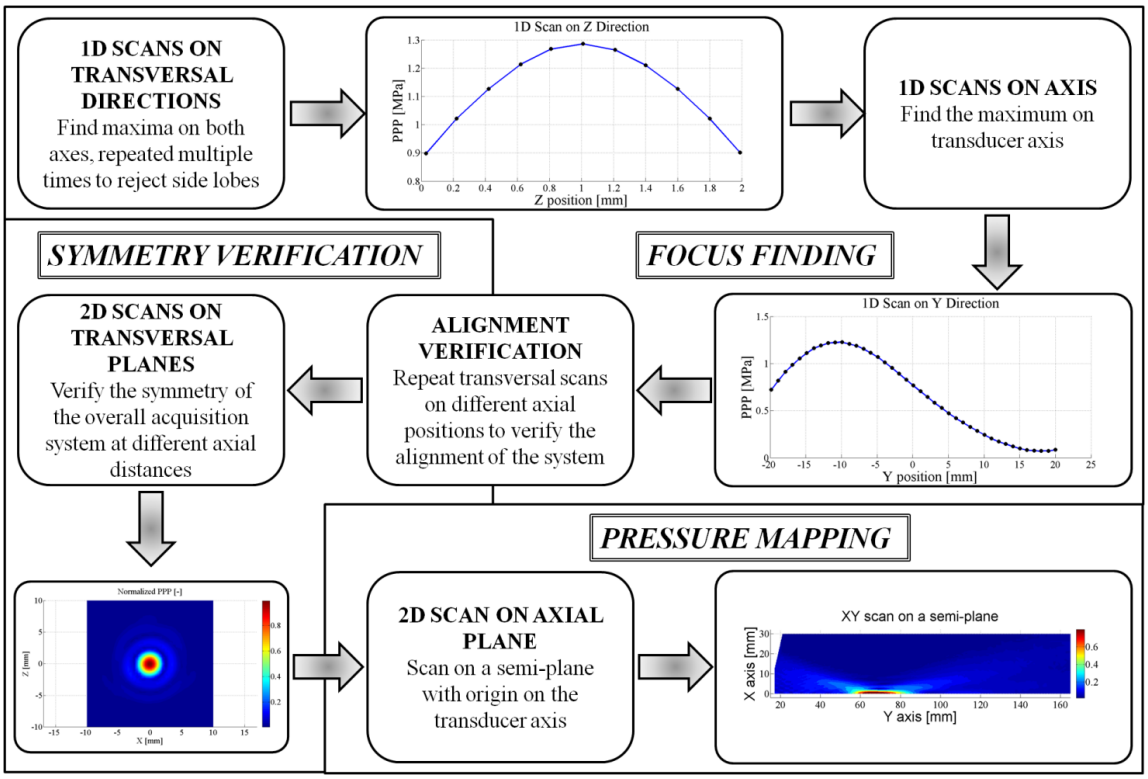

Figure 4.6. *Workflow for the pressure mapping procedure. Figure readapted from P. Miloro's PhD thesis [113].*

Afterwards, the alignment between the transducer and the hydrophone can be verified checking the coordinates of the maximum signal in transversal (X-Z) planes at different axial distances. If the alignment and symmetry of the field is verified, the problem of pressure mapping can be reduced from a 3D to a 2D problem, assuming the axial symmetry of the field. This assumption allows measurements of the field only in a semi-plane with the origin on the transducer axis, considerably reducing the number of points required to complete the procedure.

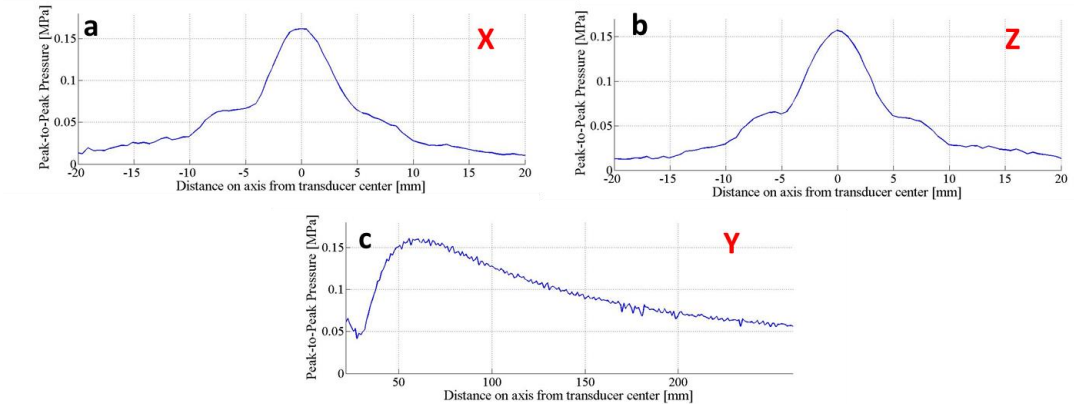

Figure 4.7. *Results of axial scans in the three direction for the transducer WS75-2 (@1 MHz). a) Scan on the radial axis X; b) Scan on the radial axis Z; c) Scan on the axial axis Y.*

All transducers used in this work were characterized both in terms of pressure field maps and in terms of intensity vs driven voltage. After the 2D scan, the hydrophone was positioned at the point of maximum acquired pressure and the Spatial Peak Pulse Average Intensities (I_{SPPA}) were evaluated, while the driven voltage was measured at the output of the power amplifier.

The results of acoustic characterization for each frequency under investigation are reported in Figure 4.8 (*f = 500 kHz*), Figure 4.9 (*f = 1 MHz*), Figure 4.10 (*f = 2 MHz*), Figure 4.11 (*f = 3 MHz*) and Figure 4.12 (*f = 5 MHz*). All axial pressure field maps are also shown in Figure 4.13.

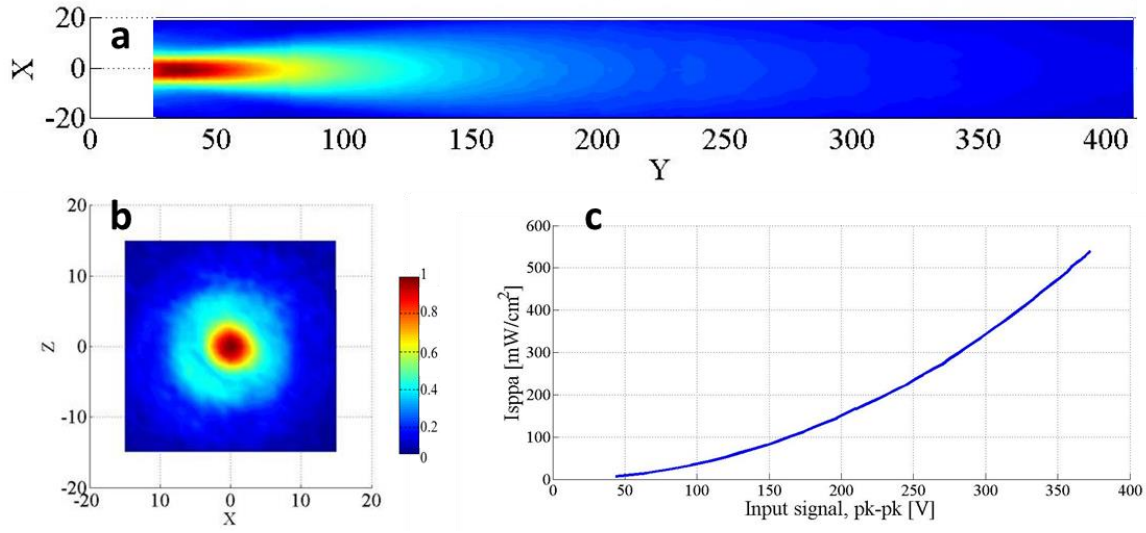

Figure 4.8. *Acoustic characterization of WS75-05 transducer (**@ 500 kHz**): a) normalized peak-to peak pressure map in the axial plane of the transducer (map XY); b) transverse normalized peak-to-peak pressure map at the "focus" distance (map XZ, Y=35 mm); c) pulse average intensity vs driven voltage curve measured at the focus.*

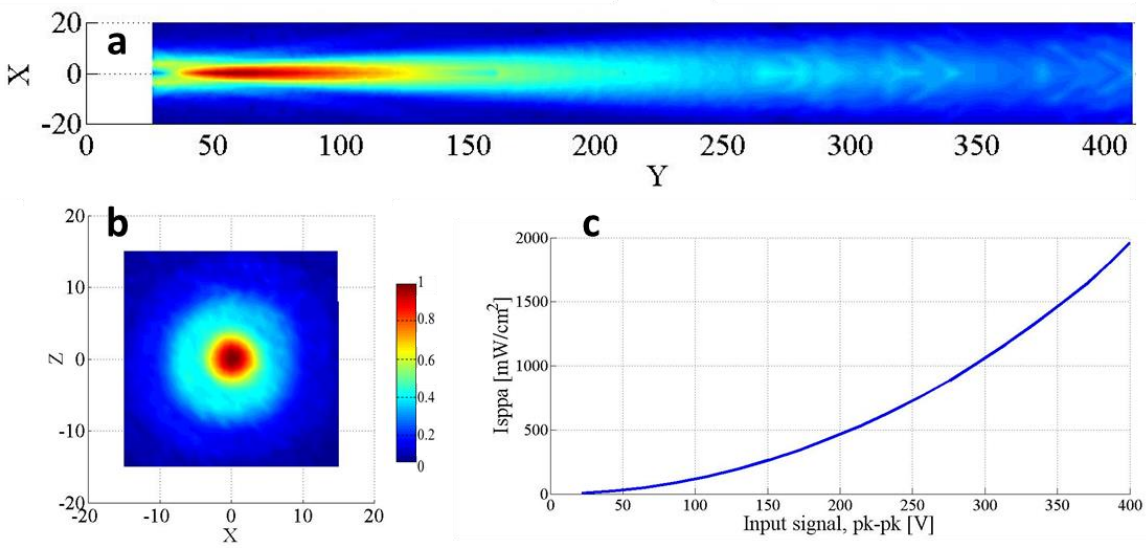

Figure 4.9. *Acoustic characterization of WS75-2 transducer (**@ 1 MHz**): a) normalized peak-to peak pressure map in the axial plane of the transducer (map XY); b) transverse normalized peak-to-peak pressure map at the "focus" distance (map XZ, Y=61.5 mm); c) pulse average intensity vs driven voltage curve measured at the focus.*

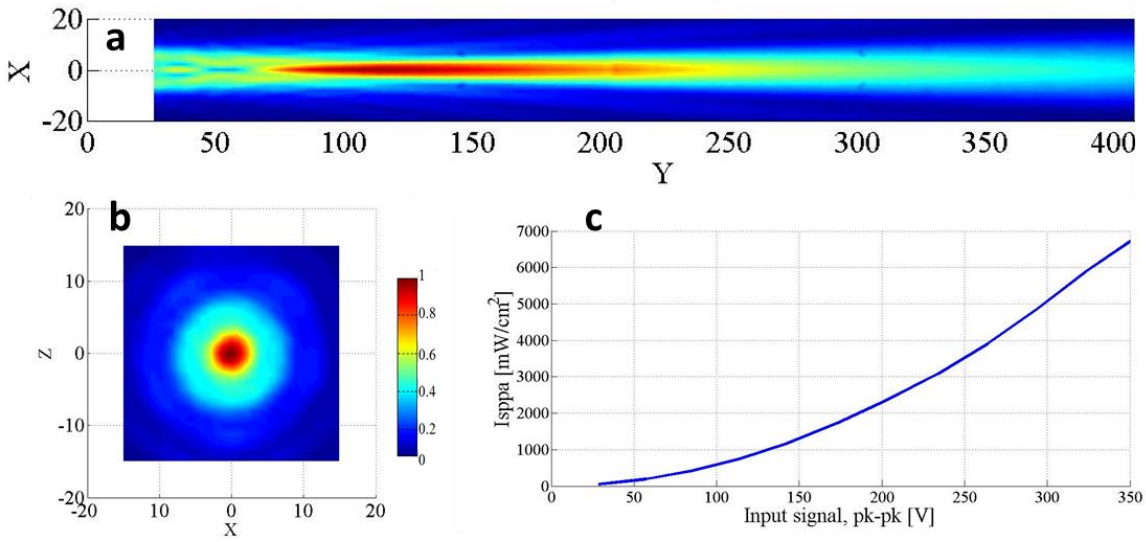

Figure 4.10. *Acoustic characterization of WS75-2 transducer (**@ 2 MHz**): a) normalized peak-to peak pressure map in the axial plane of the transducer (map XY); b) transverse normalized peak-to-peak pressure map at the "focus" distance (map XZ, Y=108 mm); c) pulse average intensity vs driven voltage curve measured at the focus.*

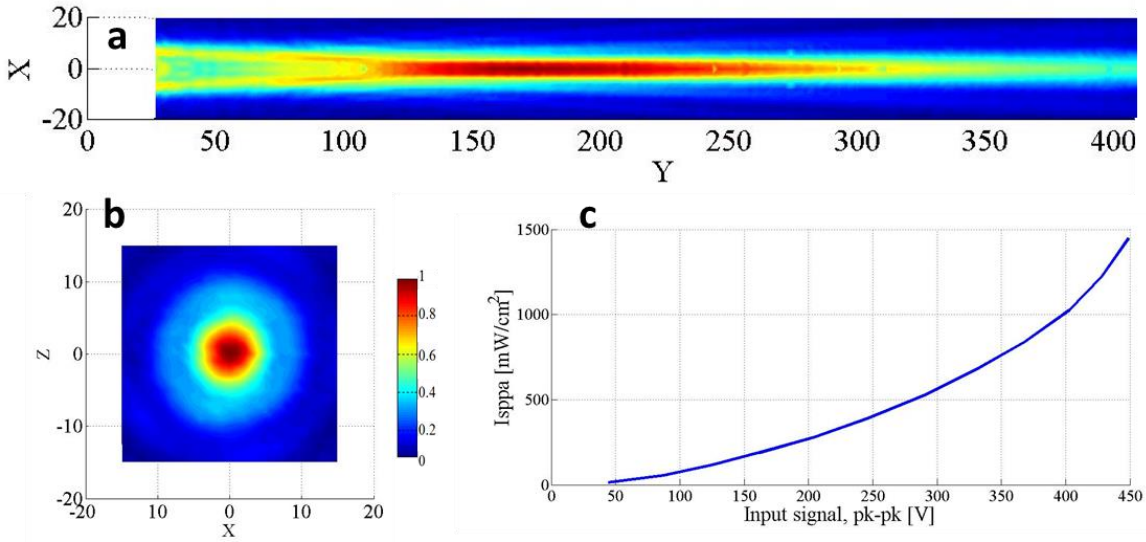

Figure 4.11. *Acoustic characterization of WS75-2 transducer (**@ 3MHz**): a) normalized peak-to peak pressure map in the axial plane of the transducer (map XY); b) transverse normalized peak-to-peak pressure map at the "focus" distance (map XZ, Y=185 mm); c) pulse average intensity vs driven voltage curve measured at the focus.*

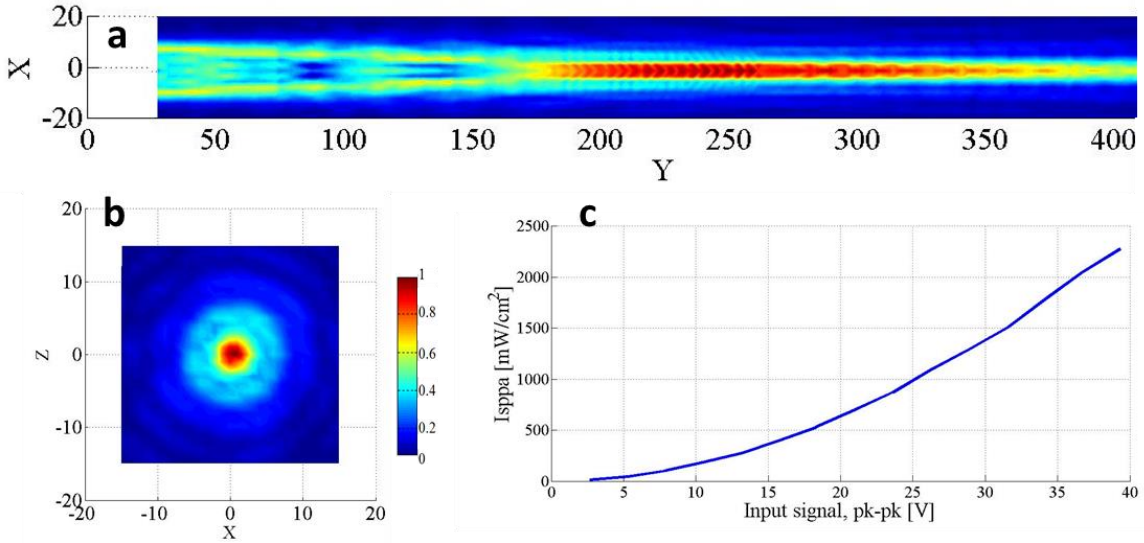

Figure 4.12. *Acoustic characterization of WS75-5 transducer (**@ 5MHz**): a) normalized peak-to peak pressure map in the axial plane of the transducer (map XY); b) transverse normalized peak-to-peak pressure map at the "focus" distance (map XZ, Y=240 mm); c) pulse average intensity vs driven voltage curve measured at the focus.*

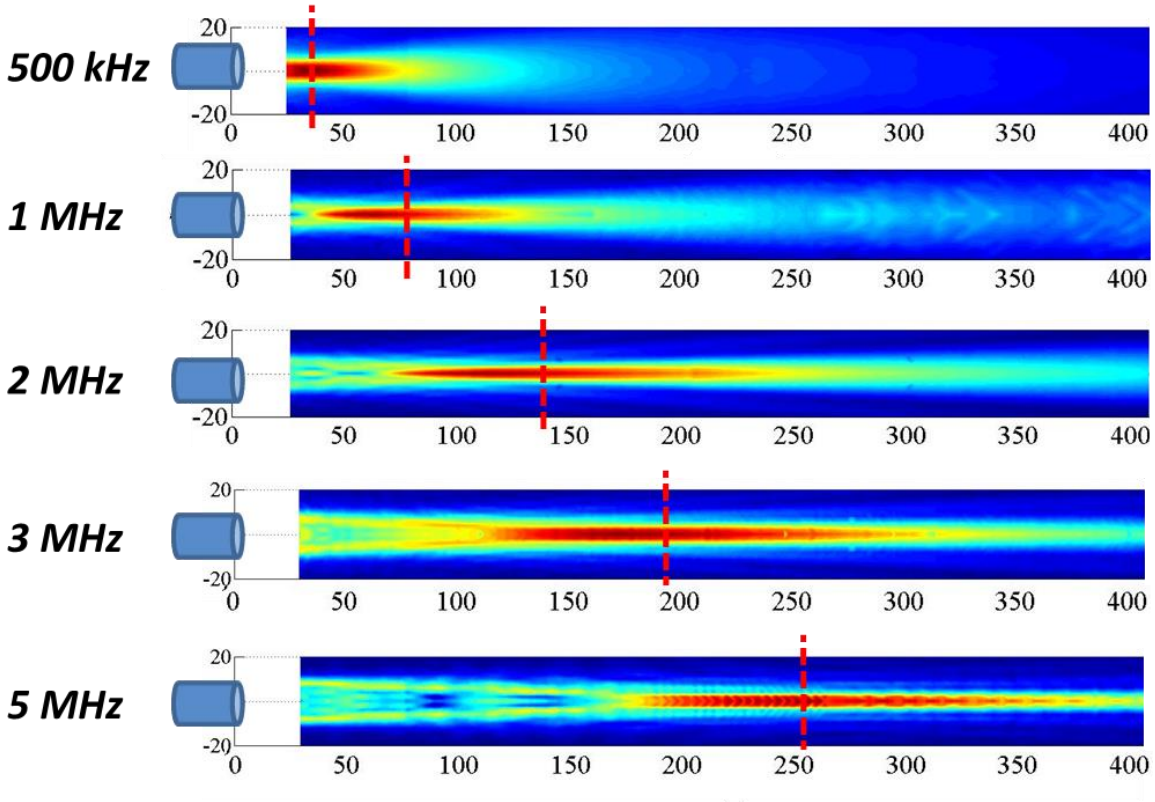

Figure 4.13. *Normalized pressure field maps for each frequency under investigation. Dashed vertical red lines highlight the highest pressure field conditions, for each frequency.*

The knowledge of the geometrical properties of the acoustic field of low intensity transducers, shown in this Section, were used to design the experimental set-up described in Section 4.3.

4.3 Experimental set-up

The ultrasonic set-up for cell stimulation (shown in Figure 4.14) is composed of a programmable wave generator (33220A, Agilent technologies) connected in series to a power amplifier and an immersion US transducer (WS75-0.5, WS75-2 and WS75-5, Ultran Group) with an active diameter of 19 mm. For the WS75-0.5 and the WS75-2 transducers, a radio frequency (RF) power amplifier (50 dB gain, 240L, Electronics & Innovation) was used. On the other hand, due to the very low electrical impedance of the WS75-5 transducer @ 5 MHz, a linear 15 MHz bandwidth power amplifier was used instead of the broadband RF amplifier to maximize the power transfer to the ultrasonic transducer [112]. The transducer and the sample were coaxially aligned in a

small tank of deionized and degassed water of dimension 500x100x120 mm. A linear rail allowed movement of the sample along the beam axis of transducer to enable alignment of the cells at the location of the axial maximum of the pressure field. To enhance the reliability of the studies all cell stimulation experiments were performed in deionized and degassed water with samples positioned at the point of maximum pressure (dashed vertical red lines, in Figure 4.13).

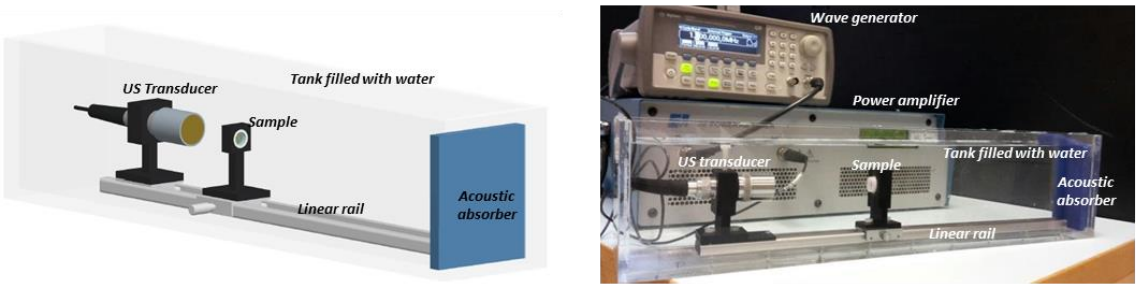

Figure 4.14. *Schematic diagram (left) and picture (right) of the experimental set-up used for cell stimulation experiments.*

The set-up was designed and built up trying to minimize the typical exposure errors that normally affect a vast majority of current systems used for *in vitro* US cell stimulation (see Section 4.1). To this purpose, an US transparent cell culture well was needed in order to guarantee a known and reproducible US cell exposure. A multilayered structure for cell cultures was hence designed (Figure 4.15). It consists of a thin polystyrene membrane (25 µm thickness, Goodfellow) secured within a cylindrical well (1 cm in diameter) of polytetrafluoroethylene and containing the cell culture medium. Secure mounting of the structure was guaranteed by a custom perforated cup produced by 3D printing (Projet HD 3000, 3D Systems) that allows US waves to reach the membrane directly. Moreover the cup houses an agarose disk during the culture, which is used to give the cells a uniform support. The disk was removed during US stimulation. Thanks to its small thickness (much smaller than the US wavelengths that range from 2.96 mm @ 500 kHz to 0.3 mm @ 5 MHz), the polystyrene membrane doesn't attenuate US waves. The transmission through the membrane was measured by using a through-transmission technique (see Section 3.2.1) in which the signal was acquired in the absence and presence of the membrane interposed between the emitting transducer and the hydrophone. The transmission

values for the different frequencies are as follows: (1) f = 500 kHz, transmission: 99.86%; (2) f = 1 MHz, transmission: 99.74%; (3) f = 3 MHz, transmission: 99,36%; (4) f = 5MHz, transmission: 99,10%. For these measurements, the transducers were driven with a sinusoidal tone burst of 40 cycles at frequency f, in presence and absence of the sample. Then, the root mean squares of the two corresponding acquired signals were calculated and divided by each other For all measurements, signals were collected 10 times so as to significantly reduce the effect of noise.

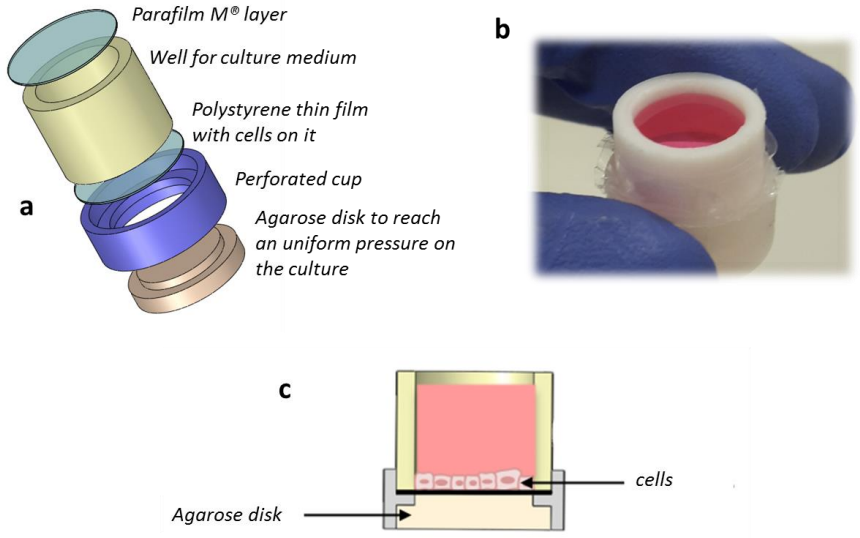

Figure 4.15. *US-transparent cell culture well. a) Exploded view of the culture well, showing its components. The polystyrene membrane is featured by a thickness of 25 µm, thus resulting transparent to US waves. Figure (b) and schematically representation (c) of a fully assembled well, filled with cell culture medium.*

In order to avoid possible reflections from the sides of the well, the set-up and especially the culture well, were designed so that the entire US beam (more than the 6 dB beam cross-sectional area) crosses the full membrane on which the cells are cultured (see Figure 4.16: the black dashed line indicates the sample diameter).

Before use, all parts of the wells were washed with Ethanol 70% (Sigma Aldrich® Corporation) and ultrapure MilliQ® water (Merck Millipore) and exposed to UV light for 30 min; then all components were assembled under sterile conditions. In order to avoid liquid leakage, UV sterilized Parafilm M® (Bemis Company) was used as a gasket to be placed on the opposite side of the well, to seal it during stimulation. Sterile agarose disks (2% wt/vol, Sigma Aldrich® Corporation) were prepared in the autoclave. Once removed from the autoclave, the solution was allowed to cool to 45 ºC, when

Penicillin/Streptomycin (PEN/STREP, Gibco™ - Thermo Fisher Scientific) and Amphotericin B (Sigma Aldrich® Corporation) were added to the agarose solution, to a final concentration of 1% each. The solution was then casted into a disk and left to set.

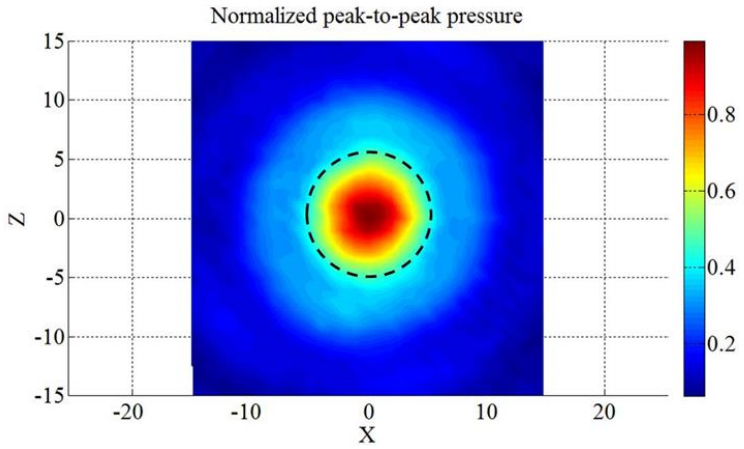

Figure 4.16. *Example of a transverse (X and Z are the two radial directions) normalized peak-to-peak pressure map at the target axial distance (Y=61.5 @ 1MHz). Black dashed line indicates the dimension of the circular membrane in the samples | diameter = 10 mm. Image coordinates are expressed in [mm].*

The polystyrene membrane, within the assembled wells, was then treated with oxygen plasma (Colibrì, Gambetti Kenologia S.r.l.; parameters: 100% O2, 50 s at 50 W and 0.5 mBar), to make it hydrophilic and to promote the formation of a stable protein coating. The membrane was incubated for 6 h at 37 °C with 100 µL of a Collagen Type I solution from rat tail (Sigma Aldrich® Corporation, St. Louis, Missouri, USA), diluted in sterile water (100 µg/mL). After the incubation period, the liquid was removed and the membrane was left to dry overnight. Just before cell seeding, the wells were exposed again to UV light for 30 min. This protein coating process was performed to improve cell attachment to the polystyrene membrane.

4.4 C2C12 muscle cell Ultrasound stimulation

None of the studies about muscle cells regeneration reports an *in vitro* systematic investigation of the effects of LIPUS exposures at different frequencies and intensities [110]. This was conducted in this study by exploiting the tunable stimulation system with an US-transparent cell culture well described above (Section 4.3), thus enabling a correlation between the US doses and the triggered bioeffects.

A highly controlled LIPUS stimulation on C2C12 cells was exploited by comparing 4 different frequencies (500 kHz, 1 MHz, 3 MHz and 5 MHz) and 3 different intensities (250, 500 and 1000 mW/cm^2) and quantifying the triggered bioeffects for the different conditions, in terms of cell proliferation and differentiation.

The frequencies and the intensities chosen are the ones investigated in several *in vitro* and *in vivo* studies, focused on US-triggered bioeffects on muscles. However, such studies have been performed in different conditions and using different set-ups. Consequently, the results available in the state-of-the-art are hardly comparable. The novelty of this study consists of a direct comparison of the effects produced by different stimulation frequencies on muscle cells, by using the same set-up and by minimizing possible exposure inaccuracies.

The C2C12 cell line (ATCC® CRL1772™, ATCC®, Manassas) was used in this study. It is a subclone of the mouse myoblast cell line established by D. Yaffe and O. Saxel [114] which can differentiate, forming contractile myotubes and characteristic muscle proteins. C2C12 cells were cultured and propagated in vented flasks to near 80% confluence. The proliferation medium was composed of high-glucose Dulbecco's Modified Eagle's Medium (DMEM, Gibco™ - Thermo Fisher Scientific) added with Fetal Bovine Serum (FBS, Gibco™- Thermo Fisher Scientific) to a final concentration of 10%, and PEN/STREP to a final concentration of 1%. To harvest cells, the medium was removed and the cells were washed twice with PBS (Gibco™- Thermo Fisher Scientific) and trypsinized for 2-3 min at 37 °C (trypsin solution: 0.25% w/v Trypsin - 0.53 mM EDTA, Gibco™ - Thermo Fisher Scientific). Trypsin was inhibited by adding complete medium, and removed by centrifuging the cells (2500 rpm, 7 min, EBA 20 centrifuge, Hettich Lab Technology). The cells were then re-suspended and seeded in the wells for experiments at the desired density.

For proliferation tests, cells were seeded at a density of 10,000 cells/cm^2 and kept in culture for 24 h. 12 h after the US treatment, these cells were harvested using trypsin and centrifuged to form a cell aggregate (pellet). Then the liquid above the pellet (surnatant) was removed and the pellet was washed twice with PBS. Finally, sterile milliQ water was added and cells underwent two freeze-thaw cycles to lyse cell

membranes. The lysates were analyzed using the Quant-iT™ PicoGreen® dsDNA Assay (Invitrogen™ - Thermo Thermo Fisher Scientific) to quantify double-stranded DNA (dsDNA).

For differentiation tests, cells were seeded at a density of 50,000 cells/cm^2 and kept in culture for 24 h, after which they reached confluence. Then cells were switched to differentiation medium, composed of high-glucose DMEM added with FBS to a final concentration of 1%, PEN/STREP to a final concentration of 1% and 1% of Insulin-transferrin-sodium selenite media supplement (ITS, Sigma Aldrich® Corporation). The medium was changed once per day for 7 days. 24 h after the last stimulation, the cells were fixed with a paraformaldehyde (Sigma Aldrich® Corporation) solution in PBS (4% wt/vol) for 15 min, than permeabilized with 0.1% Triton X-100 (Sigma Aldrich® Corporation) in PBS for 15 min. The cells were then stained for actin fibers with Fluorescein Isothiocyanate Labeled Phalloidin (Sigma Aldrich® Corporation) and for nuclei with Hoechst 33342 (Molecular Probes™ - Thermo Fisher Scientific) for a further 15 min. Fluorescence images were obtained by means of a UV-VIS microscopy analysis (ECLIPSE Ti-E, Nikon Corporation). Images of the blue channel (nuclei) and the red channel (actin) were acquired for each sample at 10X magnification at 5 different locations in the well. Differentiation was evaluated by quantifying length and width of the myotubes formed, by means of the ImageJ® software (National Institutes of Health, available at *https://imagej.nih.gov/ij/*) and by computing the fusion index. This was calculated for each image, as the number of nuclei in multinucleated structures divided by the total number of nuclei in the image. Moreover, images at 4X magnification of the red channel (actin) were taken for each sample, in order to have an overall low-magnification qualitative view of the different sample types.

The protocol for proliferation tests consisted of a single LIPUS stimulation performed 24 h after cell seeding. The evaluation of the effects produced was carried out 12 h after such single US exposure (Figure 4.17-a). The protocol for differentiation tests, instead, consisted of LIPUS exposures repeated daily for 7 days, associated with medium renewals for 7 days, starting 24 h after cell seeding. The effects of the treatment were evaluated 24 h after the last US stimulation (Figure 4.17-b).

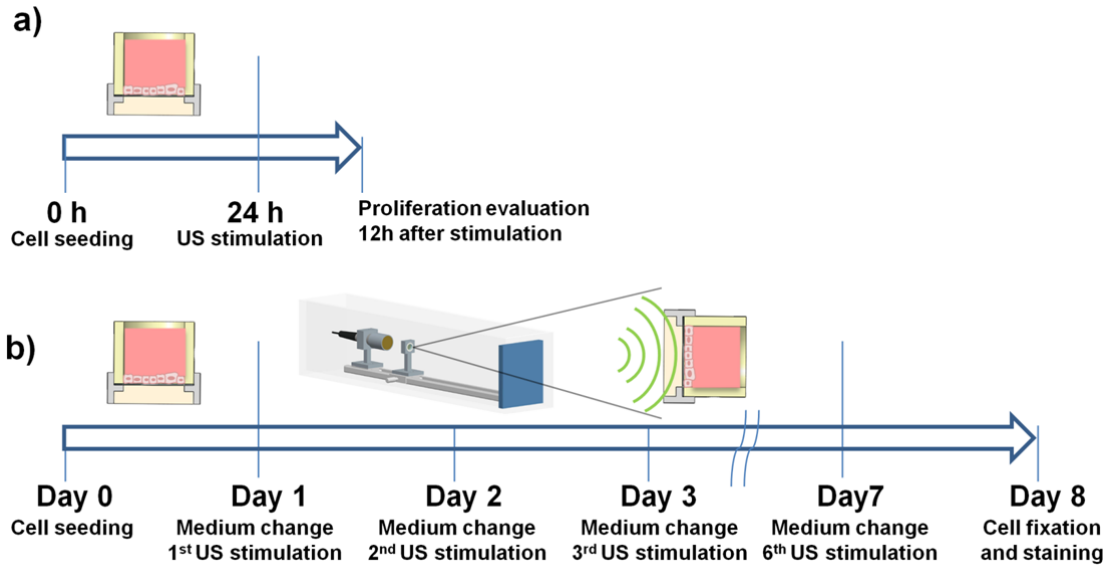

Figure 4.17. *Stimulation protocols for C2C12 cells. LIPUS stimulation protocol depiction for proliferation (a) and differentiation (b) tests.*

In both proliferation and differentiation tests, each LIPUS exposure lasted for 5 min, with a pulse repetition frequency of 1 kHz and a duty cycle of 20%. As a first trial, the following exposure conditions were tested: (1) f = 500 kHz, SPPA intensity = 500 mW/cm^2 (peak negative pressure, P_n= 122 kPa); (2) f = 1 MHz, SPPA intensity = 500 mW/cm^2 (P_n= 122 kPa); (3) f = 3 MHz, SPPA intensity = 500 mW/cm^2 (P_n= 122 kPa); (4) f = 5 MHz, SPPA intensity = 500 mW/cm^2 (P_n= 122 kPa); (5) control without stimulation. The water in the stimulation tank was kept at room temperature (~ 28°C). All samples were immersed in the tank for the duration of the stimulation task. Control samples were also immersed for the same time, although not stimulated, so to exclude possible manipulation- and temperature-dependent effects on the final results.

After evaluating the optimal frequencies for maximum cell proliferation and differentiation, the same protocols were repeated at those frequencies at each of the following SPPA intensities: (1) 250 mW/cm^2 (P_n= 86 kPa) (2) 500 mW/cm^2 (P_n= 122 kPa) and (3) 1 W/cm^2 (P_n= 172 kPa). Three and four independent samples per exposure condition were analyzed for proliferation and differentiation tests, respectively.

4.4.1 C2C12 proliferation results

As previously mentioned, in order to assess the bioeffects triggered by different US exposure conditions on C2C12 cell proliferation, the quantification of dsDNA was

performed 12 h after US stimulation. The aim of the first set of experiments was to identify the ultrasonic frequency that maximized this cellular process. Thus 4 different US frequencies were tested, at a constant intensity of 500 mW/cm^2. Additionally non-stimulated samples served as control. As shown in Figure 4.18-a, an increase of dsDNA (and consequently of cell proliferation) was found in all samples treated with US in comparison to the non-stimulated ones. Such differences were statistically significant for exposures at 500 kHz (p = 0.0097), 1 MHz (p = 0.0274), 3 MHz (p < 0.0001), but not for 5 MHz. Moreover, a significant difference was observed between samples treated with US at 3 MHz and at 5 MHz, (p = 0.0080). Samples stimulated at 3 MHz showed an amount of dsDNA that appeared higher in comparison with samples stimulated at 500 kHz and 1 MHz. However, the differences with such sample types were not statistically significant. The p value between 3 MHz and 500 kHz samples was 0.1265, while the one between 3 MHz and 1 MHz samples was 0.0514.

However, the results suggested quite clearly that 3 MHz was the stimulation frequency that maximized cell proliferation; for this reason, it was selected for the following experiments, in which the frequency was kept constant at 3 MHz and different SPPA intensity values were evaluated, so to identify the optimal LIPUS exposure to maximize proliferation. Figure 4.18-b shows the obtained results. The sample stimulated at the highest intensity (1 W/cm^2) showed a significant increment in the dsDNA with respect to both samples stimulated at 250 mW/cm^2 and at 500 mW/cm^2 (p = 0.0081 and p = 0.0168, respectively). From these results, it appears that the optimal LIPUS exposure conditions, among those tested, which maximize proliferation are 3 MHz and 1 W/cm^2.

All data obtained underwent a non-parametric statistical analysis using the Kruskal-Wallis post-hoc test and the Dunn's multiple comparison test in order to evaluate significant differences among the samples. Results were considered statistically different for p-values ≤ 0.05. Although it is rather difficult to compare results obtained with different stimulation set-ups, it must be mentioned that Puts et al. [115, 116] demonstrated that stimulation at 3.6 MHz, although at lower intensities than the ones tested in this study, led to an increase in the activator protein-1 (AP-1) with respect to non-stimulated C2C12 cells. AP-1 is a heterodimeric protein activated by the

mechanical tension applied to cells, which has a pro-mitogenic function. Thus, in this study, it was possible to hypothesize that the optimal exposure conditions found in this work maximized the activity of this protein, probably in synergy with other extracellular and intracellular mechanisms, such as the Rho A, ROCK and ERK pathways [117].

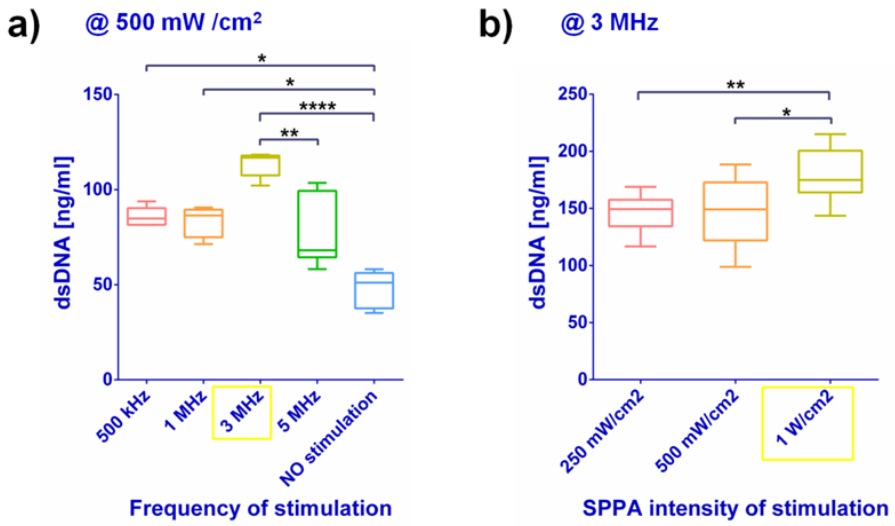

Figure 4.18. *Proliferation tests. a) Box and whiskers plots representing the median values and interquartile ranges of the dsDNA concentrations found in the cell lysates of samples subjected to LIPUS treatment at an SPPA intensity of 500 mW/cm² and at different frequencies, and non-stimulated samples (whiskers represent the maximum and minimum values obtained). b) Box and whiskers plots of the dsDNA concentrations found in samples subjected to LIPUS treatment at the fixed frequency of 3 MHz and at different SPPA intensities. In proliferation experiments, three independent samples were analyzed for each sample type. * = p < 0.05, ** = p < 0.01, **** = p < 0.0001.*

4.4.2 C2C12 differentiation results

The effects of LIPUS at different frequencies on C2C12 cell differentiation were evaluated after 7 days of stimulation in differentiation medium. First, 4 different US frequencies were tested, by keeping the same intensity of 500 mW/cm², in addition to non-stimulated control samples. Figure 4.19-a and Figure 4.19-b show fluorescence images of the myotubes formed. In particular, Figure 4.19-a shows low-magnification (4X) images of actin, stained in red for each stimulation condition, while Figure 4.19-b shows images at 10X magnification for each stimulation conditions with nuclei stained in blue and actin in red. Figure 4.19-c shows the results of a quantitative morphological

analysis of myotube width i) and length ii) and of the cell fusion index iii). A statistically significant enhancement of myotube length (Figure 4.19-c ii)) and width (Figure 4.19-c i)) was found in samples treated with US at a frequency of 1 MHz with respect to all other treatments and to non-stimulated controls ($p < 0.0001$). No significant differences were found in myotube width (Figure 4.19-c i)) between 500 kHz, 3 MHz, 5 MHz treatments and non-stimulated samples, while for myotube length (Figure 4.19-c ii)) a difference was observed by comparing 5 MHz samples with control samples and also with 500 kHz samples ($p = 0.0364$ and $p = 0.0019$, respectively). 500 kHz samples and 3 MHz samples also differed slightly ($p = 0.0208$).

Analysis of the fusion index (Figure 4.19-c iii)) revealed an increase of this parameter in the samples treated at a frequency of 1 MHz. This increment was statistically significant in comparison with the samples stimulated at 500 kHz and 5 MHz and with control (non-stimulated) samples ($p < 0.0001$). The difference between samples stimulated at 1 MHz and those stimulated at 3 MHz was not statistically significant ($p = 0.0814$), although samples stimulated at 1 MHz showed a clear tendency to develop myotubes with higher fusion index levels.

Overall, the absolute fusion index values obtained (maximum median value obtained for 1 MHz = 21.07%) are in general smaller respect to the ones that can be found in some literature examples. This can be due to the sub-optimal culture conditions, in terms of substrate and extracellular environment features, used in this study. The culture well was in fact designed with the main aim to provide an US-transparent interface, so to properly correlate the bioeffects to the actual US delivered. To improve skeletal muscle differentiation, a variety of stimuli are needed, such as chemical [118], topographical [119], mechanical [120], electrical [121] and intracellular ones [46].

Overall, the LIPUS treatment at a frequency of 1 MHz showed an enhancement in myotube development in comparison with the other conditions. Thus, it was identified as the optimal frequency to induce skeletal muscle differentiation.

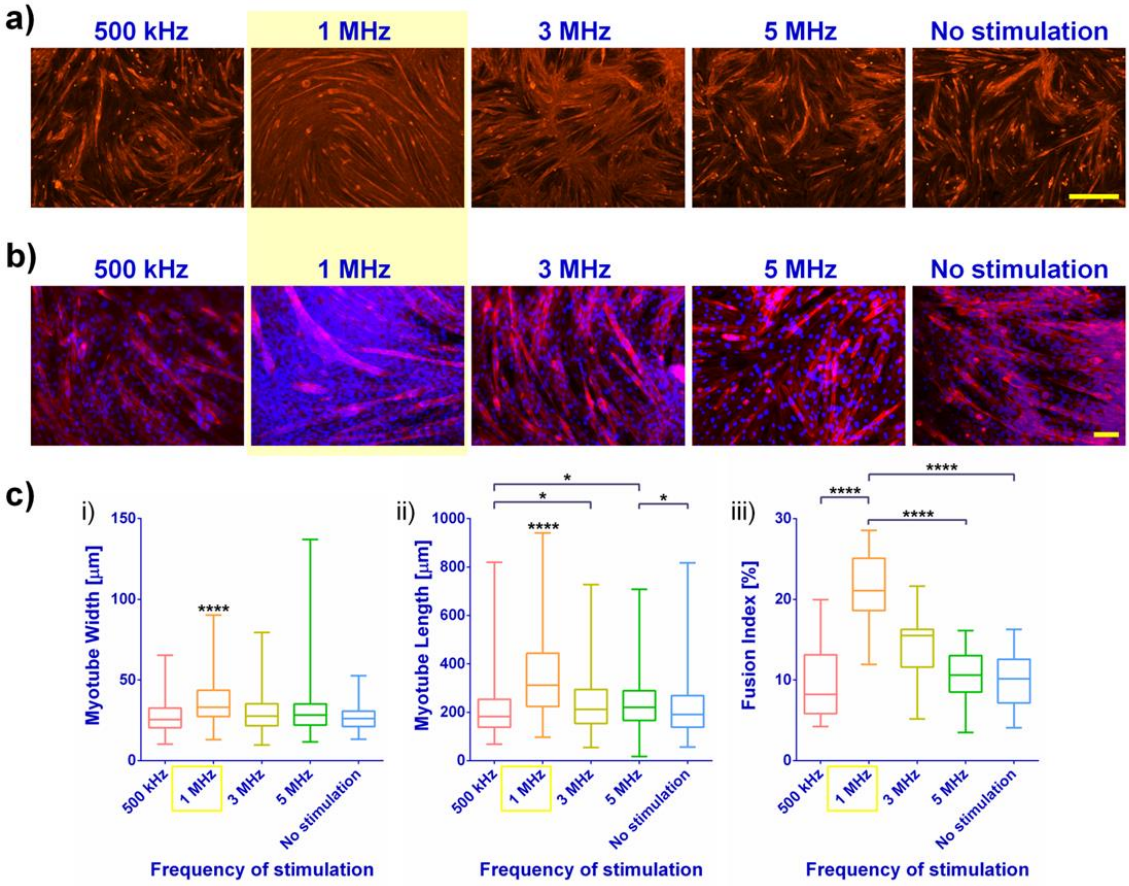

Figure 4.19. *Differentiation tests - different frequencies (@ I = 500 mW/cm^2). a) Fluorescence images at 4X magnification of differentiated C2C12 cells after 7 days of daily LIPUS stimulation and differentiation medium renewal. Control samples underwent only medium renewal. Different stimulation frequencies were tested, at a fixed SPPA intensity of 500 mW/cm2. Actin filaments are shown in red (scale bar = 500 µm). b) Fluorescence images at 10X magnification of differentiated C2C12 in the same stimulation conditions of point a), showing nuclei in blue and actin in red (scale bar = 100 µm). c) Box and whiskers plots representing the median values and interquartile ranges of the 3 parameters used to quantify cell differentiation, namely myotube width i), myotube length ii) and fusion index iii), obtained for the different stimulation frequencies tested, at a fixed SPPA intensity of 500 mW/cm2 (whiskers represent the maximum and minimum values obtained). In differentiation experiments, four independent samples were analyzed for each sample type. * = p < 0.05, ** = p < 0.01, **** = p < 0.0001.*

The following tests were thus based on 3 different spatial peak pulse average (SPPA) intensities values (250 mW/cm^2, 500 mW/cm^2 and 1 W/cm^2) at a constant frequency of 1 MHz. As shown in the fluorescence images of Figure 4.20-a and Figure 4.20-b and in the quantitative analysis of Figure 4.20-c, the SPPA intensity of 500 mW/cm^2 appeared to increase all the 3 differentiation parameters (Figure 4.20-c i), ii), iii)) with respect to the other two intensities tested. Such differences were significant, for all parameters, in comparisons between 500 mW/cm^2 samples and 1 W/cm^2 samples (p < 0.0001). Significant differences were also found between 500 mW/cm^2 samples and 250 mW/cm^2 samples concerning myotube width (Figure 4.20-c i)) and fusion index

(Figure 4.20-c iii)) (p < 0.0001 and p = 0.0134, respectively), but not concerning myotube length (Figure 4.20-c ii)) (p = 0.2000). Finally, a significant difference was also found by comparing myotube width (Figure 4.20-c i)) between 250 mW/cm^2 samples and 1 W/cm^2 samples (p = 0.0097).

Overall, these results suggest that 1 MHz and 500 mW/cm^2 are the optimal LIPUS exposure conditions, among the ones tested, to maximize C2C12 cell differentiation.

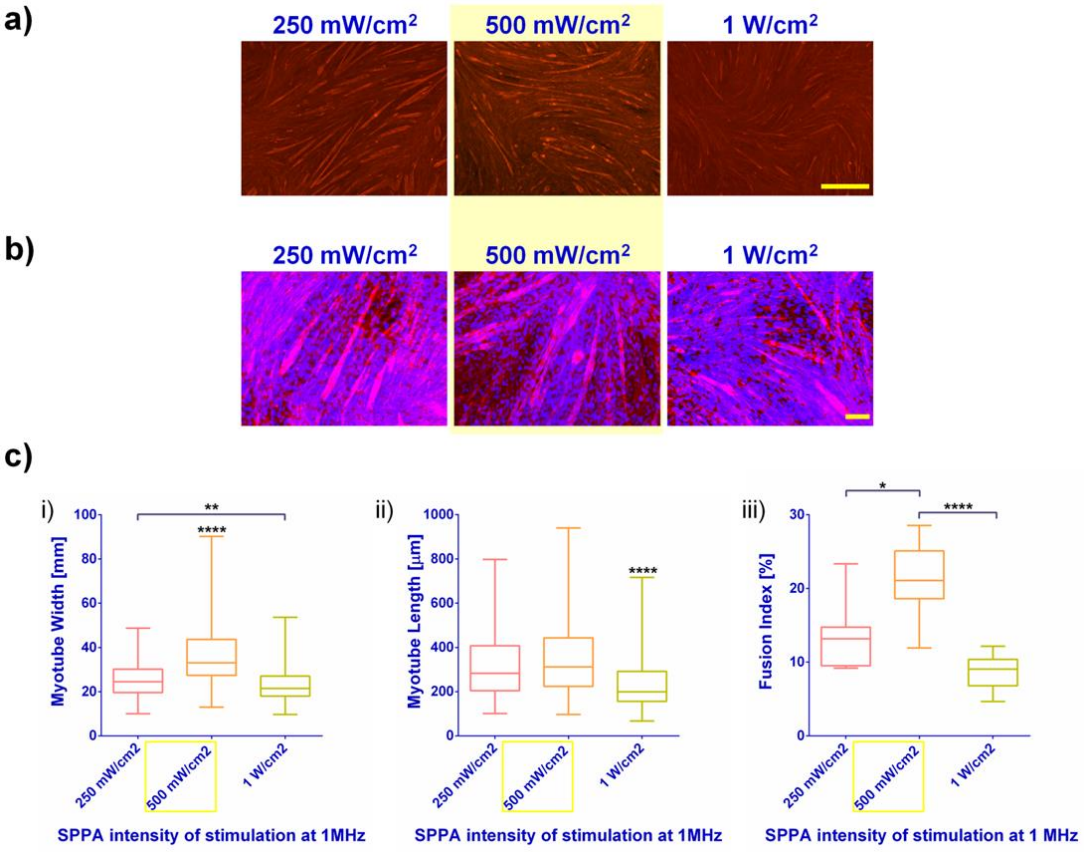

Figure 4.20. *Differentiation tests - different intensities (@1 MHz). a) Fluorescence images at 4X magnification of differentiated C2C12 cells after 7 days of daily LIPUS stimulation and differentiation medium renewal. Stimulation was performed at the fixed frequency of 1 MHz and at different SPPA intensities (scale bar = 500 µm). b) Fluorescence images at 10X magnification of differentiated C2C12 in the same stimulation conditions of point a), showing nuclei in blue and actin in red (scale bar = 100 µm). c) Box and whiskers plots representing the median and interquartile ranges of myotube width i), myotube length ii) and fusion index iii), obtained for the treatments at the fixed frequency of 1 MHz and at different SPPA intensities (whiskers represent the maximum and minimum values obtained). In differentiation experiments, four independent samples were analyzed for each sample type. * = p < 0.05, ** = p < 0.01, **** = p < 0.0001.*

Considering the different *in vitro* studies on cell differentiation and US stimulation, some of them showed an increase in term of myogenin or desmin protein content and gene expression that is representative of an increase of differentiation. Among these studies, Abrunhosa et al. [122] reported an analysis of the myotube morphology that is

similar to the one presented in this study, although with a different cell line. The bioeffects obtained in this work, in terms of fusion index and myotube width, are higher than the ones achieved by Abrunhosa et al. [122]. This group used similar US stimulation parameters, although they found better results in continuous rather than in pulsed mode. This discrepancy could be due to the different US stimulation set-ups used and thus a direct comparison is difficult.

There are different cellular pathways involved in the enhanced muscle differentiation due to US exposure. Ikeda et al. [123] showed that US activates phosphorylation of p38 MAPK. Although they demonstrated that the US stimulation of C2C12 cells pushes their differentiation towards an osteoblast and/or chondroblast lineage, it is well known that phosphorylation and activity of the α and β isoforms of p38 MAPK is gradually induced during the differentiation of myoblast [124]. Moreover, a change in its activity affects the transcriptional pattern of muscle-specific genes, indicating that it may modulate transcriptions factors involved in the differentiation process [124-126].

Calcium ions may also play an important role: they are in fact essential for muscle cell contraction and differentiation. These ions can enter cells through stretch-activated channels, which are strictly connected to the cell stress fibers. Porter et al. [127] reported that calcium channel blockade decreases both the number and the size of differentiated myotubes. US may be a trigger for an increased activation of such channels.

C2C12 cell line consists of murine myoblast cells derived from satellite cells, whose behavior corresponds to the one of the progenitor lineage. It is considered a good model of skeletal muscle development and it is widely used to this purpose [128]. C2C12 cells are indeed a subclone of C2 myoblasts that can differentiate in culture, and it is known that they reproduce a number of skeletal muscle features [129], representing a reliable model for the study of muscle tissue in a variety of normal and pathological conditions.

For these reasons the results obtained could partly clarify why some *in vivo* US-based experiments reported in the literature showed significant muscle regeneration, while others did not. In fact, a significant improvement of muscle regeneration after injuries

was observed in some studies featured by a stimulation frequency around 1 MHz [130-132]. Other studies that did not report significant bioeffects on muscles due to US stimulation, were based on stimulation frequencies around 3 MHz [133, 134]. It is obviously premature to affirm that a strong correlation can be drawn between our findings and these previous studies, because *in vivo* stimulation conditions varied between studies in terms of intensity and duration and also due to the well known fact that attenuation in tissues is frequency-dependent and varies between tissues [135]. Since the same free field intensity may result in different conditions at the target tissue, further investigation is needed to translate the results obtained in this study to in vivo settings, with the aim of evaluating the bioeffects triggered by US on muscle tissues.

4.4.3 Temperature measurements

Temperatures increase inside the cell culture well due to US stimulation was evaluated by means of a fine wire thermocouple (COCO-001, OMEGA, Stamford, Connecticut, USA), positioned inside the well for each US stimulation condition (Figure 4.21). A type T thermocouple (resolution of 0.1 C°) with a diameter of 25 µm was selected in order to minimize scattering and reflections of the US wave and to minimize the consequent errors in temperature measurements, which could occur using probes with typical dimensions equal to or greater than 1/2 of the square root of the wavelength [136]. Temperature data were acquired at 1 Hz of sampling frequency by means of a thermocouple measurement device (USB-TC01, National Instruments Corporation). Tests were performed at room temperature (~ 28 °C). As mentioned, few works associate temperature measurements to the US stimulation regimes used, but this is crucial to discriminate between thermal and non-thermal (mechanical) bioeffects.

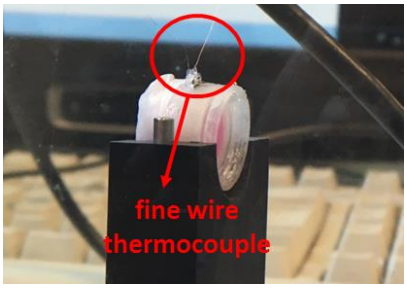

Figure 4.21. *Fine wire thermocouple measurements in the US-transparent cell culture well.*

The results of temperature measurements in our case are reported in Figure 4.22. Results show that for the different conditions tested - intensity fixed at 500 mW/cm^2 and different frequencies (Figure 4.22-a), frequency fixed at 3 MHz and different intensities (Figure 4.22-b), and frequency fixed at 1 MHz and different intensities (Figure 4.22-c), all temperature rises were equal to or lower than 0.6 °C. These findings are in line with the typical temperature rise reported in LIPUS stimulation (< 1 °C) [97]. Thus, our experimental conditions can be classified as non-thermal US exposures [137]. Moreover, it must be pointed out that a contribution of this temperature increase could be due in part to viscous heating artifacts. In fact, viscous-free sensors weren't used, such as thin film thermocouples, for these measurements [138]. This probably led to an overestimation of the real temperature rise within the culture wells, due to US stimulation. Since the temperature increase was almost the same for all the different frequencies tested (Figure 4.22-a), it can be affirmed that the different results obtained concerning proliferation and differentiation at diverse stimulation frequencies are surely due only to non-thermal bioeffects.

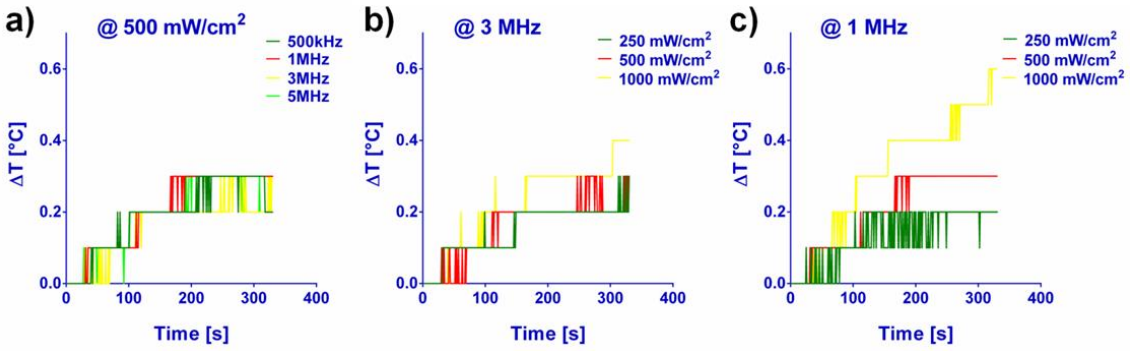

Figure 4.22. *Temperature measurements. a) Graph representing the temperature variations inside the cell culture well for the following stimulation conditions: 500 kHz, 1 MHz, 3 MHz, 5 MHz, at an SPPA intensity of 500 mW/cm^2. b) Graph representing the temperature variations due to LIPUS stimulation at 3 MHz (the optimal one in proliferation tests) and 250 mW/cm^2, 500 mW/cm^2 and 1 W/cm^2. c) Temperature variations measured during LIPUS stimulation at 1 MHz (for the optimal one in differentiation tests) and 250 mW/cm^2, 500 mW/cm^2 and 1 W/cm^2*

Scientific production (Chapter 4)

Publications on Internationals journals

- A. R. Salgarella, **A. Cafarelli**, L. Ricotti, L. Capineri, P. Dario, A. Menciassi. "Optimal ultrasound exposure conditions for maximizing C2C12 muscle cell proliferation and differentiation". *Ultrasound in Medicine and Biology, April 2017*;

- L. Ricotti, **A. Cafarelli**, V. Iacovacci, L. Vannozzi, and A. Menciassi. "Advanced Micro-Nano-Bio Systems for Future Targeted Therapies". *Current nanoscience, 2014*;

Patents

- **A. Cafarelli**, L. Ricotti, A. Menciassi. Italian patent: "Sistema di stimolazione ad ultrasuoni di un campione in vitro", filing no. 102016000052583, filing date: May 2016.

Papers presented at International conferences

- A.R. Salgarella, L. Ricotti, G. Giudetti, J. Kronek, M. Righi, A.Cutrone, **A.Cafarelli**, A. Zahoranová, P. Šramková, D. Treľová, S. Bossi, S. Micera, I. Lacík, A. Menciassi. "Advanced nano-doped materials for long-term neural interfaces". *15th International Conference on Nanotecnology (IEEE NANO)*. Rome, July, 2015;

5 High Intensity Focused Ultrasound for cancer treatment

US can be focused deep into the body with extreme precision thus causing tissue necrosis in the target volume. This technology is generally known as High Intensity Focused Ultrasound (HIFU) or sometimes Focused Ultrasound (FUS) surgery.

The use of HIFU in combination with magnetic resonance (MR) or ultrasound (US) monitoring was already demonstrated to be effective for the treatment of various malignancies in organs such as pancreas, prostate, liver, kidney, breast and bone [4]. Also other applications, such as the treatment of brain pathologies, are rapidly gaining acceptance in clinics.

However, there are some considerations that limit clinical applications of FUS, *i.e.*, beam propagation in heterogeneous tissues, poor estimation of the US dose at the target, long treatment duration, lack of flexibility and limited effectiveness in moving organs.

A flexible robotic FUS system was designed and developed for overcoming these limitations and therefore improving the diffusion of FUS into routine procedures. The use of a robotic-assisted approach for FUS may alleviate the problems related to the predictability and repeatability of current procedures by enhancing accuracy, safety and flexibility of the treatment.

In this Chapter, after briefly exploring the main principles of HIFU and highlighting the main limitations of current systems (Section 5.1), an innovative robotic platform for FUS is described, both in terms of architecture and workflow of the procedure (Section 5.2).

Though the whole problem of using robotic-FUS regards many different competence and components (robotic guidance, US imaging, etc.), this PhD thesis focuses on the therapeutic part, and the assessment of the overall procedure. A dedicated 16 channels annular array HIFU transducer was characterized and integrated in the platform (Section 5.3) and the functionalities of the system were assessed *in-vitro* and *ex-vivo* with dedicated models for targeting and monitoring, both in static and dynamic conditions (Section 5.4).

5.1 HIFU: background

As suggested by the name, High Intensity Focused Ultrasound (HIFU) - sometimes referred also as Focused Ultrasound (FUS) surgery - is the term used to describe the use of a FUS beam of high energy for therapeutic purposes. US can target tissue deep in the body, producing a biological effect (*e.g*. tissue necrosis) only within the focal volume, while preserving surrounding tissues (Figure 5.1).

The fundamental principle is analogous to using a magnifying glass to focus beams of sun rays and burn a leaf for example. Focused transducer concentrates acoustic waves in a small region of the space (*i.e.* the focus), creating a region of high pressure deep in the body with high precision and accuracy and with minimal effects elsewhere.

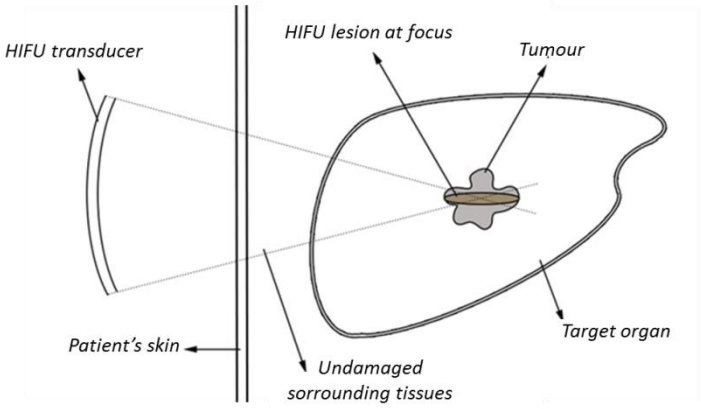

Figure 5.1. *Schematic illustration showing the principle of High Intensity Focused Ultrasound (HIFU) therapy. Figure readapted from Guo et al. 2012 [139].*

As already explained in Section 2.2.2, different biological effects can be produced at the target; protein denaturation [18] due to temperature rises (>56°C), histotripsy induced by inertial cavitation [19] or tissue fragmentation due to tissue boiling [140] are the typical mechanisms of tissue necrosis caused by HIFU.

The ability of FUS to induce tissue necrosis in tissues has long been recognized [141]. First applications of FUS were proposed in 1942 by Lynn [142] and Fry in 1950s [143] for non-invasively destroing target tissue within the body (*e.g.* brain). In the 1980's Coleman and Lizzie developed Sonocare CST-100, the first FUS system approved by the Food and Drug Administration (FDA), which was designed to treat glaucoma [144].

But, as shown in Figure 5.2, it's only from the 1990's that, thanks to developments of modern imaging modalities (MR and US), FUS underwent an exponential growth in

terms of number of clinical applications, treatment sites, number of patients treated and approvals (*www.fusfoundation.org*).

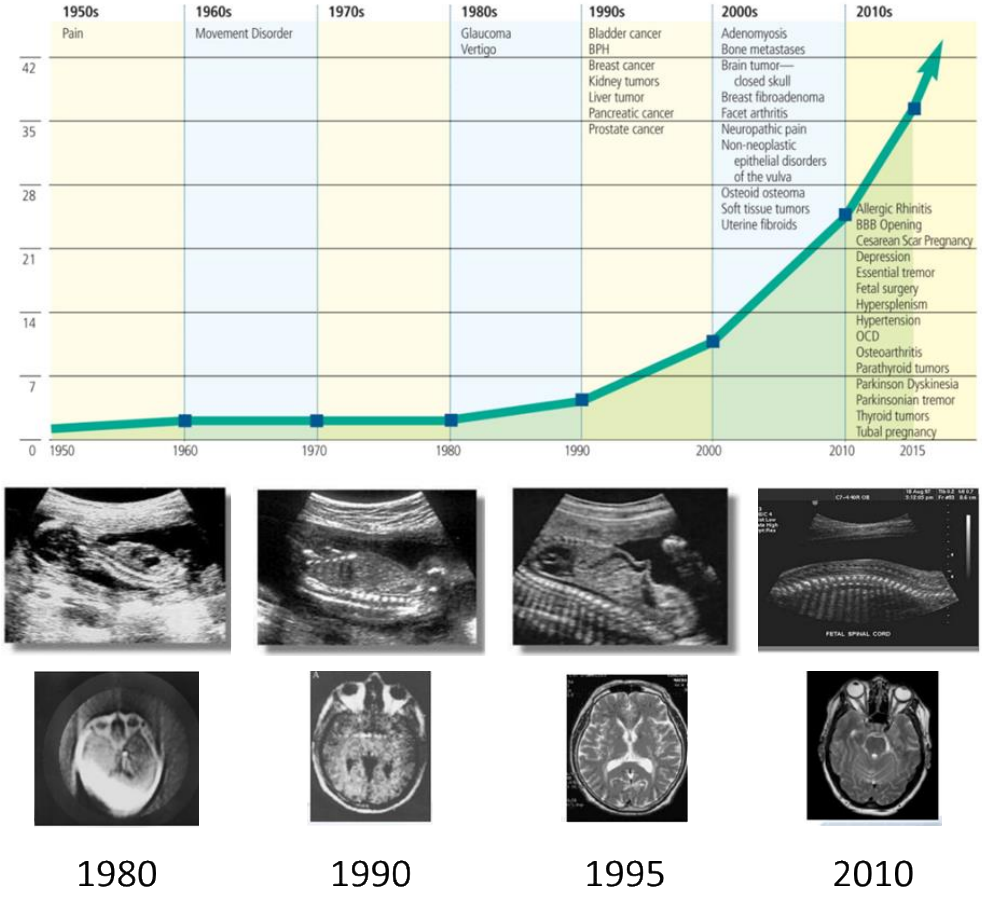

Figure 5.2. *Timeline of FUS clinical indications (first clinical trials or commercial treatments) in humans. The number of clinical indications for FUS has increased from just a couple of conditions before the 1990s to 35 in 2015, and several others are expected to be available in the near future. Last two lines represent the evolution of imaging modalities (a) US images, b) magnetic resonance images). Figure readapted form the FUS foundation website (www.fusfoundation.org) and from the lecture of Prof Jean-François Aubry at the Winter School on Therapeutic Ultrasound 2015.*

Three main categories of HIFU devices can be found in clinics: extracorporeal devices, interstitial devices and trans-rectal devices. Extracorporeal transducers are used to treat tumors through the skin, trans-rectal probes are designed to target prostate carcinomas, while interstitial devices are used to treat tumors in the esophagus and in the biliary duct.

For all of these categories, anatomical and/or functional imaging for precise targeting and treatment follow-up can be performed through two different imaging modalities: magnetic resonance (MR) or ultrasound (US).

Magnetic resonance and ultrasound guidance have both their pros and cons. Magnetic Resonance guided FUS (MRgFUS) systems offer high quality images and quantitative temperature maps [145], while Ultrasound guided FUS (USgFUS) devices guarantee the possibility to verify the treatment acoustic window, and an intrinsic higher frame rate that allows real-time therapy monitoring and can enable a compensation of physiological movements [146]. Compared to MR systems, US devices also have other advantages such as lower cost and system size.

Nowadays there are several applications for FUS, performed under MR guidance or US guidance, which are in various stages of development and adoption (Figure 5.3).

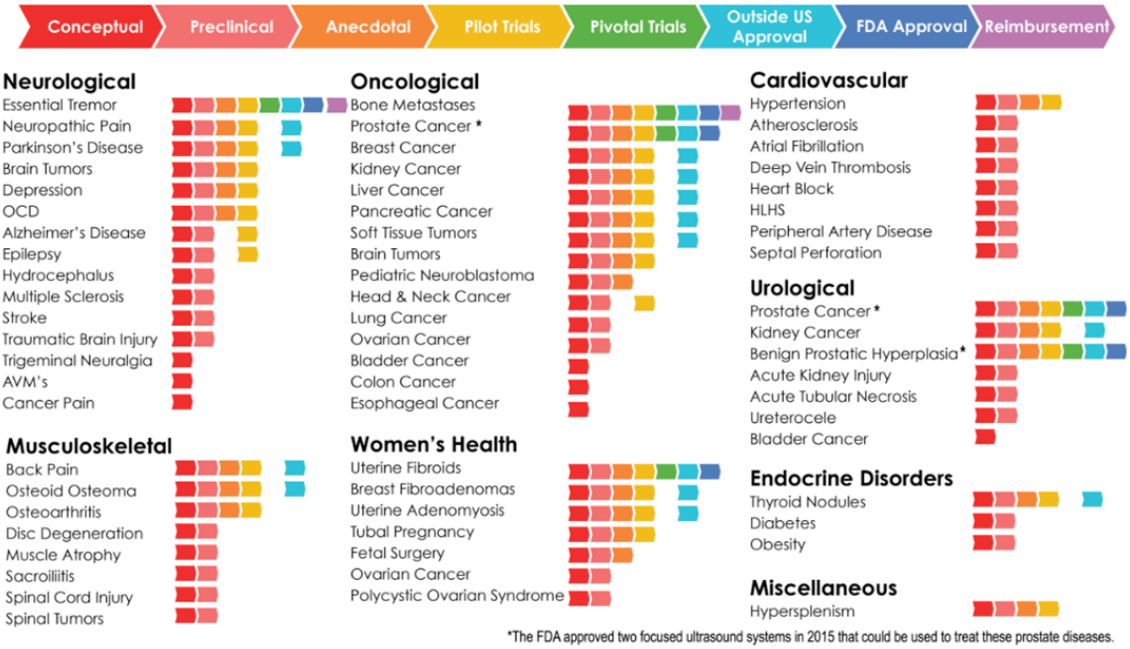

Figure 5.3. *State of the technology of FUS applications. Figure downloaded from the FUS Foundation website (www.fusfoundation.org) on March 30th 2017.*

Malignant tumors of breast, liver, kidney, pancreas and prostate have been successfully treated. FUS is also widely used for the treatment of uterine fibroids and for pain palliation of bone metastases [147]. Additionally, pre-clinical testing of image-guided FUS for target drug delivery (*e.g.* chemotherapy drugs) is also underway [148].

The last few years have also demonstrated the possibility to accurately target small regions within the brain under magnetic resonance guidance (transcranial magnetic resonance imaging-guided focused ultrasound, tcMRgFUS). The first study reporting a successful thermal lesioning of the thalamus was presented by Martin in 2009 [149]

and now tcMRgFUS represents a very promising technique for several neurological disorders such as brain tumors, essential tremor, depression, neuropathic pain, obsessive-compulsive disorder, tremor-dominant Parkinson's diseases and other neurodegenerative pathologies [150].

Focusing the attention on extracoporeal USgFUS systems, as also visible in Table 5.1, there are already some platforms that operate in clinical setting, such as the HAIFU JC (Chongqing Haifu Medical Technology Co. Ltd, Chongqing, China), EchoPulse (Theraclion, Malakoff, France) and Alpius (ALPINION Medical Systems, Seoul, Korea).

Manufacter	Nation	Device	Guidance (MR o US)	Clinical Application
Chongqing Haifu	China	Haifu JC	USgFUS	Breast cancer, kidney tumors, liver tumors, osteoid osteoma, pancreatic tumors, soft tissue tumors, uterine adenomyiosis, uterine fibroids
InSightec	Israel	ExAblate	MRgFUS	Back & neck pain, bone metastases, breast cancer, neurological disorders, osteoid osteoma, prostate diseases, uterine adenomyiosis, uterine fibroids
Phillips Healthcare	Netherlands	Sonalleve	MRgFUS	Uterine fibroids, bone metastases
Theraclion	France	THOne EchoPulse	USgFUS	Breast fibroadenoma, thyroid nodules
Alpinion Medical Systems	Korea	Alpius	USgFUS	Uterine fibroids
EDAP TMS	France	Ablatherm Focal One	USgFUS	Prostate diseases
SonaCare Medical	USA	Sonablate	USgFUS	Prostate diseases
EyeTechCare	France	EyeOP. EyeMUST	/	Glaucoma

Table 5.1*. Clinically approved FUS systems*

However, all these platforms present some limitations, which are listed as follows:

- ***lack of flexibility***: all these system are specific for one or at maximum a few clinical targets;
- ***2D imaging***: only one 2D imaging probe, mounted confocally to the HIFU transducer, is used for the guidance of the therapy;
- ***static targeting***: the technique is applied mainly on non-moving organs, or in some cases on moving targets but in combination with respiratory gating or some form of breath hold;
- ***inability to monitor the treatment during sonication***: the lesion progress cannot be monitored during the sonication because the US images are completely distorted by the noise generated by commercial HIFU transducer operating in continuous mode;
- ***time consuming procedure***: treatments are not automatized and therefore the total duration of the procedure is long (*e.g*. few hours). As an example, in a study of a preliminary experience using HIFU on patients with advanced stage of renal malignancy, a median tumor size of 8.7 cm took a therapy time of about 5.4 hours [151].

In this framework, the FUTURA (Focused Ultrasound Therapy Using Robotic Approaches) project (*www.futuraproject.eu*) stemmed from the idea to develop an autonomous, multi-functional and multi-robotic assisted platform for flexible non-invasive FUS therapy with the main aim to overcome current limitations of FUS procedure.

As described in the next Section (5.2), the possibility to manage two dedicated anthropomorphic manipulators (therapeutic manipulator with HIFU transducer + US confocal probe and monitoring manipulator with a 3D US probe) provided the FUTURA platform with a high flexibility in terms of workspace, thus allowing to choose suitable acoustic windows during all the phases of the procedure and to treat targets with high accuracy both in static and dynamic conditions.

5.2 A robotic system for HIFU surgery: the FUTURA platform

Despite the already demonstrated promising results (both from technological and clinical point of view) of HIFU technology that encourage further researches, it is clear that FUS suffers from important limitations, *i.e.* the limited flexibility in targeting and monitoring, which narrows the applicability mainly to non-essential and non-moving organs [9].

A robotic-assisted approach may offer the chance to overcome these limitations. As already demonstrated, robotic technology and computational devices are used to achieve pre-planning and navigation of surgical devices based on imaging data, leading to several advantages, including increasing task precision, accuracy, dexterity, and repeatability in positioning surgical tools and manoeuvring controlled trajectories [152]. In addition, robotic assistance to FUS, both with US or MR imaging modality, can intrinsically add precision to the entire procedure.

In the specific scenario of FUS, robotics may also represent the enabling technology for the treatment of different pathologies by US exploiting their intrinsic flexibility. To date, the improvement of the HIFU treatment accuracy by using different robotic solutions was investigated by several research groups: a single channel HIFU transducer coupled with a six-axis robot was presented in [153], where the HIFU system is intended to be deployed by an industrial robotic manipulator to allow precise targeting with a stable positioning. In parallel, a non-invasive US theragnostic system that compensates for movement by tracking and following the area to be treated by stereo US imaging, while irradiating the affected area with HIFU, was described in [154] and [155]. Finally, an all-in-one robotized HIFU system was developed by Chanel *et al.* in [156] for real-time intra-abdominal organ motion compensation by exploiting a US visual servoing scheme.

The goal of FUTURA project was to design, develop and assess an innovative robotic platform for FUS treatments. The expected contribution was to advance robustness, accuracy, precision and reliability of the therapy, as well as improving safety and acceptability of multifunctional robotic platforms in the surgical room [157].

One of the most important features of the FUTURA platform, as visible in the representation of Figure 5.4, is the use of two independent anthropomorphic manipulators that can be independently driven for maximizing the flexibility of the FUS procedure; this architecture allows to treat in principle different pathologies, relieving the problems related to the predictability and repeatability of the current procedures by enhancing accuracy, safety and flexibility of the treatment.

In addition, the FUTURA robotic integrated approach allows a safe interaction and cooperation between robots, patient and medical staff by using environmental reconstruction sensors. In fact the platform is expected to operate into a traditional surgical room, which appears as an unstructured and extremely critical environment; perception and cognitive capabilities are guaranteed by merging external sensors and embedded control strategies in a computer-assisted framework.

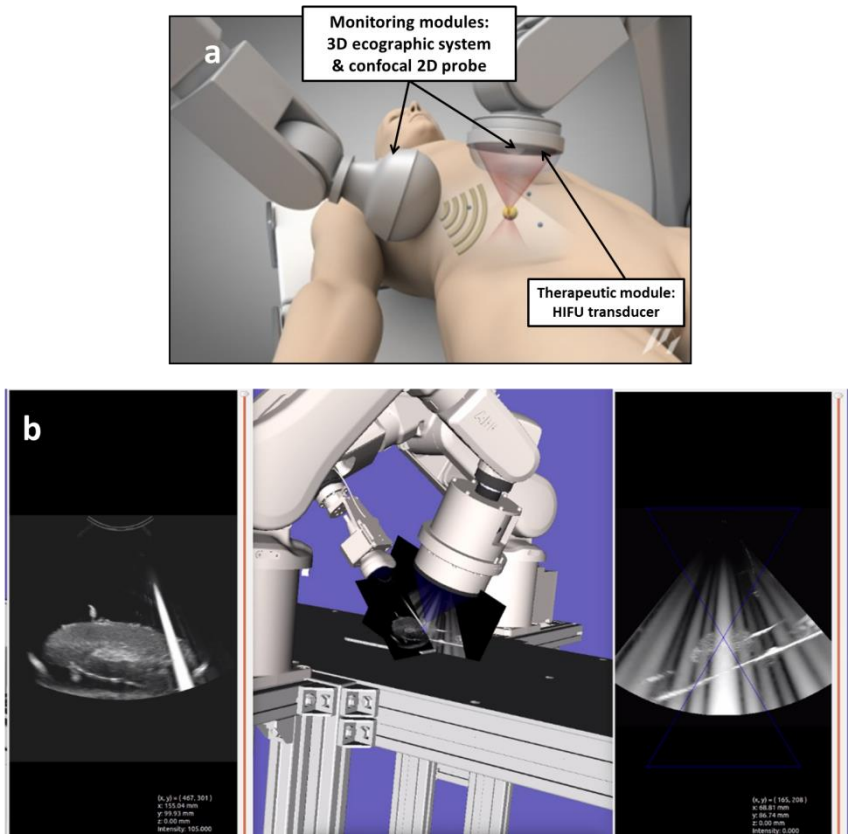

Figure 5.4. *a) General representation of the FUTURA platform; b) Real-time 3D visualization of the platform during sonication (middle) with B-mode images acquired simultaneously from the 2 US probes (left and right).*

5.2.1 Platform architecture and modules

The FUTURA platform with all the components integrated is shown in Figure 5.5.

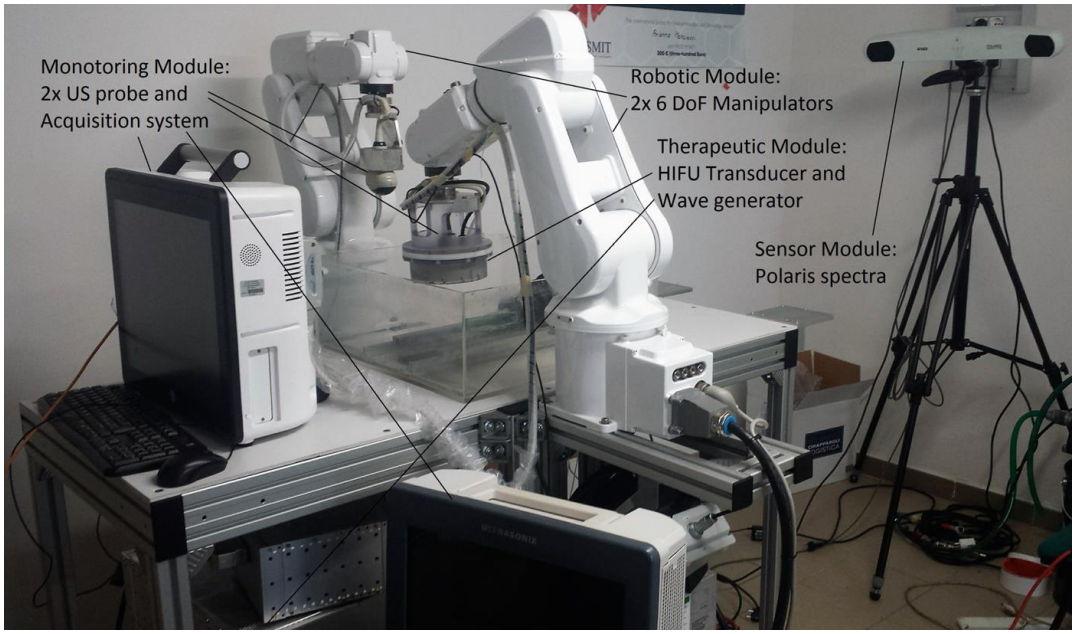

Figure 5.5. *FUTURA platform: robotic, monitoring, therapeutic and sensor modules.*

It consists in 4 different modules: robotic module, therapeutic module, monitoring module and sensor module.

1) ***Robotic module***: composed of two six degrees-of-freedom (DoFs) anthropomorphic manipulators - tracking and therapeutic manipulators - (*i.e.,* ABB IRB 120 - *www.abb.com*), with a payload of 3 Kg, repeatability of ± 0.01 mm and a control loop time in the order of 1 ms.

2) ***Therapeutic module*****:** composed of a dedicated and custom-made FUS system that consists of four main components:
   - a 16 channels high power signal generator (developed by Image Guided Therapy (IGT), *www.imageguidedtherapy.com*);
   - a 16 channels phased annular array transducer (Imasonic SAS, *www.imasonic.com*);

- a coupling system which provides an acoustic path between the FUS transducer and the patient and also cools the transducer for maintaining the patient skin at a physiological temperature;

The 16 channels annular array HIFU transducer (central frequency of 1.2 MHz) is driven by the 16 channels signal generator (20W of RF power per channel over a large frequency range (500kHz – 5MHz)). The phased array annular transducer allows to change the distance of the HIFU focus - along the axial axis - for the treatment of both superficial and deep seated tumours (electronic steering of ±40 mm). A flexible and acoustically transparent membrane (latex, 0.15 mm) attached to the HIFU transducer filled with degassed water maintained under proper pressure, was used as coupling system of the transducer with the patient's body (Figure 5.6). The pressure source is both dynamic, *i.e.* pump with adjustable flow rate, and static, *i.e.* an external water tank which can be raised or lowered in order to adjust finely the pressure on the membrane and hence the spacing between the transducer and the patient skin. Finally, a water circulation system, including an online degassing process to avoid cavitation in the proximity of the transducer, developed by IGT, was also included.

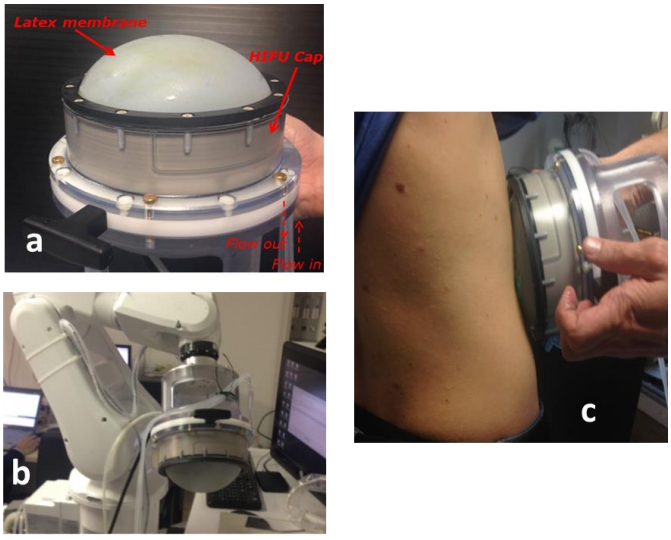

Figure 5.6. *Coupling system of FUTURA HIFU system. a) the specific interface (latex, 0.15 mm) filled with water, b) connection of the HIFU transducer to the robot, c) coupling of the HIFU transducer with the patient's body.*

Taking into account the intrinsic features of the transducer (electronic steering of ±40 mm, around the natural focus) and by exploiting the flexible membrane inflation and deflation process, as shown in Figure 5.7, the HIFU focusing range can varies from 10 to 130 mm, thus guaranteeing a correct therapy delivery in a range of distance compatible with the human anatomy.

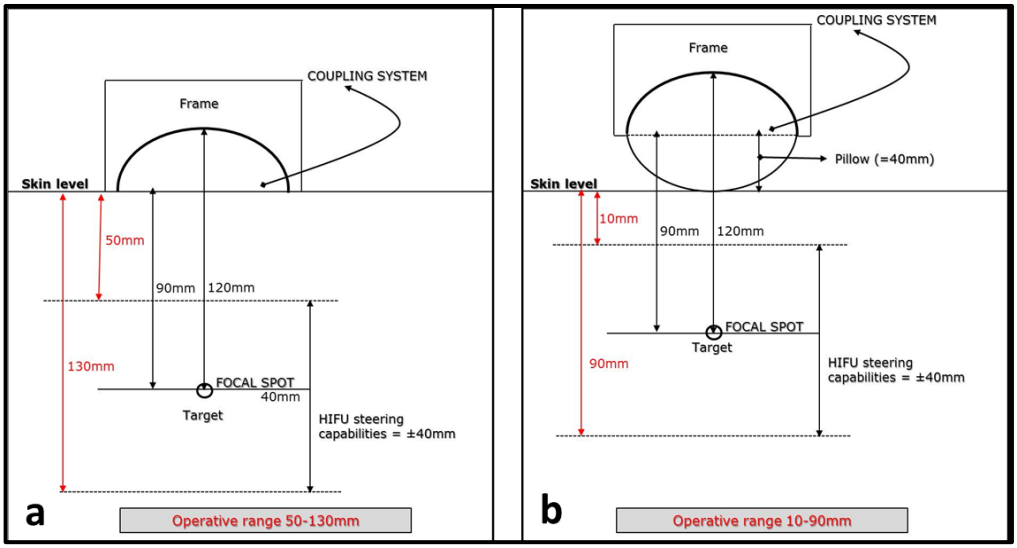

Figure 5.7. *Representation of the wide focusing range (10-130 mm) of FUTURA HIFU transducer in the two limit configurations a) minimum inflation of the coupling system, b) maximum inflation of the coupling system.*

3) ***Monitoring module***: composed of two different US probes. These are:

- a 2D imaging US probe (Analogic Ultrasound PA7-4/12) confocal to the HIFU transducer mounted on the therapeutic robotic manipulator,
- a 3D imaging US probe (Analogic Ultrasound 4DC7-3/40) mounted on the tracking manipulator;

Both probes are connected to two different Analogic Ultrasound SonixTablet machines (*www.bkultrasound.com/ultrasonix*) for continuous targeting of the organ and monitoring of the therapy.

4) ***Sensor module:*** consisting of proprioceptive (two ATI mini 45 force/torque sensors - *www.ati-ia.com* - fixed to the end-effectors of the robots) and exteroceptive (Microsoft Kinect depth space sensors and an NDI Hybrid Polaris Spectra optical tracking system - *www.ndigital.com* - placed in the working

environment) sensors for the implementation of dedicated control strategies. In particular, the two force/torque sensors are employed in the implemented hybrid force/position manipulator control. This control allows the FUTURA platform to: *i)* guide the manipulators by hand for finding suitable acoustic windows, and *ii)* maintain constant interacting forces/torques with the patient in different directions while the manipulator is moving. The Microsoft Kinect sensors are used for obstacle perception in the FUTURA environment and the Polaris Spectra is necessary in order to calibrate different platform modules.

Finally, a dedicated platform software, developed in Robot Operating System (ROS) system, allows the exchange of information and the synchronization among different modules.

5.2.2 Experimental procedure

The general workflow of the robotic-assisted FUS procedure is represented in Figure 5.8 (Top) and includes the following steps:

A. ***Pre-Treatment phase***: during this step, pre-operative images (*i.e.* MR or Computer Tomography images) are registered with the on-line US images, the target is identified and the therapy is planned;

B. ***Treatment phase***: HIFU therapy is delivered under US monitoring; for each single sonication a target point is selected, the HIFU transducer is switched on and the lesion progress is assessed using both the US probes, exploiting a pulsed signal for the transducer;

C. ***Post-Treatment phase***: after the last sonication, the treatment is finally evaluated using both US images probes.

The assessment of the overall workflow of the procedure is discussed in Section 5.4.

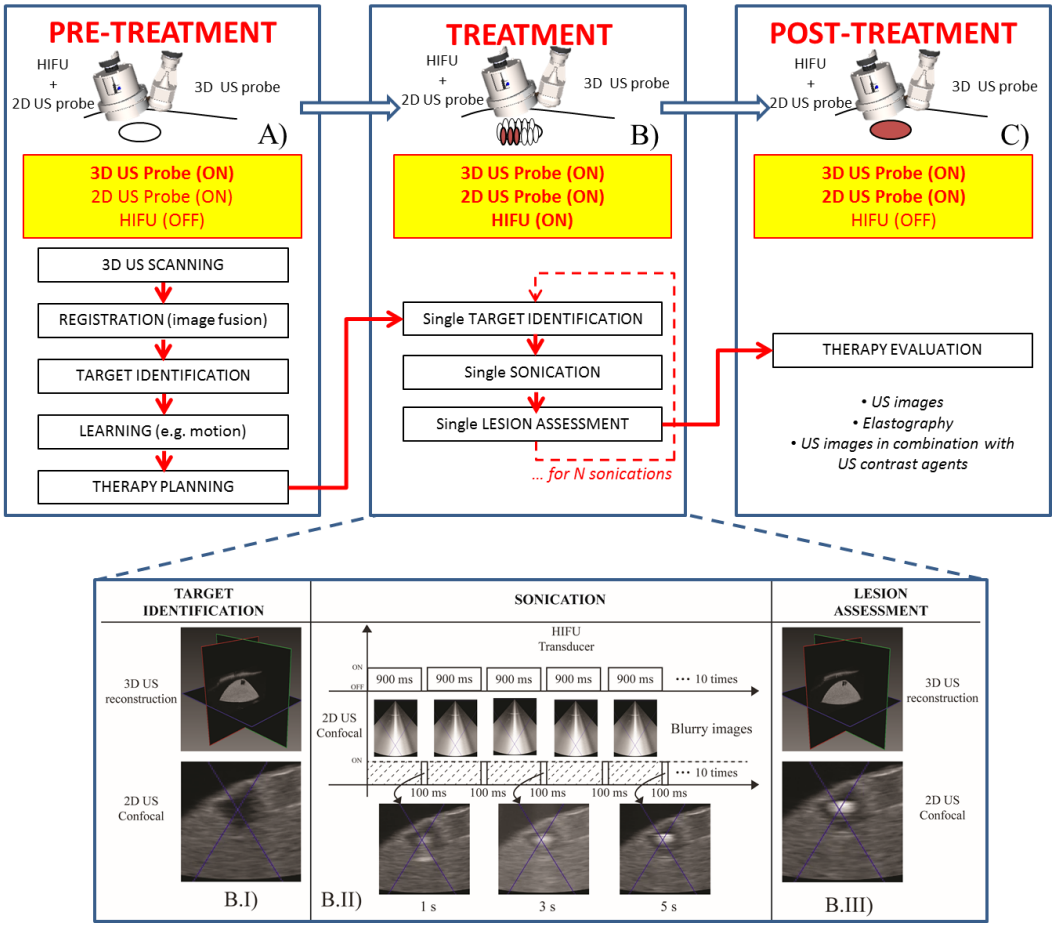

Figure 5.8. *Workflow of the robotic-assisted FUS procedure (Top) that includes: A) Pre-Treatment; B) Treatment and C) Post-Treatment phases. Each single sonication can be divided in three further stages: B_I): Target identification phase: both US probes are used to identify the point to be sonicated; B_II) Sonication phase: the HIFU is switched on and the lesion progress is assessed through US confocal probe; B_III) Lesion assessment phase: the created lesion is assessed with both US imaging probes.*

5.3 HIFU transducer characterization

Before fixing the HIFU to the end effector of the therapeutic robot, the transducer was characterized in free field conditions. In particular, two different experiments were conducted: the geometric characterization of the HIFU focus (Section 5.3.1) and the assessment of the confocality between the HIFU transducer and the PA7-4/12 US imaging probe (Section 5.3.2).

5.3.1 HIFU field characterization

In order to understand the geometric properties of the 16 channels annular array HIFU beam (*e.g.*, typical dimensions of the focus, distance between active surface and focus,

etc.) the acoustic field generated by the US transducer was characterized in free field conditions.

The procedure used was the same as that described in Section 4.2.2, with only the following differences:

- the 16 channels custom phased array signal generator developed by IGT was used to drive the HIFU generator;
- a PicoScope 3204D (Pico Technology) was used to acquire the signal from the hydrophone;
- a user-friendly Graphical User Interface (GUI) developed in Python was used to manage the overall procedure in order to control the gantry, the wave generator and the oscilloscope in an automatic mode;

The results of the characterization of the HIFU transducer generated field are reported in Figure 5.9.

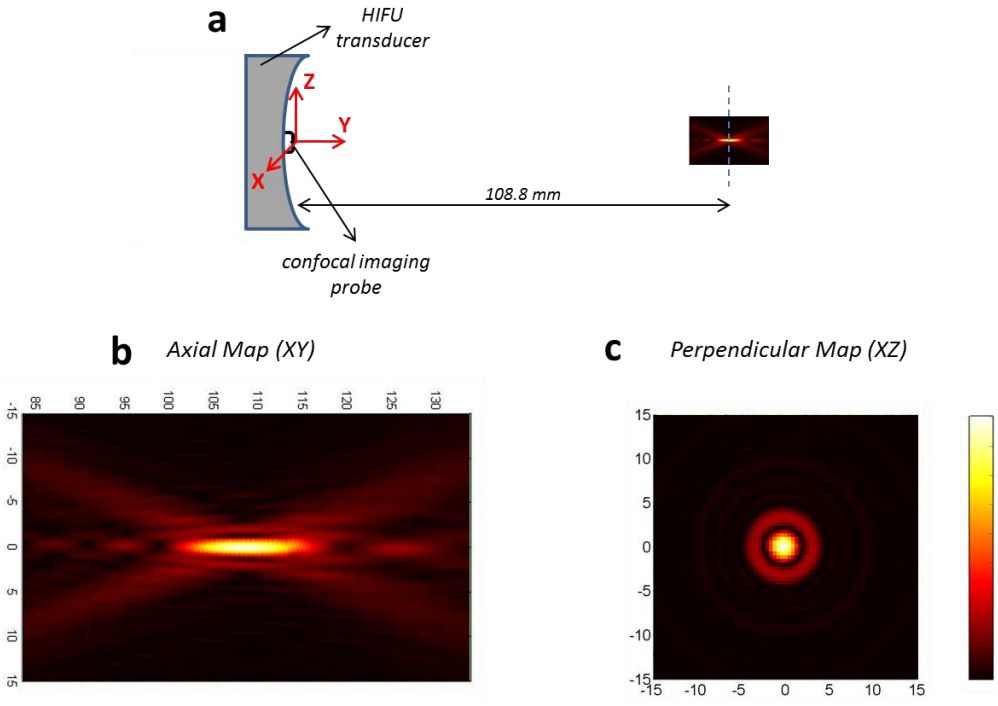

Figure 5.9. *Field characterization of the HIFU transducer @1.2 MHz; a) Visualization of the focus with respect to HIFU transducer; b) pressure map in the axial plane of the HIFU transducer; c) pressure map in the perpendicular plane of the HIFU transducer, at the focus. The origin of the reference system is located on the US probe.*

The geometrical properties of the focus are reported in Table 5.2. The 3 dB focal area of the HIFU transducer used in this work has a diameter of 1.5 mm and a focal length of 10.0 mm (typical cigar shape).

Property	Value
Focal length (3dB) [mm]	10.0
Focal diameter (3dB) [mm]	1.5
Focal area (3dB) [mm^2]	7.1
Focal volume (3dB) [mm^3]	94.2

Table 5.2. *Geometrical features of the HIFU transducer @1.2 MHz.*

5.3.2 Verification of the confocal configuration of the 2D US probe

The confocality between the HIFU transducer and the 2D PA7-4/12 US imaging probe was also verified. The goal of this experiment was in fact to verify the mutual positioning of HIFU and confocal 2D US probe. With this aim, the following steps were followed (the coordinates system is the same shown in Figure 5.9-a).

1. ***Focus finding* and *symmetry verification:*** The position of the HIFU focus (point of maximum pressure) was found through 1D scans of the hydrophone in three directions (X-Y-Z), by performing the procedure as described in detail in Section 4.2.2;

2. ***Hydrophone tip verification from US images:*** An US-image (X-Y plane) is acquired with the tip of the hydrophone positioned in the HIFU focus. As shown qualitatively in Figure 5.10, the tip of the hydrophone is visible in the middle of the image as a hyperechoic spot;

3. ***Verification of the confocal configuration of the US probe:*** The hydrophone was moved in X and Z axes (radial axes with respect to the HIFU transducer) both in positive and negative directions until the hydrophone tip was no more detectable in the US images. The hypothesis was that a correct alignment of the US probe with respect to the HIFU transducer should result in total symmetry in both X and Z directions.

4. ***Error estimation:*** A misalignment of 0.5 mm (X direction) and 1 mm (Z direction) was measured at the focus distance (Y=108.8 mm). As a result, the tilt angles of the US probe were 0.26° in X axis and 0.53° in Z axis.

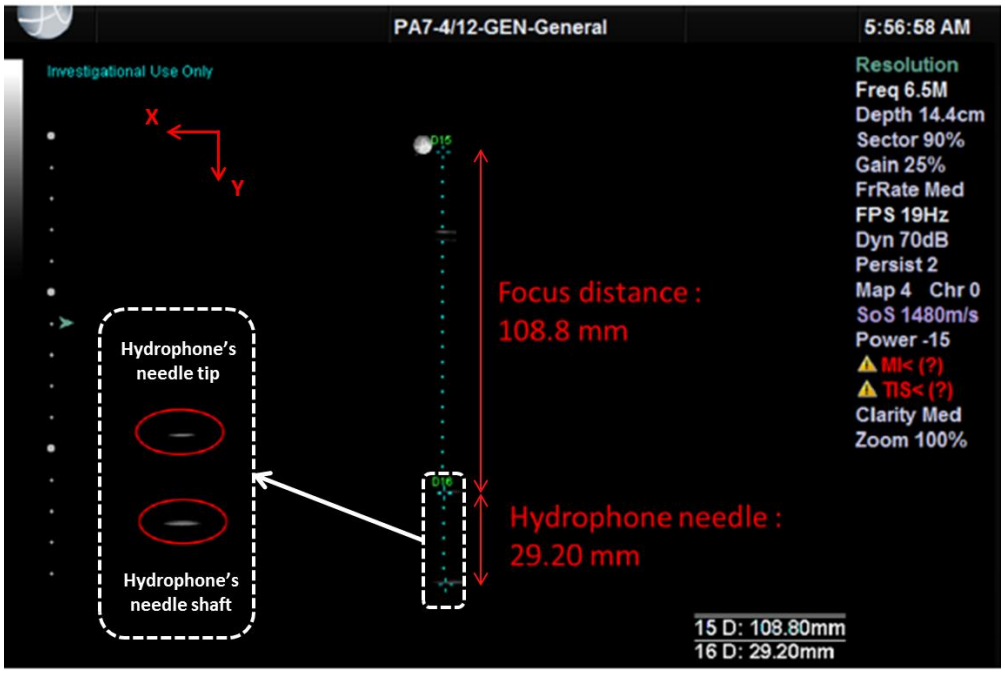

Figure 5.10. *B-Mode image of the needle hydrophone positioned in the HIFU focus.*

As a consequence of this calibration, a small misalignment of the US confocal probe with respect to the HIFU transducer was measured (*i.e.* 1 mm and 0.5 mm in the two radial directions at the focus distance). Considering the dimensions of the HIFU focus reported in Table 5.2 (cigar shape with typical dimension of 1.5 mm and 10 mm), this asymmetry can be considered negligible for a correct targeting and monitoring.

However, for the optimization of other imaging modalities, such as Acoustic Radiation Force Imaging (ARFI) [158], this misalignment should be considered. For this reason, a more precise mechanical repositioning of the confocal US probe inside the HIFU transducer will be considered next.

5.4 Assessment of HIFU procedure

The assessment of the HIFU procedure and the demonstration of therapy monitoring with 2 different US probes was firstly performed in *in vitro* static conditions (Section 5.4.1), thus a study of the HIFU lesion volume as a function of sonication time and acoustic power was accomplished in *ex vivo* static conditions (Section 5.4.2) and finally the performances of the system in terms of treatment precision were evaluated for moving targets (Section 5.4.3).

5.4.1 *In vitro* tests in static conditions

The FUS procedure was conducted by using an in-house developed phantom, made up by a bulk of agar gel with internal cylinders (representing the targets of the therapy), based on polyacrylamide gel (PAA) mixed with egg white [54]. This material is a good mimicking phantom for HIFU ablation because it turns opaque only in proximity of the HIFU focus and the formed lesion is clearly visible especially in US B-mode images [53] (Figure 5.11). The phantom was immersed in a tank with degassed water ensuring a correct acoustic coupling for the two US imaging probes and HIFU transducer.

The first phase of the FUS procedure entails the identification of the target through the US probes (Figure 5.8-B.I). A 3D US phantom reconstruction is performed; thus, by selecting the centre of the target to be sonicated (using the HMI integrated software), the therapeutic manipulator adjusts its position for performing the desired spot sonication. The images provided by the confocal 2D US probe guarantee the correctness in manipulator position (the visualized blue cone in all the 2D US images indicates the HIFU focus position). After checking the therapeutic manipulator positioning, a sonication composed by 10 repetitions of 1 second with 90% duty cycle is set. Frequency and acoustic power of the sonication are 1200 kHz and 120 Watts, respectively. During the sonication procedure the confocal 2D US probe is active for monitoring the lesion progress when the HIFU is switched off (10% of the time) (Figure 5.8-B.II). Finally the last phase of the FUS procedure is the lesion assessment performed through both the US imaging probes (Figure 5.8-B.III).

Even if changes in echogenicity in B-mode images cannot be used as an indicator of a irreversible HIFU-induced tissue damage, they can provide a real-time feedback on the position and extent of the expected lesion [159].

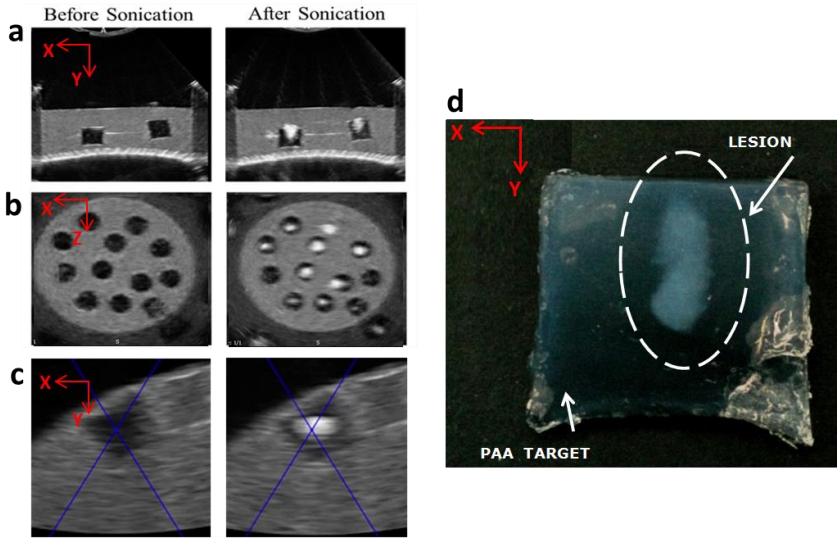

Figure 5.11. *Evaluation of target accuracy on phantom. Transversal planes (a) and frontal planes (b) extracted from the volume acquired by the 3D US probe, before (left) and after (right) sonications. The tissue-mimicking phantom is composed by two different materials, clearly distinguishable in the US B-mode images: the bulk of the structure is made up by agar gel, while the internal darker cylinders, that represent the targets of the therapy, are based on polyacrylamide gel (PAA) mixed with egg white. The spatial information of the centre of each target is used for positioning the HIFU transducer, so that the HIFU focus is coincident with the centre (as visible in (c)): blue lines represent the virtual HIFU beam and their intersection identifies the HIFU focus that is positioned exactly in the centre of the target. All generated lesions are clearly detected as hyperechoic areas (white spots in the figure) in US images. In (d) an optical image of the lesion induced by the HIFU transducer into the tissue-mimicking phantom is also represented.*

The procedure was performed on 11 different targets of the same dimensions (15 mm diameter and 15 mm height). As shown in Figure 5.11 after sonication the HIFU lesion is clearly visible in US images and can be easily detected. The lesion has the characteristic axial-symmetric "egg" shape, which is the typical shape created by acoustic cavitation activity. In the axial direction, a small mismatch between the positions of the US visualized lesion and the theoretical position of the centre of the HIFU focus was sometimes observed. This is caused by the fact that the cavitational effects are clearly visible by US images few mm above the center of the focal region; evidences of this phenomenon are reported in [53]. The position errors between the calculated location of each target ($x_t;y_t;z_t$) and the effective CoM of the corresponding lesion ($x_l;y_l;z_l$) are evaluated by means of an Euclidean distance in each single direction in the US images that represent the only feedback during FUS treatments.

Targeting error resulted to 0.66 ± 0.19 mm and 0.66 ± 0.34 mm in radial directions with respect to the HIFU transducer's active surface and 3.67 ± 1.51 mm in the axial direction.

Direct measurements on the sectioned targets in proximity of the lesion was also performed for additional assessment. Results of the calculated centre of the mass with respect to the centre of the target and dimensions (lesion's shape is approximated to an ellipsoid) are reported in mm in).

	$\lvert x_l - x_t \rvert$	$\lvert z_l - z_t \rvert$	$\lvert y_l - y_t \rvert$	Diameter	Length
US	0.66±0.19	0.66±0.34	3.67±1.51	8.13±1.95	9.17±1.73
DIRECT	*	*	4.0±1.2	2.9±0.3	5.5±1.1

Table 5.3. *Error estimation and lesion dimension evaluation.*

5.4.2 *Ex vivo* tests in static consitions

Characterization of HIFU devices using *ex vivo* tissues is an important step of the preclinical testing for new HIFU systems [160]. The size of the induced HIFU lesion and its dependence on the sonication parameters can be easily evaluated in excised animal organs by cutting and visually inspecting the samples after the sonication in proximity of the lesion. As visible in Figure 5.12, lesions are clearly recognizable.

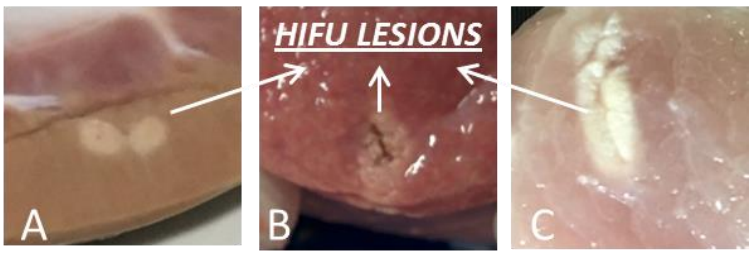

Figure 5.12. *Optical images of the lesion induced by the HIFU into ex vivo tissues: porcine kidney (A), porcine liver (B) and breast chicken (C).*

In this work, the change in the lesion size as a function of sonication time and sonication power was evaluated using *ex vivo* breast chicken tissue. The aim was to understand how these parameters affect the geometry of the lesion. The chosen tissue to be treated with the HIFU therapy was chicken breast, because of its wide availability and its known acoustic properties, which is in the same order as human muscle tissue. The used experimental set-up is shown in Figure 5.13. In order to avoid secondary

thermal effects at the bottom surface of the tissue, a hydrogelic layer (3% gelatin - 3% agar) was interposed between the tissue and the acoustic absorber. 35 different sonication conditions were tested varying the sonication time (1, 5, 10, 15 and 20 s) and the sonication power (10%, 20%, 30%, 40%, 50%, 60%, 70% of the maximum electric power - 320 Watt -, corresponding to 32, 64, 96, 128, 160, 192, 224 Watt). At least 4 lesions for each sonication condition were induced.

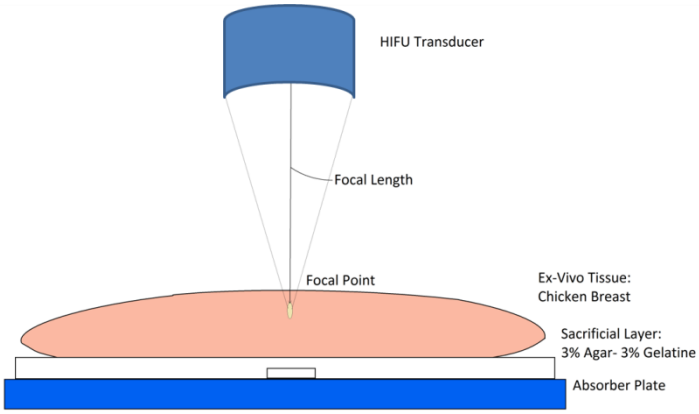

Figure 5.13. *Schematic representation of the experimental set-up used for ex vivo sonication tests.*

The procedure of extracting the lesion was performed manually using a scalpel. To indicate the position of the lesion, the tissue was marked at the surface with a small cavitation induced hole, directly above the lesion, using 5 executions (pulse repetition frequency of 1 Hz) with a duration of 200 ms at high power (80%).

The lesion volume (*V*) was derived from the lesion length and width measurement, assuming an ellipsoid shape. The formula for the calculation of ellipsoid volume is as followed:

$$V = \frac{4}{3}\pi\, l\, w^2 \qquad \text{Eq. 5.1}$$

where *l* represent the length *w* the width of the lesion. Results are reported in Figure 5.14.

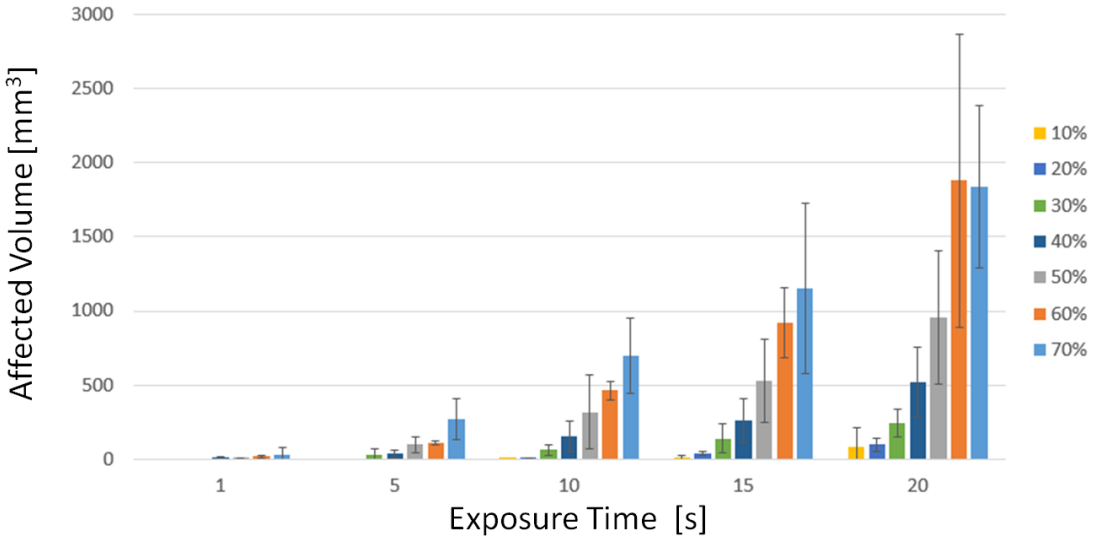

Figure 5.14. *Influence of exposure time and power on the final ablated volume in chicken breast. Electrical powers are expressed in percent of the maximum power (320 Watt).*

As visible in Figure 5.14, both sonication duration and sonication power influence the final volume of the lesion directly.

Furthermore, it is worth mentioning that, in addition to these two parameters, duty cycle can also strongly influence both the lesion size and the type of lesion (*i.e.* thermal or cavitation damage).

Starting from these preliminary results, in future it is planned to cover a broader range of sonication conditions in order to finely tune and control the type and the dimension of the lesion. In order to discriminate between thermal and non thermal effects fine wire thermocouples for temperature measurements and a passive cavitation detector for cavitation monitoring will be also integrated in the system.

5.4.3 *Ex vivo* tests in dynamic conditions

As highlighted in Section 5.1, one of the main limitation of current clinical HIFU systems is that they are not able to compensate for organs' motion during sonication. Nowadays, pathologies in moving organs (*e.g.* liver, kidney etc) are treated with HIFU in combination with motion-suppression methods, such as apnea or sustained ventilation [161]. However, continuous ablation strategies (*i.e.* motion tracking) are preferable for reducing the overall treatment duration and for avoiding sophisticated respiratory gating methods. Motion tracking has never been tested in a clinical trial;

however, many preclinical studies were published using both US and MR for motion monitoring.

Chanel et al. [162] developed an all-in-one robotized FUS system for real-time intra-abdominal organ motion compensation by exploiting a US visual servoing scheme. Seo *et al.* in [155] developed a visual US based servoing system for ablating moving medical target. Exploiting a sophisticated timeline schedule, the authors were able to interlace two US sources thus achieving a motion compensation accuracy of 1.7 mm (RMS) on average with a sonication duty cycle of 50%.

The experimental set-up used to assess the performance of the FUTURA platform under dynamic conditions, is shown in Figure 5.15. To simulate the organ motion, an *ex-vivo* porcine kidney was placed on a motorized slide; for replicating respiratory motion, a sine function with amplitude 200 mm and frequency 0.2 Hz - 12 breaths per minute - was set.

Machine learning and computer vision techniques were used for treating moving targets. More precisely, the strategy is based on a combination of three different modules: i) a tracking and detection module; ii) a trajectory prediction module; and iii) a safety check module.

The tracking and detection module estimates the motion of a Region of Interest (ROI) selected by the users through the HMI. This module is based on the approach named Tracking-Learning-Detection (TLD) described in [163], which decomposes the long-term tracking task into tracking, detection, and learning. The tracker follows the selected ROI in the US image stream using optical flow. The detector localizes similar patches in the image via a template matching approach using the Normalized Correlation Coefficient (NCC) as the main similarity measure. The learning task combines the tracker and the detector information in order to: i) correct and re-initialize the tracker when the detector is more confident, and ii) update the internal model of the detector when the tracker is more confident.

The trajectory prediction module learns the trajectory estimated by the tracking and detection module, and it drives the therapeutic manipulator during HIFU sonication even when the US images are completely distorted. Namely, the prediction module

learns the organ motion using a Gaussian process model with a periodic kernel (solving a unidimensional regression problem). When the organ motion is learned, the therapeutic manipulator starts to follow the predicted motion of the currently tracked area. Before shooting, the safety check module computes the distance between the current target position in the US image and its predicted position, thus allowing to sonicate only if this distance is smaller than a settable threshold (*e.g.*, 1 mm).

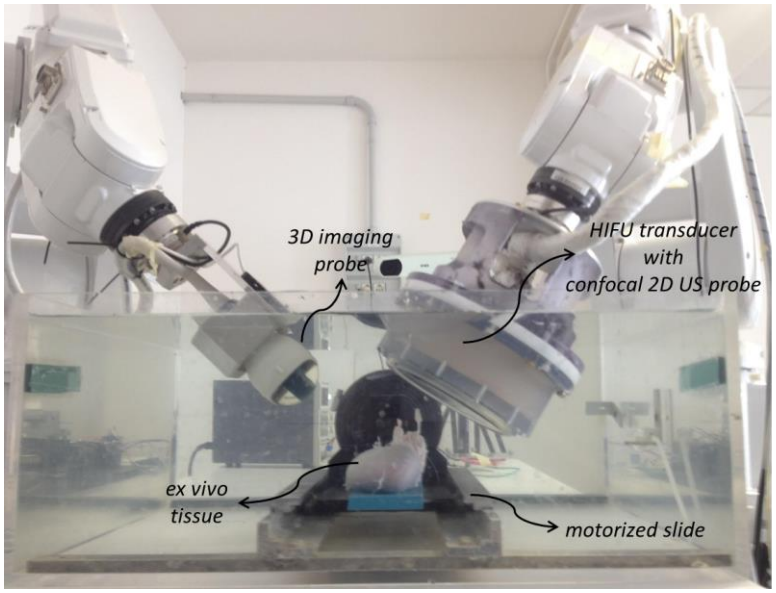

Figure 5.15. *Experimental set-up used for the therapy assessment in dynamic conditions. An ex-vivo porcine kidney is placed on a 1 DoF motorized slide for simulating the organ motion.*

Therefore, if a deviation is detected between the tracked trajectory and the learned trajectory, the HIFU sonication is disabled until the new target trajectory is learned or the target point again starts following the estimated trajectory.

Two different robotic tracking strategies were investigated:

- ***Linear Tracking.*** The linear tracking is performed moving the robot in linear motion (Figure 5.16). This is the simplest way to compensate the motion of the target point, however this approach could limit the range of imaging and treatment for the tracking of moving organs; the continuous modification of the acoustic window doesn't always allow to target/treat the target (*e.g.* presence of the ribs in the path of the HIFU beam) in an *in vivo* scenario [155]. Moreover, a tank completely filled with water is required.

It is worth mentioning that some phased array HIFU transducers can steer the focus in a certain region around the natural focus not only in the axial direction, but also in radial directions, enabling the target of moving objects also maintaining the HIFU fixed [164]; however with this configuration the complexity, and the price, of the system increases a lot due to the large number of active elements (more than 200) required [165].

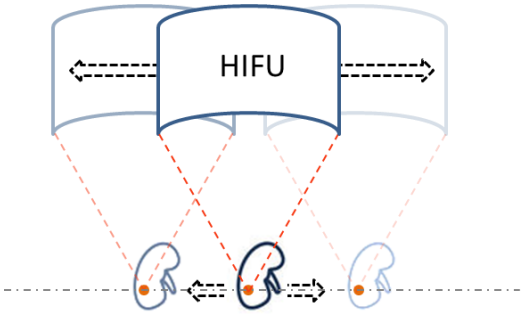

Figure 5.16. *Schematic representation of the linear tracking approach for treating moving targets.*

- ***Angular Tracking.*** Thinking about clinical applications in which the HIFU transducer is positioned in contact with the patient skin through an acoustic coupling system (*e.g.* pillow filled with degassed water), the linear tracking approach could present some problems; friction and rubbing between the membrane of the pillow and the skin can cause a loss of acoustic coupling and the continuous changing of the contact point and the resulting plane of imaging and therapy can cause the loss of the good acoustic path between the transducer and the target.

  Conversely, by means of an angular tracking approach, the HIFU transducer motion is performed only adjusting the orientation of the manipulator and maintaining the same contact point between the transducer and the patient's skin (*i.e.* pivot movement, Figure 5.17-a). During all the phases of the target motion, the versor between the end effector and the target area is computed and the desired manipulator orientation is provided to the manipulator controller.

However, maintaining a fixed pivot point, the axial distance between the HIFU and the target point continuously changes. In this respect, exploiting the electronically steering capabilities of the annular array HIFU transducer, it is possible to adjust the focal depth at a very fast rate (frame rate of 20 Hz). This results in the possibility of targeting any desired moving point in the 3D space by only using 3 angular movements and the electronic steering in the axial axis.

With the aim to test the accuracy of the angular tracking, the set-up shown in , Figure 5.17-b was used. An acoustically transparent membrane (polyester, 20 µm) was used to simulate the contact between the coupling system of the HIFU transducer (latex membrane filled with degassed water) and the patient's skin.

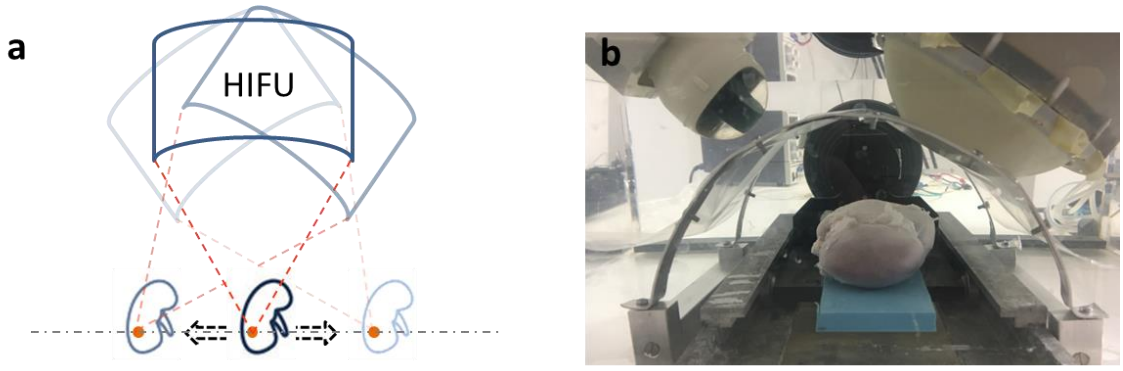

Figure 5.17. *Schematic representation of angular tracking approach for treating moving targets. b) Picture of the experimental set-up used for angular tracking tests.*

The error between the real target point position and the nominal HIFU focal spot was evaluated both with the linear and the angular tracking approach. The position of the HIFU focal spot was computed using the direct kinematics of the manipulator (based on encoder measurement) and exploiting the estimated rigid transformation between the manipulator flange and the origin of the HIFU transducer.

In order to evaluate the tracking accuracy, the following steps were followed. The target area was set on the US image provided by the 3D probe mounted on the monitoring manipulator. Then, the therapeutic robot was activated following the learned trajectory without activating the HIFU. The procedure was performed 10 times on different kidney target areas both for the linear and the angular approach; the data were recorded to evaluate the vector error between the target and the nominal HIFU focal spot.

Figure 5.18 illustrates the results of the tracking experiments.

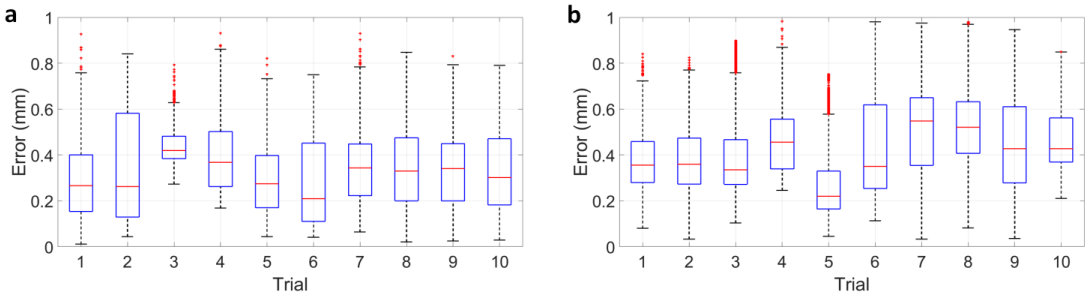

Figure 5.18. *Boxplot of the error between the real target point position and the nominal HIFU focal spot for linear tracking (a) and angular tracking (b) experiments on 10 different targets.*

The box and whiskers plot shows that the motion compensation error norm is always lower than 1 mm both exploiting the linear and the angular approach. The achieved accuracy is less than the accuracy reported in Seo *at al.* [155].

Finally, three thermal lesions were obtained on chicken breast (Figure 5.19) using the same acoustic parameters (15 s, 115 Watt, f=1.2 MHz, CW). The first one (Figure 5.19-a) was obtained in static condition with the motor of the slide turned off, while the second one (Figure 5.19-b) and the third one (Figure 5.19-c) were obtained in dynamic conditions, by means of linear tracking and angular tracking respectively.

As clearly visible in Figure 5.19, the three lesions appear very similar in size and geometry, thus qualitatively confirming the high accuracy of the implemented tracking strategies.

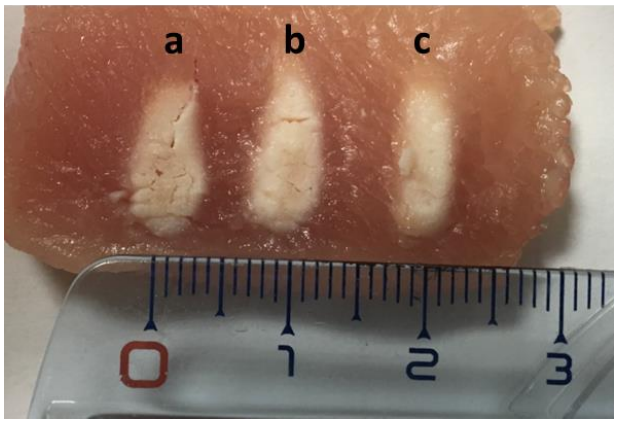

Figure 5.19. *Lesions on chicken breast performed in: a) static condition, b) dynamic conditions with a linear tracking and c) dynamic conditions with an angular tracking. The lesions were purposely induced at 10 mm distance from each other.*

Scientific production (Chapter5)

Publications on Internationals journals

- S. Tognarelli, G. Ciuti, A. Diodato, **A. Cafarelli**, A. Menciassi. "Robotic Platform for High-Intensity Focused Ultrasound Surgery under Ultrasound Tracking: the FUTURA Platform". *Journal of Medical Robotic Research. 2017.* DOI: 10.1142/S2424905X17400104

Papers presented at International conferences

- **A. Cafarelli**, A. Diodato, S. Tognarelli, M. Mura, G. Ciuti, A. Menciassi, "The FUTURA robotic platform for USgFUS". 28th Conference of the international Society for Medical Innovation and Technology (SMIT). Delft, October, 2016.

- A. Diodato, **A. Cafarelli,** A. Schiappacasse, L.A. Chanel, S. Tognarelli, G. Ciuti, A. Menciassi, "Computer-assisted robotic platform for USgFUS treatment". 6th Joint Workshop on New Technologies for Computer Assisted Surgery (CRAS). Pisa, September, 2016;

- A. Menciassi, S. Tognarelli, **A. Cafarelli**, A. Diodato, G. Ciuti, "Multifunctional robotic platform for USgFUS". 5th International Symposium on Focused Ultrasound. Washington, August, 2016;

- **A. Cafarelli**, A. Diodato, A. Schiappacasse, S. Tognarelli, G. Ciuti, A. Menciassi, "Robotic platform for Focused Ultrasound Surgery". 6th Congresso Gruppo Nazionale di Bioingegneria (GNB). Napoli, June, 2016 (*as speaker*);

- **A. Cafarelli**, A. Diodato, M. Mura, S. Tognarelli, L. Ricotti, G. Ciuti, A. Menciassi, “A tissue-mimicking phantom for in-vitro accuracy evaluation of USgHIFU procedures”. 3rd European Symposium on Focused Ultrasound Therapy. London, October, 2015; (*as speaker*). AWARDED AS BEST ORAL PRESENTATION.

- S. Tognarelli, G. Ciuti, A. Diodato, **A. Cafarelli**, M. Mura & A. Menciassi. "Robotic platform for high-intensity focused ultrasound surgery under ultrasound monitoring and guidance: the FUTURA platform". 5th Joint Workshop on New Technologies for Computer Assisted Surgery (CRAS). Brussels, September, 2015;

- **A. Cafarelli**, M. Mura, A. Diodato, A. Schiappacasse, M. Santoro, G. Ciuti, A. Menciassi. " A computer-assisted robotic platform for Focused Ultrasound Surgery: assessment of high intensity focused ultrasound delivery “. 37th

Annual International Conference of the IEEE Engineering in Medicine and Biology Society (EMBC). Milan, August, 2015;

- S. Tognarelli, G. Ciuti, A. Diodato, P. Miloro, A. Verbeni, **A. Cafarelli**, & A. Menciassi. "FUTURA: a computer-assisted robotic platform for high-intensity focused ultrasound". 4th Joint Workshop on New Technologies for Computer Assisted Surgery (CRAS). Genova, October, 2014;

- A.Verbeni, G. Ciuti, **A. Cafarelli**, P. Miloro, A. Diodato, S. Tognarelli, & A. Menciassi. "The FUTURA platform: a new approach merging non-invasive ultrasound therapy with surgical robotics". 36th Annual International Conference of the IEEE Engineering in Medicine and Biology Society (EMBC). Chicago, August, 2014;

Papers submitted to International conferences

- A. Diodato, A. Schiappacasse, **A. Cafarelli**, S. Tognarelli, G. Ciuti and A. Menciassi. "Robotic-assisted platform for USgFUS treatment of moving organs". 10th Hamlyn Symposium on Medical Robotics. London, 25-28 June 2017.

6 Focused Ultrasound-induced Blood Brain Barrier opening

FUS in combination with intravenous injection of microbubbles (MB) has been recently demonstrated to be capable of non-invasively, transiently and locally increasing Blood Brain Barrier (BBB) permeability [166], thus allowing a targeted delivery of therapeutic agents in the brain.

The feasibility of FUS-induced BBB opening was unequivocally proven in several animal models, including non-human primates. In November 2015, at Sunnybrook Health Sciences Centre in Toronto, BBB opening by FUS was achieved for the first time on humans, thus enabling an effective delivery of chemotherapy into a patient's malignant brain tumor [167].

However, a critical evaluation of the side effects associated with this procedure is still an open issue, although it is crucial towards a clinical application of this technology [168].

Real-time passive cavitation detection of MB activity could be a reliable monitoring parameter for an effective and safe FUS-induced BBB opening.

In this Chapter, after briefly exploring the state of the art of FUS-induced BBB opening and the methods for detecting acoustic cavitation (Section 6.1), a procedure for safe and effective transient BBB permeabilization based on passive cavitation on rats is presented in Section 6.2. Preliminary results are reported (Section 6.3) demonstrating that a real time passive cavitation control during FUS-induced BBB opening can ensure an effective and safe process.

The work described in this Chapter was carried out during a six months experience in the laboratories of NeuroSpin, Commissariat à l'énergie atomique et aux énergies alternatives (CEA), Gif-sur-Yvette, France, in the Molecular Imaging and Delivery of Active Substances team headed by Sébastien Mériaux and Benoît Larrat (*http://i2bm.cea.fr/drf/i2bm/english/Pages/NeuroSpin/UNIRS/MIDAS.aspx*).

6.1 FUS-induced BBB opening: background

The Blood Brain Barrier (BBB) is a specialized barrier system, lining the cerebral vessels, formed by endothelial cells connected together by tight junction proteins and surrounded by extracellular matrix, astrocytes, pericytes, vascular smooth muscle cells and microglial cells (Figure 6.1) [169].

Compared with the capillaries featuring the other organs, the peculiar structure of the BBB considerably limits the intercellular translaminar flow to very small weight, uncharged, and lipid soluble molecules.

This represents a natural defense for the brain in protecting neural tissues from harmful substances circulating in the bloodstream: only small uncharged molecules (<400 Da) and few others molecules, such as glucose and amino acids, indeed, can cross the BBB by means of a passive and active transport mechanism, respectively [170]. However, the BBB is also a serious impediment to the use of pharmaceutical treatments for brain pathologies: only about the 2% of available drugs can be delivered in the brain from the circulatory system.

Bypassing the BBB for an effective, safe, reversible and localized drug delivery in the brain is a significant challenge in medicine, that may have a huge impact in the treatment of several brain pathologies such as brain cancer (*e.g.* gliomas) or neurodegenerative diseases (Alzheimer's, Parkinson's, multiple sclerosis, amyotrophic lateral sclerosis and other ones).

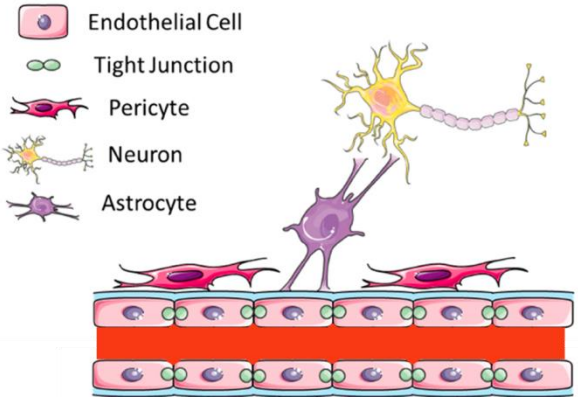

Figure 6.1. *Depiction of the BBB structure and its main components: endothelial cells, tight junctions, perycites, neurons and astrocytes. [171]*

Rather than designing new therapeutic molecules (drugs) sufficiently small to pass through the BBB, in recent years great efforts have been made in the study and testing of new noninvasive image-guided strategies for a transient and localized BBB disruption [172].

Figure 6.2 shows different brain targeted drug delivery approaches currently used in the clinics or currently under investigation in clinical trials, such as FUS used in combination with an intravenous injection of MB (Figure 6.2-a), nanoparticles activation using magnetic fields to induce targeted hyperthermia (Figure 6.2-b), transmembrane voltage induced by electric field (Figure 6.2-c), targeted laser therapy (Figure 6.2-d), and radiation therapy (Figure 6.2-e).

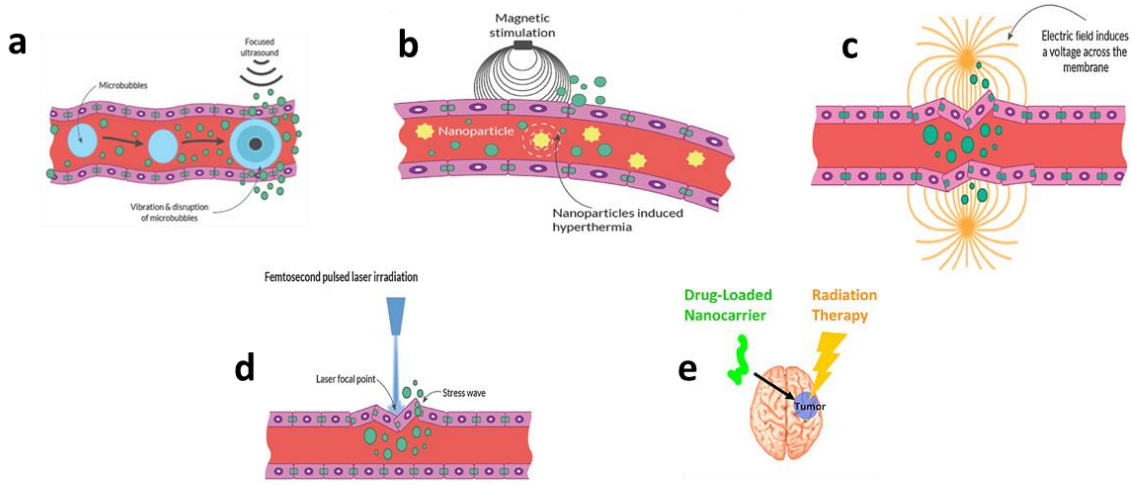

Figure 6.2. *Schematic depiction of different stereotactic solutions to enhance permeability of Blood Brain Barrier; a) FUS stimulation in combination with intravenously injected MB; b) nanoparticles activation using magnetic field; c) electric field stimulation across the membrane; d) laser stimulation; e) X-ray and proton therapy radiation. Figure readapted from Appelboom et al. [172].*

Among the above-mentioned strategies to efficiently and safely enhance the BBB permeability, the most investigated and promising technique implies the use of FUS.

FUS in combination with US contrast agents (*e.g.* MB) for BBB opening is a new emerging non-invasive technique for enhanced delivery of therapeutic agents in the brain via local, safe, and reversible BBB disruption.

McDannold *et al* [173] demonstrated US-mediated BBB opening relying on hyperthermia phenomena; the opening was however always accompanied by hemorrhages and tissue damages, making this approach unsafe.

In 2001 Hynynen [166] demonstrated for the first time that FUS in combination with MB can locally disrupt the BBB. After this pioneering work, several studies on different animal models were published, with the aim to establish the optimal acoustic parameters enabling to reversibly and locally open the BBB while avoiding induced thermal effects [174-178].

MB are US contrast agents commonly used for diagnostic procedures; they are typically larger than 1 μm, they have imaging duration up to 10 minutes and they are typically injected intravenously (IV). At present, three commercial MB agents are licensed for clinical diagnostic applications: SonoVue (Bracco, Milano, Italy), Optison (GE Healthcare, WI, USA) and Definity (Lantheus Medical Imaging, MA, USA) [179].

The use of MB reduces the total amount of energy required to open the BBB, consequently reducing the risk of skull heating and hemorrhages in the brain.

The employment of FUS in combination with MB implies significant advantages in BBB opening [180]. The following features are endowed by this approach:

- ***Targeting.*** The US beam is focused; only a small area of interest (few mm as typical dimensions) is targeted. The use of a multi-element phased array transducer (*e.g.* ExAblate Neuro, Insightec) allows also to electronically steer the focus in different areas of the brain without moving the transducer itself.

- ***Transiency***. If FUS is applied within an appropriate acoustic range, the BBB opening is reversible. Opening duration ranges from 6 to 24 hours [181, 182] and seems to be related to some acoustic parameters such as pressure and pulse length [183].

- ***Non-invasiveness*****.** The intrinsic nature of US avoids any surgical procedure, due to the possibility to transmit the energy transcranially.

- ***Safety*****.** Even if this is still an open issue, it has been preliminarily demonstrated that the use of FUS in an appropriate range and in combination with MB can

cause BBB opening without any histological evidence of hemorrhages, ischemia or apoptosis [181, 184, 185].

Recently, it has been demonstrated that the BBB is not only a physical barrier: it possesses in fact several functions, of primary importance for vascular and neural physiology. Aryal et al. [186] demonstrated that FUS has an important role in the modulation of P-glycoprotein (Pgp). This is a protein expressed by the endothelial cells of the BBB playing a major role in the efflux transportation, actively transporting a huge variety of molecules out of the brain capillary endothelial cells, and consequently preserving the brain from harmful substances. The use of US in combination with intravenous MB can actually down-regulate the Pgp for up to 48 hours, thus reversibly enhancing the permeability of the barrier.

Thanks to the progress in Magnetic Resonance (MR) imaging technology and skull aberration correction techniques [187], it is now possible to apply transcranial FUS in the brain with a sub-millimiter precision [188, 189], reducing the risk of side effects. MR imaging allows to perform also Acoustic Radiation Force Impulse (ARFI) [190] imaging in order to verify the position of the focus before the treatment and to confirm the treatment success by using MR contrast agents (*e.g.* gadolinium) that cross the barrier after the procedure.

The integration of a passive cavitation detection system may also allow a real-time monitoring of cavitation that can facilitate the intraoperative treatment monitoring reducing the associated risks [191].

6.2 Passive cavitation detection for BBB opening

Although the exact mechanisms of FUS-induced BBB opening are still not completely understood, it has been shown that the US-induced mechanical oscillations of MB play a primary role in the transient modification of the vascular endothelium.

It has been shown that MB mainly serve as cavitation nuclei; under US excitation, stable or inertial cavitation can appear (Figure 6.3). In the stable cavitation regime bubbles start to repeatedly expand and contract, thus resulting in microstreaming and

shear stress on the vessel wall, that can affect its integrity; at higher acoustic pressure, bubbles oscillation can turn into a violent collapse (inertial cavitation) that causes also localized shock waves and fluid jets. In this latter case, BBB opening can be pursued, but red blood cell extravasation and serious vessel damages can occur [192-194].

Therefore, while stable cavitation is mostly recognized to be responsible for reversible BBB opening, inertial cavitation is normally associated with tissue damages.

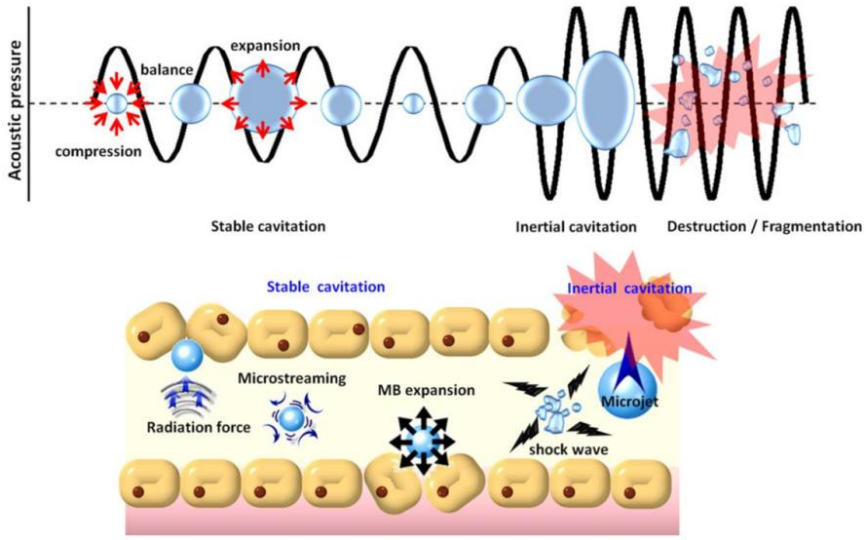

Figure 6.3. *Scheme of blood–brain barrier disruption by FUS. Disruption of the blood–brain barrier can be induced when MB apply mechanical forces on endothelial cells that lead to opening the tight junctions [179].*

The pressure range for a safe and effective BBB opening is quite narrow (*i.e.* from 0.35 to 0.45 MPa in large animals [175]). This pressure window depends on many factors, such as the target area inside the brain, the working frequency, the acoustic coupling, the type, the quantity and the quality of MB, the single response of the animal, etc. Therefore, a real-time monitoring of cavitation, which is the main mechanism responsible for BBB opening, is the preferred method to check in real-time treatment efficiency and safety.

A Passive Cavitation Detector (PCD) can be used to capture acoustic emissions resulting from cavitation. Frequency analysis (*i.e.* spectrum analysis) of the recorded acoustic signal can provide useful information regarding acoustic cavitation regimes (Figure 6.4).

Sharp increasing of harmonic ($f = n*f_0$, $n = 2, 3, 4,...$) and ultra-harmonic ($f = m*f_0$, $m = 3/2, 5/2, 7/2,...$) components of the fundamental frequency (f_0) are typical of stable cavitation events and therefore associated with safe BBB disruption. Broadband emission (*i.e.* white noise) is on the contrary associated with inertial cavitation, and so with tissue damage. The sub-harmonic component ($f_0/2$) seems to be associated with transient cavitation events, as well [7].

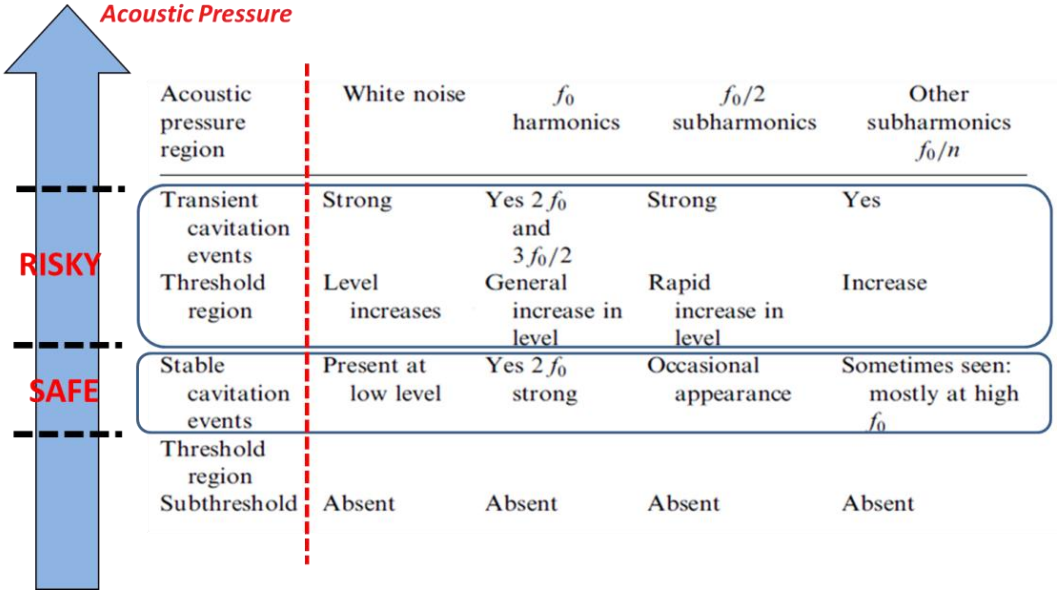

Figure 6.4. *Sensitivity of various cavitation monitoring methods over the range of levels of cavitation activity. Figure readapted from Hill et al. 2004 [7].*

Based on these consideration, stable cavitation dose (SCD) and inertial cavitation dose (ICD) can be defined as follows [195].

- ***SCD:*** sum of the root mean square (RMS) of the harmonic and ultra-harmonic frequency components;

- ***ICD:*** root mean square (RMS) of the broadband signal excluding the frequency bandwidths of stable cavitation dose.

In this work, the frequency components were calculated within bandwidths of 100 kHz around the harmonics and within bandwidths of 50 kHz around the ultra-harmonics.

6.3 FUS induced BBB opening in rats with cavitation control

A system for FUS-induced BBB opening in rats with a real-time monitoring of acoustic cavitation is herein presented.

The main goal of this study was to establish a robust procedure for safe and effective transient BBB permeabilization based on passive cavitation control. The results of this preliminary *in vivo* study enabled to define an experimental protocol for FUS-induced BBB opening experiments under MR guidance on non-human primates, which are currently ongoing at the Commissariat à l'énergie atomique et aux énergies alternatives (CEA, France).

Before the experiments, the focused transducer used for BBB opening in rats was characterized in terms of ultrasonic power. The development of an acoustic radiation force balance and its validation are reported in Section 6.3.1.

6.3.1 Transducer characterization: the Radiation Force Balance

Pressure mapping and beam plotting (see Section 4.2.2) are time-consuming procedures and usually they do not provide all the information required for a complete field characterization of US transducers. Ultrasonic power is, in fact, another very useful information required for a complete characterization of the field.

Radiation force balances (RFBs) are the most common instruments exploited for acoustic power measurements .

They can be classified into reflecting and absorbing ones, depending on the target properties. In both cases, the target can be rigidly linked to the sensor or suspended in a liquid. Guidelines and indications for the design of RFBs have been defined by the International Electrotechnical Commission (IEC) in [196].

When the transducer is directed toward the target, the US beam tends to displace the target from its equilibrium position; this tendency is caused by the radiation force whose magnitude can be detected by the balance [197].

The relationship between the measured force F and the temporal-averaged acoustic power P_{ac} assuming plane waves and a perfect absorbing target, is the following:

$$P_{ac} = c\,F = c\,g\,\Delta m \qquad \text{Eq. 6.1}$$

where c is the speed of sound in the medium and F is given by the product of gravitational acceleration (g) and the difference in weight measured by the balance (Δm). In the case of focused transducers the above relationship modifies as follows:

$$P_{ac} = \frac{2\,c\,g\,\Delta m}{1+\cos\gamma} \qquad \text{Eq. 6.2}$$

where:

$\gamma = arcsin\,(R_t/R_c)$ is the beam convergence angle;

R_t is the radius of the ultrasonic transducer active element;

R_c is the geometrical focal length (radius of curvature of the ultrasonic transducer).

In this work a home- made "weigh all" RFB for measuring acoustic power of transducers was developed and is represented in Figure 6.5.

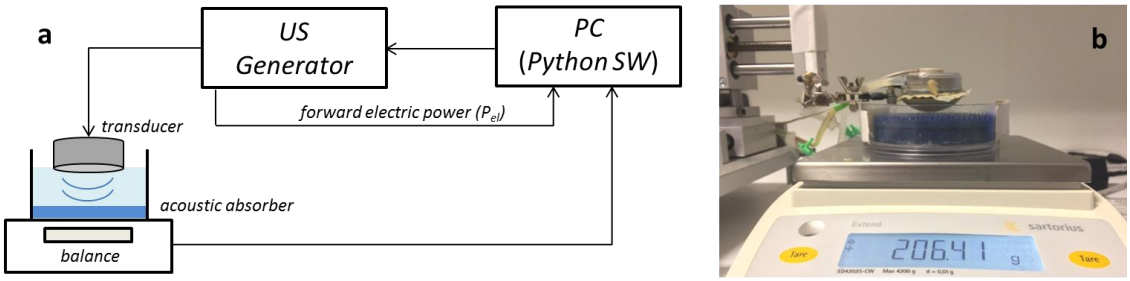

Figure 6.5. *Schematic diagram (a) and picture (b) of the experimental set-up used for acoustic power measurements.*

The system consisted of a digital balance (ED4202S-CW, Sartorious) with 4200 g weighing capacity, 0.01 g resolution and RS232 data interface, weightening a small plastic cylinder including an acoustic absorber and filled with deionized and degassed water. The absorber was composed of two 10 mm thickness layers stuck together: AptFlex F28 at the bottom and AptFlex F28P at the top (Precision Acoustic Ltd). While the bottom layer is a common acoustic absorber, AptFlex F28P is specifically designed to be a target for RFBs. The pyramidal geometry of AptFlex F28P greatly improves the echo reduction (percentage of reflected wave) while preserving a good insertion loss (fraction of transmitted wave), furtherly reduced by the additional layer of AptFlex F28.

The transducer was mounted on a 3D positioning system and placed 0.7 times the focal distance far from the absorber.

The RFB was remotely controlled by a dedicated program developed in Python, allowing to automatically control the US generator (32 channels, 10 Watt/channel, Image Guided Therapy), to acquire the forward electrical power sent to the transducer and to capture data from the balance with a sampling frequency of 5 Hz.

For performing the experiments described in this section, the exposure time was set to 3 seconds to avoid overheating of the transducer, driven with a continuous-wave.

Acquisition started 3 seconds before the shot and ended 4 seconds after, for baseline measurement. A typical signal acquired from the balance is reported as an example in Figure 6.6.

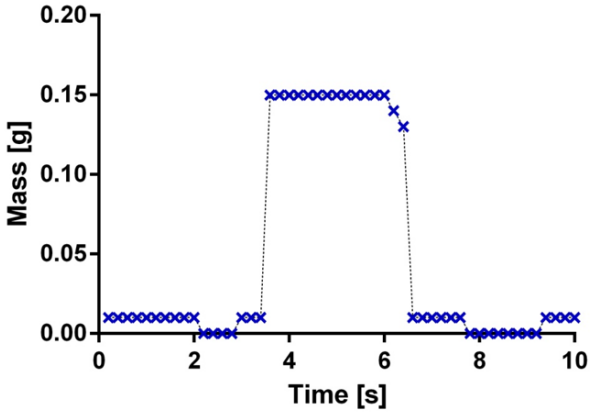

Figure 6.6. *Example of signal acquired from the balance for acoustic power measurements. The transducer is turned on at t = 3 sec (continuous-mode excitation for 3 seconds).*

Data were saved in txt format and post-processed with a custom made code, which basically read the data and implements Equation 5.2. Temperature was measured before each experiment and speed of sound (c) was consequently calculated using the 5th order polynomial interpolation proposed by Marczak [71].

Thirteen different experimental session were performed for the characterization of a 6 channels annular array focused transducer with a central frequency of 650 kHz (Imasonic) used for the *in vivo* experiments described in Section 6.3.2. The FUS transducer was provided with the same acoustic coupling system (latex membrane filled with degassed water) used during the tests.

Figure 6.7 shows the measured acoustic power for a wide input power range, mainly limited by instrumentation constraints and safety-related limits. Figure 6.7-a reports the results of acoustic power at different normalized generator output voltages, while Figure 6.7-b shows the results of acoustic power at different electric input powers.

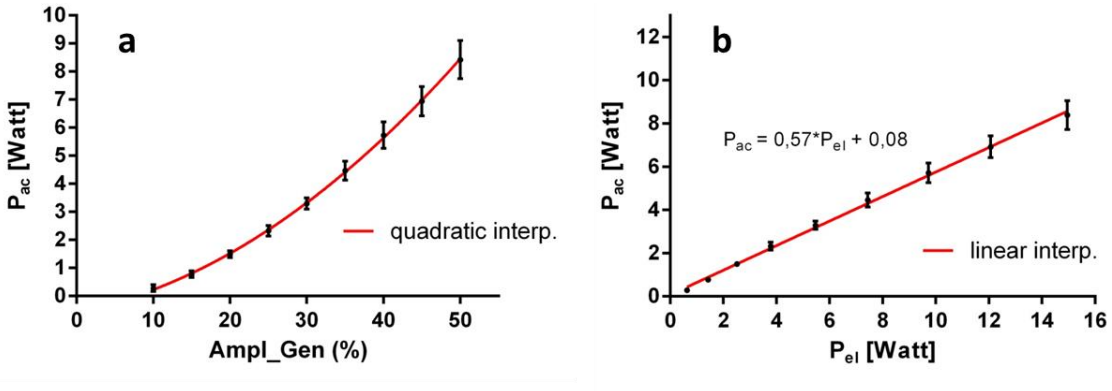

Figure 6.7. *Acoustic power characterization of the 6 channels (650 kHz, Imasonic) transducer using the 32 channels generator (10 Watt/channel, Image Guided Therapy). a) Results of acoustic power [Watt] at different normalized generator output voltages; b) results of acoustic power [Watt] at different electric input powers [Watt] sent to the transducer. Red lines represent quadratic and linear data interpolation, respectively. The slope of the linear interpolation represent the efficiency of the system.*

The efficiency of the system (η), defined as the ratio between the electric input power of the transducer acoustic and the acoustic measured power was 57%. As described in Eq. 5.3 three different factors contribute to the overall efficiency: the efficiency of the transducer (η_{tr}) (electrical into mechanical energy conversion), the transmission factor of the membrane (η_m) and the efficiency of the developed radiation force balance (η_{rfb}).

$$\eta = \eta_{tr} * \eta_m * \eta_{rfb} \qquad \text{Eq. 6.3}$$

It is worth mentioning that the developed balance has been tested to characterize the 6 channels (650 kHz) transducer that has been used for the experiment described in Section 6.3.2, but the system described above can be easily readapted for different transducers and generators.

6.3.2 *In vivo* experiments: protocol

The transducer (6 channels annular array, center frequency 650 kHz, active diameter 30 mm, Imasonic) used for FUS-induced BBB opening experiments on rats was provided with a confocal planar mono-element transducer (center frequency 1.5 MHz, diameter 4.5 mm, Imasonic) acting as PCD (Figure 6.8).

The therapeutic transducer was driven by an RF amplifier (LabFUS, Image Guided Therapy) and an oscilloscope (PicoScope 5242B, Pico Technology) was used to acquire the signal detected by the PCD. All the procedure was controlled and synchronized by a software developed in Python (version 2.7.12, Python Software).

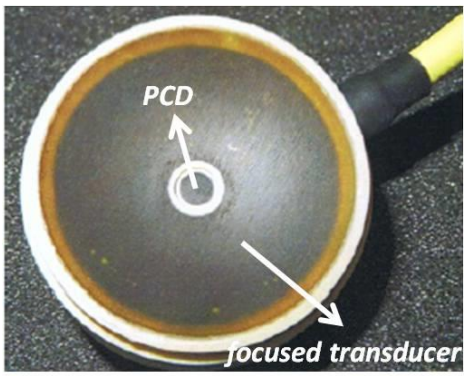

Figure 6.8. *Passive cavitation detector (PCD) positioned at the center of the 6 channels focused transducer.*

The protocol used for the experiments was the following:

1. ***Set-up preparation.*** The transducer was fixed within a stereotactic frame and a latex membrane was completely filled with degassed water for ensuring adequate acoustic coupling between the transducer and the animal's head (Figure 6.9).

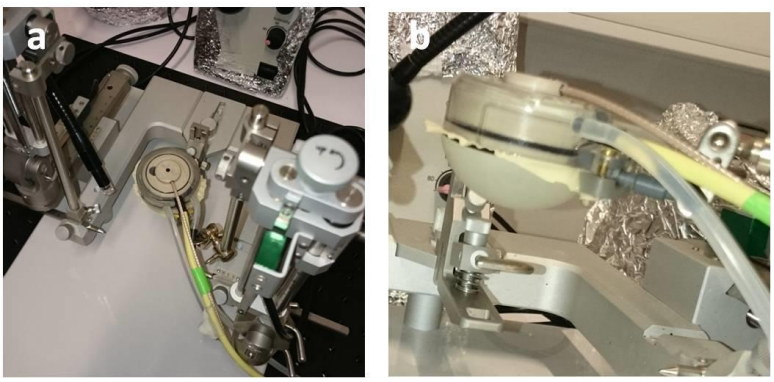

Figure 6.9. *FUS transducer with the latex membrane filled with degassed water integrated inside the stereotactic frame (a. Top view, b. Lateral view).*

2. ***Animal preparation***. Rats were anesthetized with ketamine/xylazine (8.2 mL/kg, intraperitoneal injection) and positioned within the stereotactic frame using ear bars (Figure 6.10). Acoustic coupling gel was also applied to the animal's head.

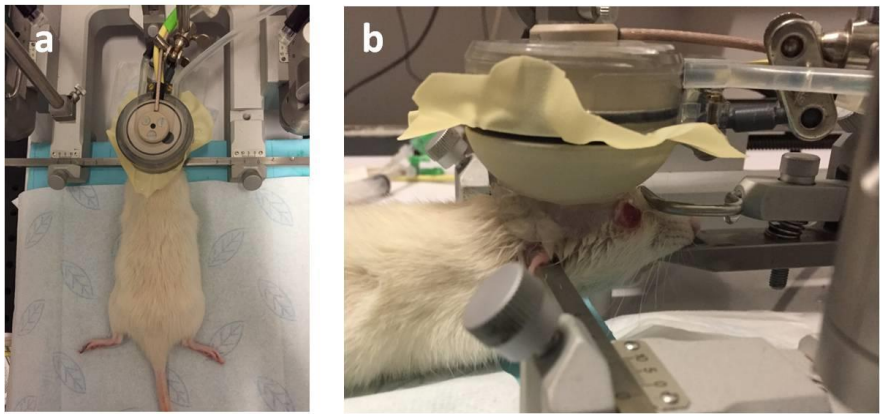

Figure 6.10. *Experimental set-up for FUS-induced BBB opening in rats (a. top view , b. lateral view). The anesthetized animal is fixed in a stereotaxic frame through ear bars.*

3. ***Acoustic coupling verification***. The acoustic coupling quality was checked with the following procedure. A complete PCD baseline acquisition was acquired before MB injection for incremental acoustic pressures. Smooth growing of the stable cavitation (SCD) with no broadband emissions of inertial cavitation (ICD) were observed when adequate acoustic coupling was obtained (Figure 6.11, top). On the other hand, inadequate coupling caused by bubbles trapping in the water balloon or in the acoustic coupling gel or due to insufficient degassing of water, could be identified by broadband emissions (ICD) and sharp variation of the SCD (Figure 6.11, bottom).

   The overall procedure (degassing water, positioning of the acoustic coupling membrane and acoustic coupling verification) was repeated, in case of inadequate coupling.

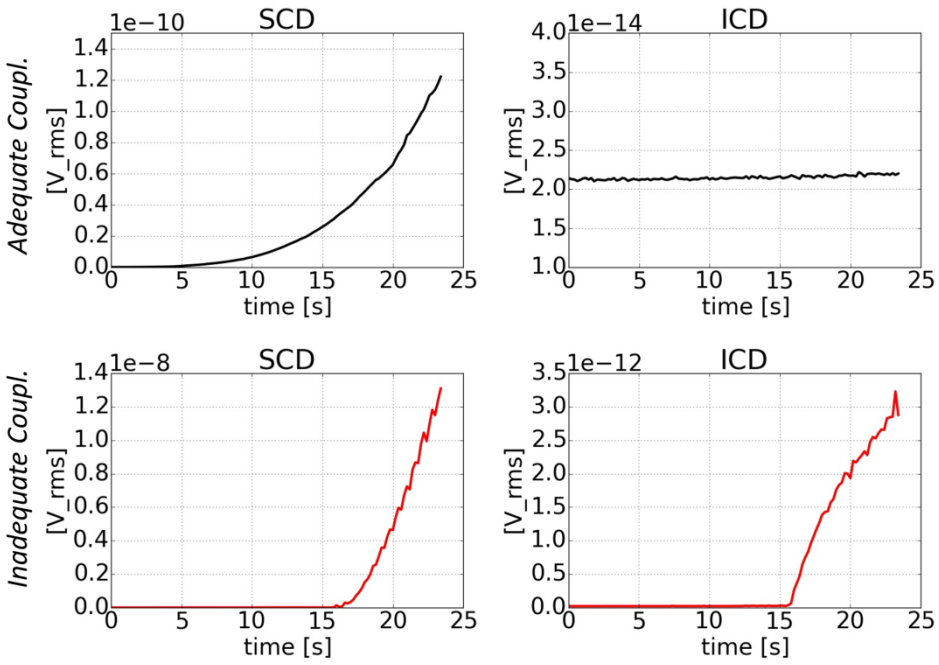

Figure 6.11. *Stable cavitation dose (SCD) and inertial cavitation dose (ICD) during a sonication without microbubbles. Black lines represent typical cavitation doses if the acoustic coupling is adequate; red lines represent typical cavitation doses of inadequate acoustic coupling.*

4. ***BBB opening with cavitation monitoring***. MB were injected intravenously (SonoVue: 200 µL), after a control acquisition (baseline acquisition). Sonication was performed at 650 kHz for 180 s, with a pulse length of 10 ms and pulse repetition frequency of 10 Hz. The frequency components of the signal acquired by the PDC (sampling frequency of 31.25 MHz) were quantified by computing the Fast Fourier Transform (FFT) using the library pyFFTw [198].

   During the whole sonication, SCD and ICD were computed for each pulse. The control algorithm was based on a relative method [199]; for each acoustic pressure the relative power spectrum was calculated as the ratio between the instantaneous signal power spectrum after MB injection and the correspondent baseline power spectrum.

   The closed loop control allowed the acoustic pressure to increase until a defined SCD was reached, and to decrease as soon ICD events were detected.

An example of spectrum where stable cavitation components were detected is shown in Figure 6.12-a, while the spectrum reported in Figure 6.12-b is typical of an inertial cavitation regime.

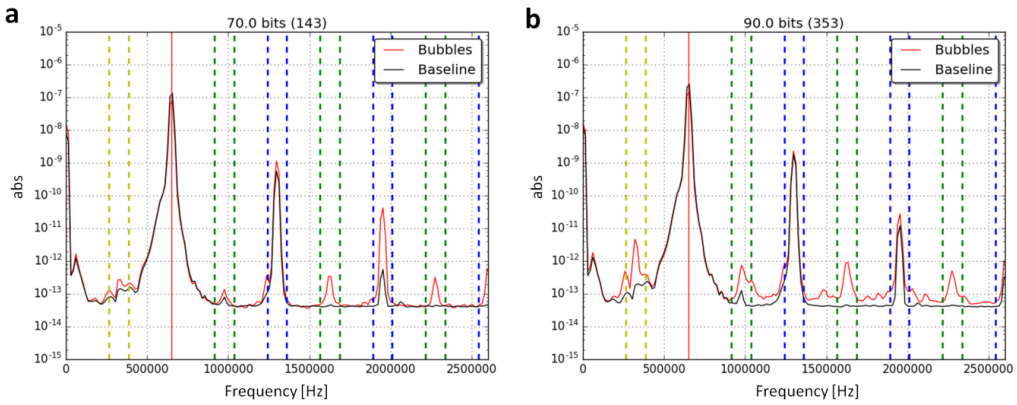

Figure 6.12. *Typical spectra acquired in stable cavitation (a), and inertial cavitation (b) regimes. Harmonic components are quantified within the blue bands, ultra-harmonics in the green bands and the sub-harmonic component in the yellow band. ICD is calculated between these bands. A sharp increasing of harmonic and ultra-harmonic components of the fundamental frequency is clear in (a), while broadband emission (i.e. white noise) and the appearance of the sub-harmonic component is visible in (b).*

5. ***Evans blue injection and gross pathology***. After sonication, Evans blue dye was injected intavenously (150 µL/ 100 mg). Evans blue is the most commonly used marker for the verification of the BBB integrity [200], since this dye extravasates in the brain only where the BBB is disrupted and is visible to the naked eye, thus providing a gross indication of BBB opening.

   After approximately 30 minutes from sonication, animals were sacrificed and the brain was manually sliced into thin coronal sections of approximately 2 mm.

   For a better visualization of the Evans blue within the brain and in order to discriminate possible hemorrhages, the blood was removed using a saline perfusion system.

6.3.3 *In vivo* experiments: results

Two representative cases are reported in Figure 6.13. The left column reports a case of a "safe" opening, while the right column reports a case of an "unsafe" one, where the acoustic pressure was not properly controlled.

Evans blue extravasation, as well as stable cavitation events, appear clear in both cases. However bleeding, associated with brain damages, is evident only in the case where also inertial cavitation events were detected. This seems to demonstrate a clear correlation between BBB-opening and stable cavitation, and between erythrocyte extravasation and inertial cavitation.

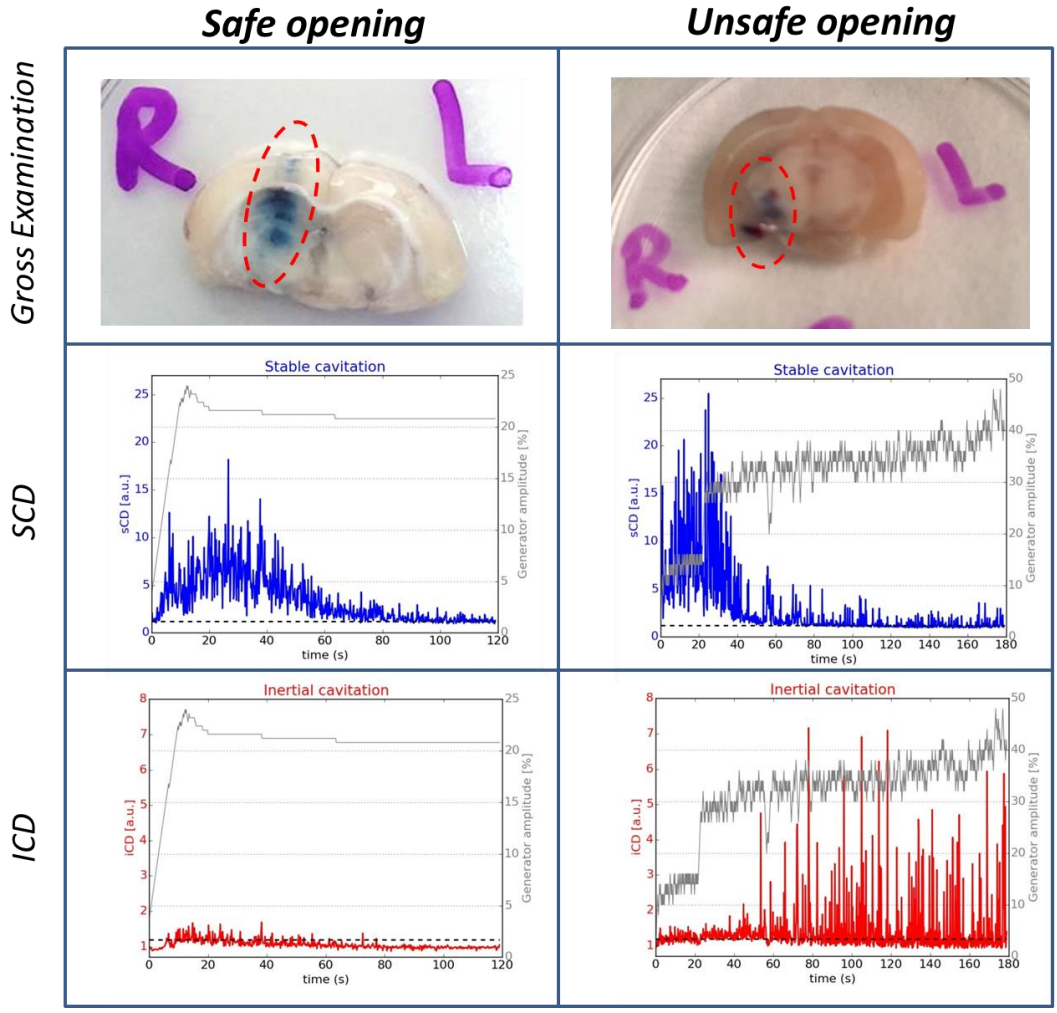

Figure 6.13. *FUS-induced BBB opening in rats with PCD analysis.* ***Top****. Representative sagittal gross views of rat brain after US exposure and Evans Blue injection: a "safe" case where opening was clear and bleedings were not observed (left), and an "unsafe" case where also bleedings were observed (right).* ***Middle****. Representative graphs of stable cavitation doses (SCD): "safe" opening (left) and "unsafe" opening (right); in both cases stable cavitation, that is associated with not dangerous opening, is present.* ***Bottom.*** *Representative graphs of inertial cavitation doses (ICD) that is linked with tissue damages; ICD peaks are present only in the "unsafe" opening (right).*

Although these results are preliminary (since deriving from a reduced number of experiments), they demonstrate that real time PCD control during FUS-induced BBB opening can ensure the efficiency and the safety of the process.

MB activity detected in real-time by PCD appears as a reliable monitoring parameter. SCD can be a useful parameter to demonstrate effective MB activity, while ICD, associated with damages, can serve as a parameter to set a threshold of acoustic pressure for a safe sonication.

Starting from this study and these considerations, a passive cavitation detection based feedback control method was finalized and recently successfully tested on non-human primates at the Commissariat à l'énergie atomique et aux énergies alternatives (CEA, France).

Scientific production (Chapter 6)

Papers submitted to Internationals journals

- H. A. S. Kamimura, J. Flament, J. Valette, **A. Cafarelli**, R. A. Badin, P. Hantraye, & B. Larrat. "Ultrasound-mediated blood brain-barrier disruption in non-human primates using relative-based spectra of cavitation for feedback control". Scientific Reports.

Papers submitted to International conferences

- H. A. S. Kamimura, J. Flament, J. Valette, **A. Cafarelli**, R. A. Badin, P. Hantraye, & B. Larrat. "MRI guided ultrasound-mediated blood-brain barrier opening in non-human primates using passive cavitation detection based feedback control". 2017 IEEE International Ultrasonics Symposium (IUS). Washington, 6-9 Sept 2017.

7 Conclusions

Therapeutic Ultrasound is an exponentially growing research field that can potentially transform the treatment of many medical disorders (cancer, neurodegenerative diseases, etc..), by using ultrasonic energy to precisely target tissue deep in the body without incisions or radiation, hence in a truly minimally invasive manner. However, despite the encouraging results obtained in preclinical and clinical studies and the promising features of this innovative technology, some open issues still have to be addressed.

The major open problems which hamper further development of therapies based on US are related to the optimization of the acoustic stimulation, the formulation of US-responsive materials and a deeper understanding of the interaction between US and cells, US and tissues and US and materials which could enhance the US effect.

Unfortunately, many users and researchers in this field operate US by using non standardized configurations, vulnerable to errors during calibration and use. Therefore, the results available in the state-of-the-art are hardly comparable, slowing down the progress of this technology.

The work which led to the preparation of this thesis was based on, and driven by, these considerations. The main contribution of the candidate in the scientific achievements reported in this thesis are summarized in the following:

- *Development of acoustically tuned materials for US phantoms and smart substrates for cell culture.* An experimental set-up for measuring speed of sound and attenuation was developed. AG, PAA and PDMS materials at different concentrations and doped with different concentrations of $BaTiO_3$ were characterized both acoustically and mechanically. In addition, it was demonstrated how these data can be used to develop custom tissue-mimicking phantoms and to fabricate smart materials for stimulating cells with a highly controlled US dose. (Chapter 3)

- *Design, realization and calibration of an experimental set-up for in vitro LIPUS stimulation*. The aim was to minimize the typical exposure errors that normally

affect a vast majority of current systems used for *in vitro* ultrasound cell stimulation, providing highly controlled US exposure on cells. An experimental system for in vitro LIPUS cell stimulation, with the possibility to explore several ultrasound stimulation parameters, such as intensity, therapy duration, duty cycle and also frequency, was designed, characterized and validated by studying the influence of LIPUS on skeletal muscle regeneration. (Chapter 4)

- *In-vitro and ex-vivo assessment of an innovative robotic platform for focused ultrasound treatments.* A dedicated HIFU transducer was characterized and integrated within a robotic platform intended for FUS treatments. The overall US guided procedure was assessed both in static and dynamic conditions, exploiting *in vitro* and *ex vivo* dedicated models. (Chapter 5)

- *Optimization of a safe and effective FUS-induced BBB opening in vivo procedure*. A procedure for safe and effective transient BBB permeabilization in rats, based on real-time passive cavitation detection, was presented. A clear correlation between safe BBB opening and stable cavitation and between unsafe erythrocyte extravasation and inertial cavitation was demonstrated. (Chapter 6)

All these activities, dealing with different aspects of therapeutic US, were investigated following the same scientific approach. In particular, well-characterized and reproducible systems for US studies were developed, by paying specific attention to the characterization of US sources, proper design of set-ups and correct reporting of exposure conditions.

By better controlling the US beam, and only thanks to a synergic contribution by physicians, physicists, engineers and biologists, US could address the unmet clinical needs and provide treatments which are superior to the best current therapies, thereby improving the quality of life and longevity for millions of patients around the world.

APPENDIX A: Abbreviations

AG	=	Agarose
ARFI	=	Acoustic Radiation Force Impulse
BBB	=	Blood Brain Barrier
c	=	speed of sound
DC	=	Duty cycle
f	=	frequency
HIFU	=	High Intensity Focused Ultrasound
ICD	=	Inertial Cavitation Dose
IEC	=	International Electrotechnical Commission
IV	=	Intravenous
LIPUS	=	Low Intensity Pulsed Ultrasound
MB	=	Microbubbles
MR	=	Magnetic Resonance
MRgFUS	=	Magnetic Resonance guided Focused Ultrasound
FUS	=	Focused Ultrasound (Surgery)
PAA	=	Polyacrylamide
PCD	=	Paasive Cavitation Detector
PDMS	=	Polydimethylsiloxane
Pgp	=	P-glycoprotein
PRF	=	Pulse Repetition Frequency
RFB	=	Radiation Force Balance
RMS	=	Root Mean Square
SCD	=	Stable Cavitation Dose
tcMRgFUS	=	transcranial MRgFUS
TMMs	=	Tissue-Mimicking Materials
US	=	Ultrasound
USgFUS	=	Ultrasound guided Focused Ultrasound
Z	=	acoustic impedance
α	=	attenuation coefficient

APPENDIX B: Scientific Production

Publications on Internationals journals

- **A. Cafarelli**, L.Ricotti, A. Verbeni, A: Poliziani, P. Dario, A. Menciassi. "Tuning mechanical and acoustic properties of materials for ultrasound phantoms and smart substrates for cell cultures". *Acta Biomaterialia.2017*

- S. Tognarelli, G. Ciuti, A. Diodato, **A. Cafarelli**, A. Menciassi. "Robotic Platform for High-Intensity Focused Ultrasound Surgery under Ultrasound Tracking: the FUTURA Platform", *Journal of Medical Robotic Research. 2017*

- A. R. Salgarella, **A. Cafarelli**, L. Ricotti, L. Capineri, P. Dario, A. Menciassi. "Optimal ultrasound exposure conditions for maximizing C2C12 muscle cell proliferation and differentiation". *Ultrasound in Medicine and Biology 2017*

- **A. Cafarelli**, P. Miloro, A. Verbeni, M. Carbone, and A. Menciassi. "Speed of sound in rubber-based materials for ultrasonic phantoms". *Journal of Ultrasound, 2016;*

- L. Ricotti, **A. Cafarelli**, V. Iacovacci, L. Vannozzi, and A. Menciassi. "Advanced Micro-Nano-Bio Systems for Future Targeted Therapies". *Current nanoscience, 2014*;

- A. Verbeni, **A. Cafarelli**, P. Miloro, and A. Menciassi, "Inertial cavitation detection during in-vitro sonothrombolysis". Abstract. *Journal of Therapeutic Ultrasound. 2014*;

Publications submitted to Internationals journals

- H. A. S. Kamimura, J. Flament, J. Valette, **A. Cafarelli**, R. A. Badin, P. Hantraye, & B. Larrat. "Ultrasound-mediated blood brain-barrier disruption in non-human primates using relative-based spectra of cavitation for feedback control". Scientific Reports.

Papers in preparation

- A. Diodato, **A. Cafarelli**, A. Schiappacasse, G. Ciuti, S. Tognarelli and A. Menciassi. "USgFUS robotic system for moving target with a pivoting skin contact point". Physics in Medicine and Biology. To be submitted by 30 of June 2017.

- **A. Cafarelli**, L. A. Chanel, F. Di Bartolo, H. Locteau, S. Tognarelli, E. Dumont and A. Menciassi. "Ultrasound Acoustic Radiation Force Impulse (US-ARFI) imaging for localization of HIFU focal spot". Ultrasonics. To be submitted by 30 of June 2017.

Patents

- **A. Cafarelli**, L. Ricotti, A. Menciassi. Italian patent: "Sistema di stimolazione ad ultrasuoni di un campione in vitro", filing no. 102016000052583, filing date: May 2016.

Papers presented at International conferences

- **A. Cafarelli**, A. Diodato, S. Tognarelli, M. Mura, G. Ciuti, A. Menciassi, "The FUTURA robotic platform for USgFUS". 28th Conference of the international Society for Medical Innovation and Technology (SMIT). Delft, October, 2016.

- A. Diodato, **A. Cafarelli,** A. Schiappacasse, L.A. Chanel, S. Tognarelli, G. Ciuti, A. Menciassi, "Computer-assisted robotic platform for USgFUS treatment". 6th Joint Workshop on New Technologies for Computer Assisted Surgery (CRAS). Pisa, September, 2016;

- A. Menciassi, S. Tognarelli, **A. Cafarelli**, A. Diodato, G. Ciuti, "Multifunctional robotic platform for USgFUS". 5th International Symposium on Focused Ultrasound. Washington, August, 2016;

- **A. Cafarelli**, A. Diodato, A. Schiappacasse, S. Tognarelli, G. Ciuti, A. Menciassi, "Robotic platform for Focused Ultrasound Surgery". 6th Congresso Gruppo Nazionale di Bioingegneria (GNB). Napoli, June, 2016;

- **A. Cafarelli**, A. Diodato, M. Mura, S. Tognarelli, L. Ricotti, G. Ciuti, A. Menciassi, “A tissue-mimicking phantom for in-vitro accuracy evaluation of USgHIFU procedures”. 3rd European Symposium on Focused Ultrasound Therapy. London, October, 2015; AWARDED AS BEST ORAL PRESENTATION.

- S. Tognarelli, G. Ciuti, A. Diodato, **A. Cafarelli**, M. Mura & A. Menciassi. "Robotic platform for high-intensity focused ultrasound surgery under ultrasound monitoring and guidance: the FUTURA platform". 5th Joint Workshop on New Technologies for Computer Assisted Surgery (CRAS). Brussels, September, 2015;

- **A. Cafarelli**, M. Mura, A. Diodato, A. Schiappacasse, M. Santoro, G. Ciuti, A. Menciassi. " A computer-assisted robotic platform for Focused Ultrasound Surgery: assessment of high intensity focused ultrasound delivery ". 37th Annual International Conference of the IEEE Engineering in Medicine and Biology Society (EMBC). Milan, August, 2015;

- A. R. Salgarella, L. Ricotti, G. Giudetti, J. Kronek, M. Righi, A.Cutrone, **A.Cafarelli**, A. Zahoranová, P. Šramková, D. Treľová, S. Bossi, S. Micera, I. Lacík, A. Menciassi. "Advanced nano-doped materials for long-term neural interfaces". 15th International Conference on Nanotecnology (IEEE NANO). Rome, July, 2015;

- S. Tognarelli, G. Ciuti, A. Diodato, P. Miloro, A. Verbeni, **A. Cafarelli**, & A. Menciassi. "FUTURA: a computer-assisted robotic platform for high-intensity focused ultrasound". 4th Joint Workshop on New Technologies for Computer Assisted Surgery (CRAS). Genova, October, 2014;

- A. Verbeni, **A. Cafarelli**, P. Miloro and A. Menciassi, "An experimental system for the study f the mechanism of sonothrombolysis" .5th Congresso Gruppo Nazionale di Bioingegneria (GNB). Pavia, June, 2014;

- A.Verbeni, G. Ciuti, **A. Cafarelli**, P. Miloro, A. Diodato, S. Tognarelli, & A. Menciassi. "The FUTURA platform: a new approach merging non-invasive ultrasound therapy with surgical robotics". 36th Annual International Conference of the IEEE Engineering in Medicine and Biology Society (EMBC). Chicago, August, 2014;

- S. Tognarelli, P. Miloro, A. Verbeni, M. Mura, **A. Cafarelli**, G. Ciuti, P. Dario, A. Menciassi. "Low invasive therapy under robotic guidance in the vascular district: a case study". 3rd Joint Workshop on New Technologies for Computer/Robot Assisted Surgery (CRAS). Verona, September, 2013;

- **A. Cafarelli**, A. Verbeni, P. Miloro and A. Menciassi, "Qualitative Assessment of Thermal Effects in High Intensity Ultrasound Thrombolysis Experiments" . 25th International Conference of the Society for Medical Innovation and Technology (SMIT) . Baden-Baden, September, 2013;

Papers submitted to International conferences

- H. A. S. Kamimura, J. Flament, J. Valette, **A. Cafarelli**, R. A. Badin, P. Hantraye, & B. Larrat. "MRI guided ultrasound-mediated blood-brain barrier opening in non-human primates using passive cavitation detection based feedback control". 2017 IEEE International Ultrasonics Symposium (IUS). Washington, 6-9 Sept 2017.

- A. Diodato, A. Schiappacasse, **A. Cafarelli**, S. Tognarelli, G. Ciuti and A. Menciassi. "Robotic-assisted platform for USgFUS treatment of moving organs". 10th Hamlyn Symposium on Medical Robotics. London, 25-28 June 2017.

- L. Ricotti, I.Di Cioccio, A. R. Salgarella, **A. Cafarelli**, P. Losi, M. C. Barsotti, I.Foffa, P. Dario, A. Menciassi and G. Soldani "Nanocomposite small diameter vascular graft stimulated by ultrasound waves" 2017 Fall Meeting of the Materials Research Society (MRS 2017). Boston 26 Nov - 1 Dec 2017.

APPENDIX C: Additional material on acoustic and mechanical characterization of AG, PAA, PDMS.

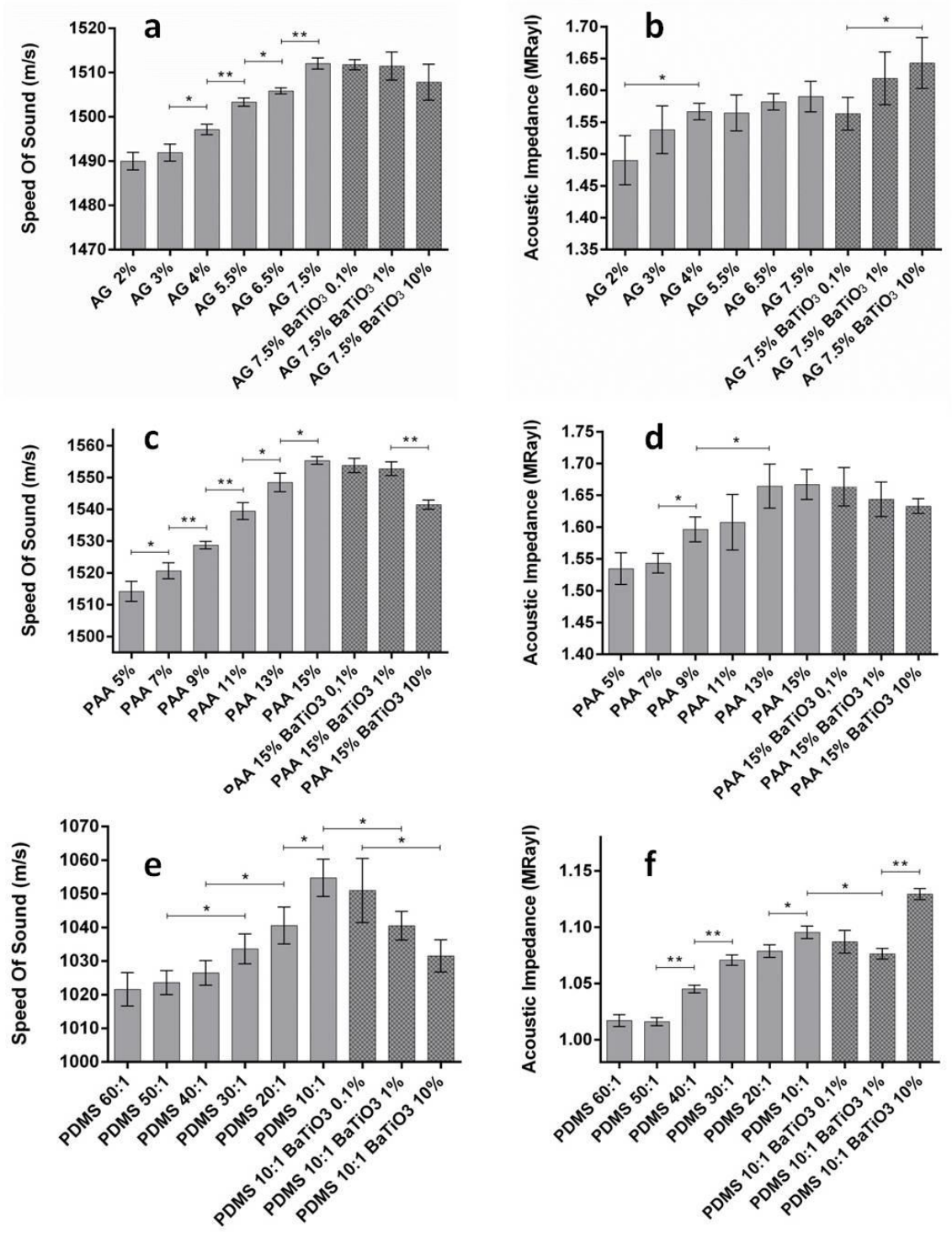

Figure A.1. *Speed of Sound (c) and Acoustic Impedance (Z) for the tested materials: (a) AG c; (b) AG Z; (c) PAA c; (d) PAA Z; (e) PDMS c; (f) PDMS Z. Gridded bars refer to samples doped with $BaTiO_3$ nanoparticles. At least 3 independent samples were tested for each sample type. *=p<0.05, **=p<0.01.*

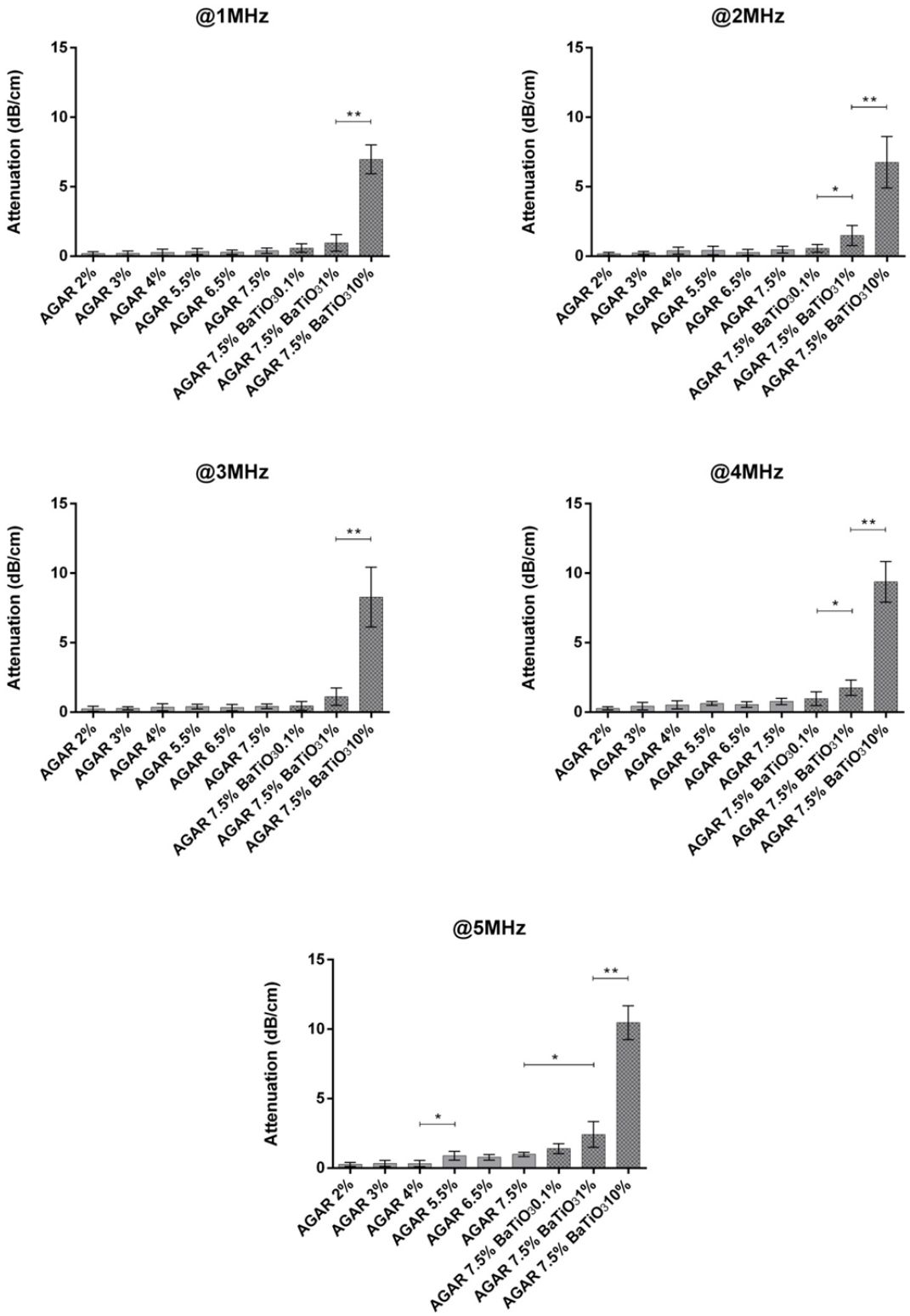

Figure A.2. *Attenuation Coefficient (α) for AG and related nanocomposites, measured at 1,2,3,4 and 5 MHz . At least 3 independent samples were tested for each sample type. Statistical comparisons refer to values on each column: each sample is compared with the one reported in the row immediately above. *=p<0.05, **=p<0.01.*

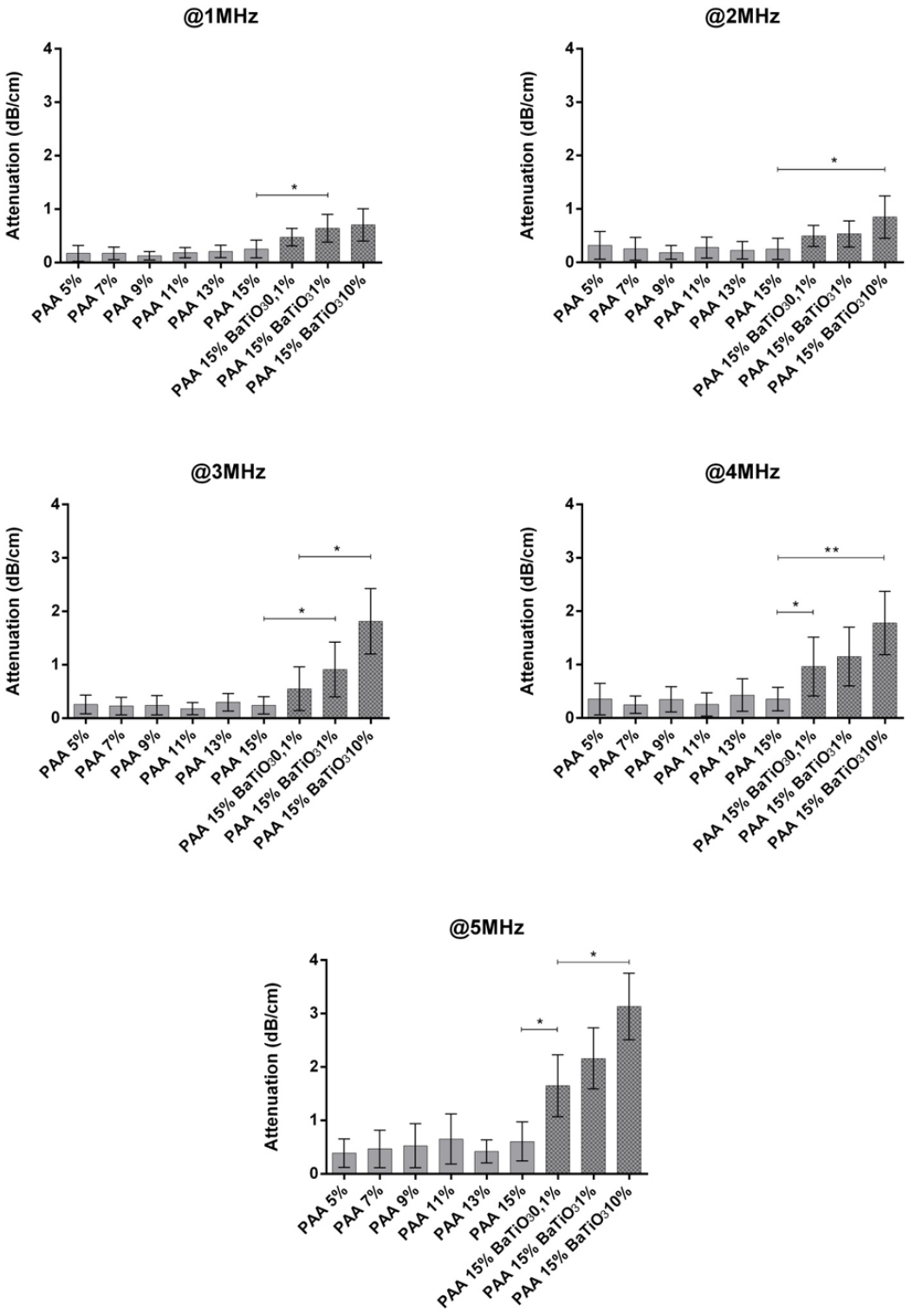

Figure A.3. *Attenuation Coefficient (α) for PAA and related nanocomposites, measured at 1,2,3,4 and 5 MHz . At least 3 independent samples were tested for each sample type. Statistical comparisons refer to values on each column: each sample is compared with the one reported in the row immediately above. *=p<0.05, **=p<0.01.*

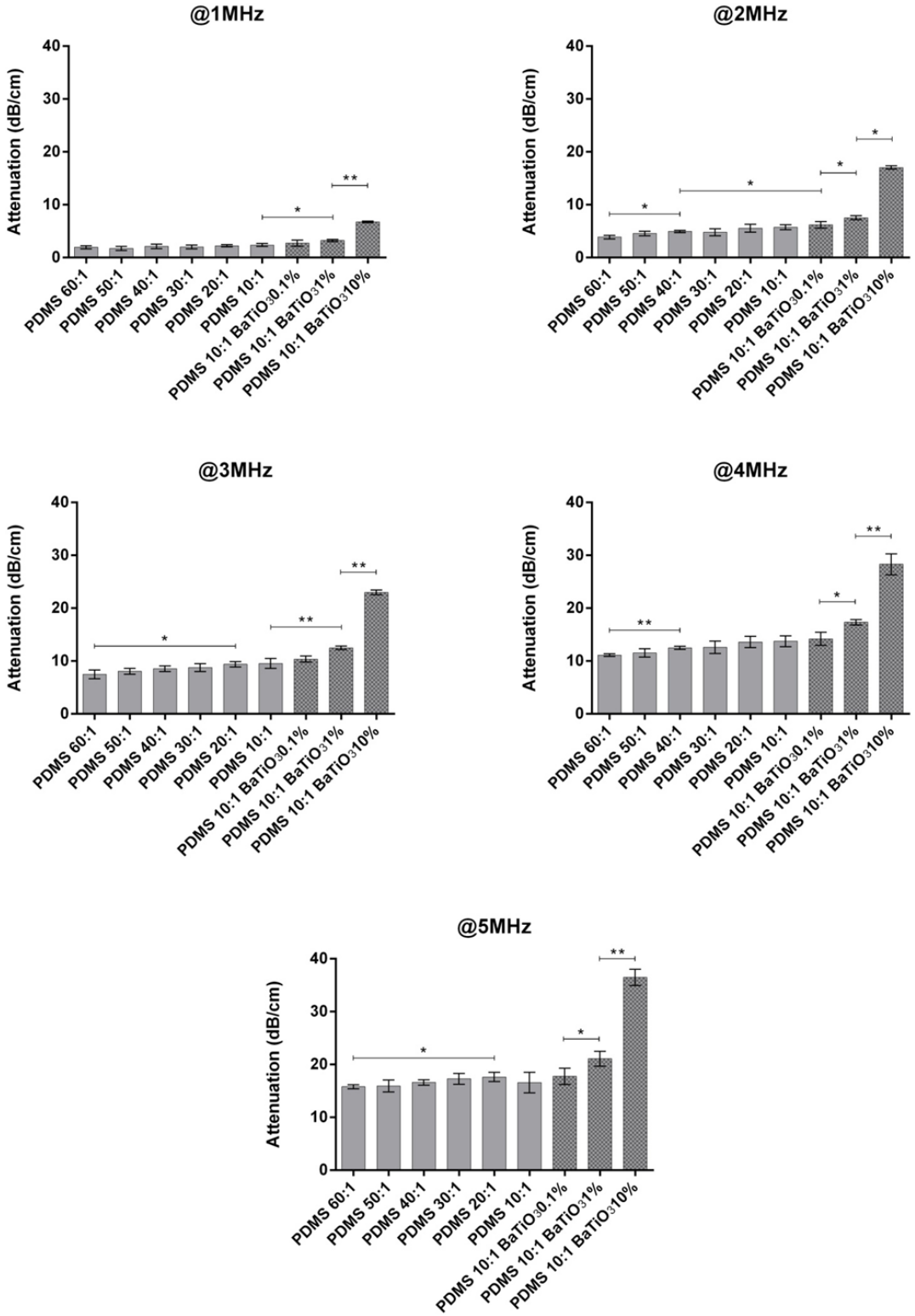

Figure A.4. *Attenuation Coefficient (α) for PDMS and related nanocomposites, measured at 1,2,3,4 and 5 MHz . At least 3 independent samples were tested for each sample type. Statistical comparisons refer to values on each column: each sample is compared with the one reported in the row immediately above. *=p<0.05, **=p<0.01.*

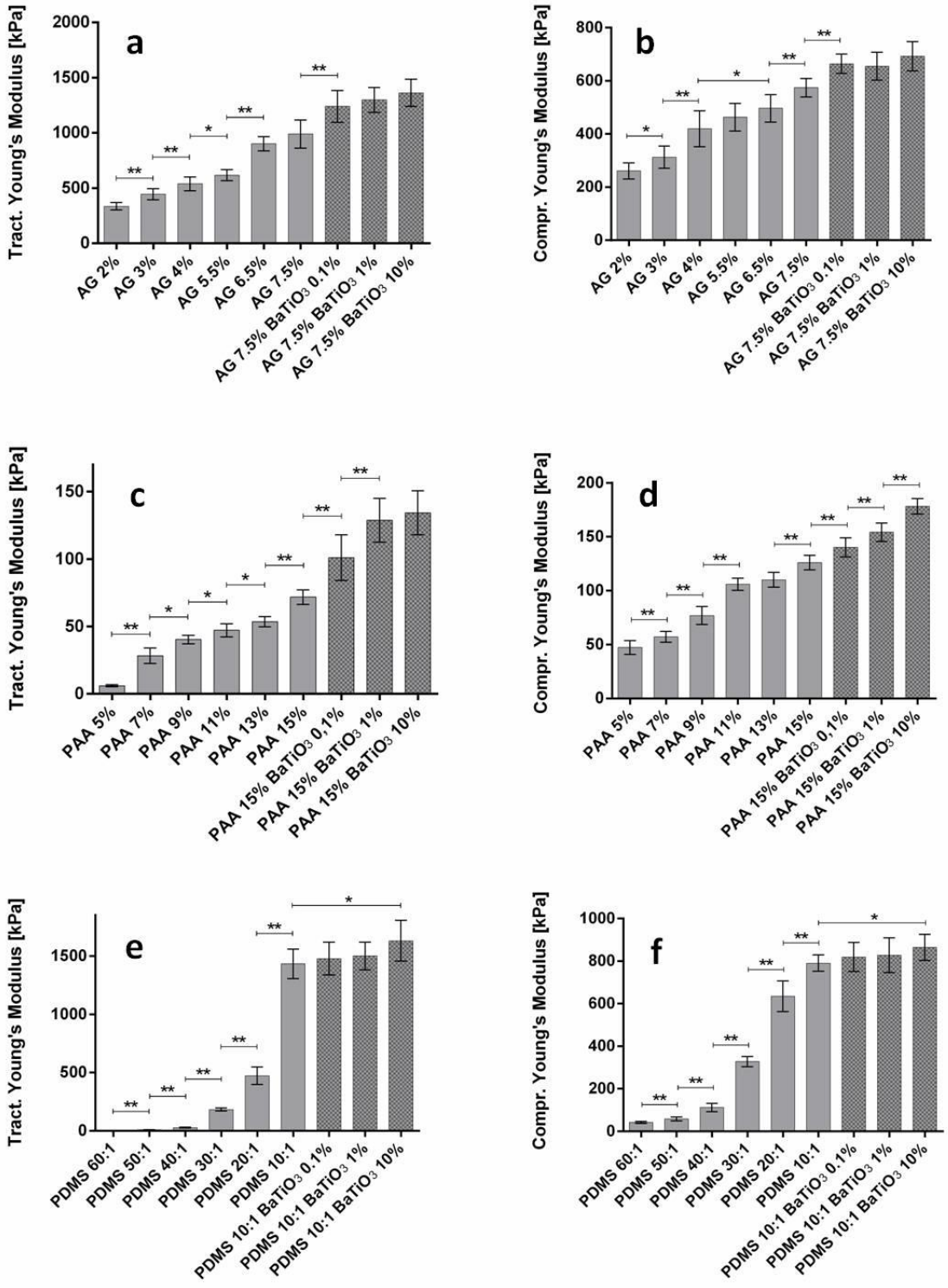

Figure A.5. *Young's moduli, derived from traction and compression tests performed on the different materials: (a) AG traction; (b) AG compression; (c) PAA traction; (d) PAA compression; (e) PDMS traction; (f) PDMS compression. Gridded bars refer to samples doped with $BaTiO_3$ nanoparticles. At least 7 independent samples were tested for each sample type. *=p<0.05, **=p<0.01.*

APPENDIX D: Design of a LIPUS stimulation set-up with a real-time optical monitoring

The integration of a real-time monitoring system (optical microscope, high-speed video-camera, etc.) within in vitro LIPUS stimulation set-ups would undoubtedly be of great interest in the field. A real-time monitoring of the target (cells, drug delivery vectors, et.) would allow a better understanding of the involved bio/non-bio phenomena in LIPUS stimulation.

However, the integration of a monitoring system within LIPUS set-ups is challenging and currently used solutions have some limitations with regard to the correct exposure of the cells to US energy [201-204]. Taking into account considerations of Section 4.1, this jeopardizes the reproducibility of the experiments. Commercial US transducers are in fact not transparent to light and consequently the US stimulation system and the optical imaging system cannot be aligned and must be positioned on different axes; this creates geometrical configuration problems and exposure inhomogeneities on the target due to the non-perpendicularity of the US beam.

Starting from this problem, an innovative LIPUS stimulation set-up that allows to stimulate a target in a correct, controlled and highly reproducible way and to monitor in real-time the target during the exposure by means of an optical imaging system, was designed and patented [205].

The proposed set-up is featured by an US exposure system positioned at 90° respect to the optical imaging system (*e.g.* a microscope objective) and by an acoustically fully reflective (but optically transparent) interface able to properly deviate the US beam but allow the passage of light. The target will thus be homogeneously exposed to the US radiation but it could be also imaged in bright field or fluorescence. A schematic example of the system architecture and components is shown in Figure A.6.

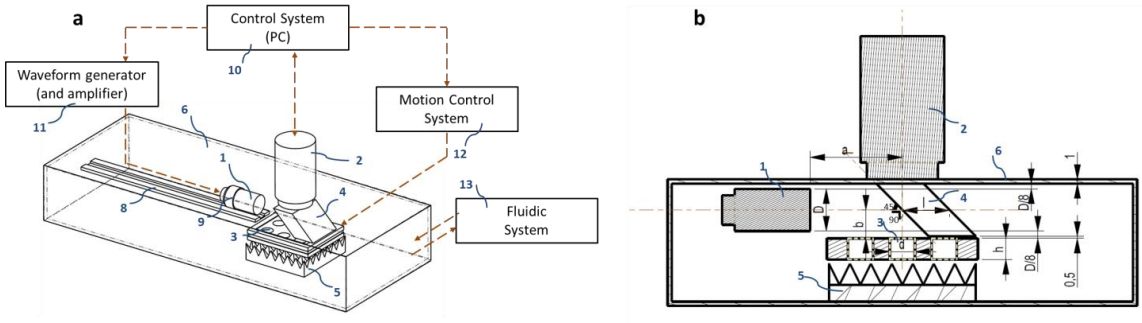

Figure A.6. *Depiction of the overall architecture of the target LIPUS stimulation system. (a) 3D view and (b) cross-sectional view of the system. 1=US transducer, 2=optical monitoring system, 3=sample, 4=acoustically-reflective/optically transparent element, 5=acoustic absorber, 6= tank filled with deionized water, 8=linear rail, 9=locking system for the transducer, 10=control system, 11=signal generator and amplifier, 12=motorized system, 13=fluidic system.*

The key element of the system is the acoustically reflective / optically transparent element .It is placed at 45° with respect to the axis of the ultrasonic beam propagation, allowing a perpendicular impact of the US on the target; the optical monitoring system is placed in axis with respect to the sample instead allowing the visualization of the target in real-time (in bright field or fluorescence, depending on the application).

The system is designed to be extremely flexible, with the possibility to easily interchange different US transducers and different optical monitoring systems.

The sample holder, represented in Figure A.7 consists of one or more wells containing the samples. The sample holder is isolated / sealed via two thin membranes that minimally interfere with the acoustic wave.

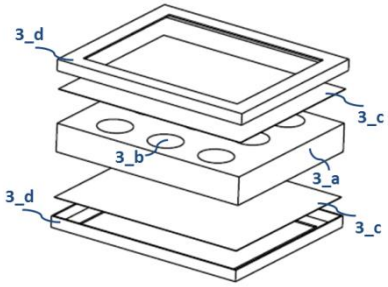

Figure A.7. *Sample holder (3_a) containing one or more wells (3_b) containing the samples. The sample holder is isolated / sealed by two thin membranes (3_c) attached to the holder by means of two cups (3_d).*

Bibliography

[1] Wickham J. The new surgery. Br Med J (Clin Res Ed) 1987;295:1581.
[2] Baltayiannis N, Michail C, Lazaridis G, Anagnostopoulos D, Baka S, Mpoukovinas I, et al. Minimally invasive procedures. Annals of translational medicine 2015;3.
[3] Dario P, Hannaford B, Menciassi A. Smart surgical tools and augmenting devices. Robotics and Automation, IEEE Transactions on 2003;19:782-92.
[4] Foley JL, Eames M, Snell J, Hananel A, Kassell N, Aubry J-F. Image-guided focused ultrasound: state of the technology and the challenges that lie ahead. Imaging Med 2013;5:357-70.
[5] Leskinen JJ, Hynynen K. Study of factors affecting the magnitude and nature of ultrasound exposure with in vitro set-ups. Ultrasound Med Biol 2012;38:777-94.
[6] ter Haar G, Shaw A, Pye S, Ward B, Bottomley F, Nolan R, et al. Guidance on reporting ultrasound exposure conditions for bio-effects studies. Ultrasound Med Biol 2011;37:177-83.
[7] Hill CR, Bamber JC, Haar G. Physical Principles of Medical Ultrasonics, second ed.: Wiley Online Library; 2004.
[8] www.fusfoundation.org. An Overview of the Biological Effects of Focused Ultrasound. 2015.
[9] Hsiao Y-H, Kuo S-J, Tsai H-D, Chou M-C, Yeh G-P. Clinical Application of High-intensity Focused Ultrasound in Cancer Therapy. J Cancer 2016;7:225.
[10] Crum L, Bailey M, Kaczkowski P, Makin I, Mourad P, Beach K, et al. Therapeutic ultrasound: A promising future in clinical medicine. Acoustical Society of America University of Washington 2005;21.
[11] Wissler EH. Pennes' 1948 paper revisited. J Appl Physiol 1998;85:35-41.
[12] Sapareto SA, Dewey WC. Thermal dose determination in cancer therapy. International Journal of Radiation Oncology* Biology* Physics 1984;10:787-800.
[13] Suslick KS. Ultrasound: its chemical, physical, and biological effects: VCH Publishers; 1988.
[14] Cravotto G, Gaudino EC, Cintas P. On the mechanochemical activation by ultrasound. Chem Soc Rev 2013;42:7521-34.
[15] Fix SM, Borden MA, Dayton PA. Therapeutic gas delivery via microbubbles and liposomes. J Control Release 2015;209:139-49.
[16] Nelson TR, Fowlkes JB, Abramowicz JS, Church CC. Ultrasound biosafety considerations for the practicing sonographer and sonologist. J Ultrasound Med 2009;28:139.
[17] Ter Haar G. Safety and bio-effects of ultrasound contrast agents. Med Biol Eng Comput 2009;47:893-900.
[18] Moros E. Physics of thermal therapy: fundamentals and clinical applications: Taylor & Francis; 2012.
[19] Roberts WW, Hall TL, Ives K, Wolf JS, Fowlkes JB, Cain CA. Pulsed cavitational ultrasound: a noninvasive technology for controlled tissue ablation (histotripsy) in the rabbit kidney. The Journal of urology 2006;175:734-8.
[20] Mindjuk I, Trumm CG, Herzog P, Stahl R, Matzko M. MRI predictors of clinical success in MR-guided focused ultrasound (MRgFUS) treatments of uterine fibroids: results from a single centre. Eur Radiol 2015;25:1317-28.
[21] Uri Rosenschein MVF, PhD; Efim Kerner, MSc; Itzchak Fabian, MSc;, Joelle Bernheim MYE, PhD. Ultrasound Imaging–Guided Noninvasive Ultrasound Thrombolysis. 2013.
[22] Hersh DS, Kim AJ, Winkles JA, Eisenberg HM, Woodworth GF, Frenkel V. Emerging applications of therapeutic ultrasound in neuro-oncology: moving beyond tumor ablation. Neurosurgery 2016;79:643-54.

[23] Leinenga G, Langton C, Nisbet R, Götz J. Ultrasound treatment of neurological diseases [mdash] current and emerging applications. Nature Reviews Neurology 2016;12:161-74.
[24] Brown SA, Greenbaum L, Shtukmaster S, Zadok Y, Ben-Ezra S, Kushkuley L. Characterization of nonthermal focused ultrasound for noninvasive selective fat cell disruption (lysis): technical and preclinical assessment. Plast Reconstr Surg 2009;124:92-101.
[25] Baker KG, Robertson VJ, Duck FA. A review of therapeutic ultrasound: biophysical effects. Phys Ther 2001;81:1351.
[26] Wang S, Zderic V, Frenkel V. Extracorporeal, low-energy focused ultrasound for noninvasive and nondestructive targeted hyperthermia. Future Oncology 2010;6:1497-511.
[27] Apfel R. Acoustic cavitation: a possible consequence of biomedical uses of ultrasound. The British journal of cancer Supplement 1982;5:140.
[28] Liang H, Tang J, Halliwell M. Sonoporation, drug delivery, and gene therapy. Proceedings of the Institution of Mechanical Engineers, Part H: Journal of Engineering in Medicine 2010;224:343-61.
[29] González-Mariscal L, Nava P, Hernandez S. Critical role of tight junctions in drug delivery across epithelial and endothelial cell layers. The Journal of membrane biology 2005;207:55-68.
[30] Yang F-Y, Chiu W-H, Liu S-H, Lin G-L, Ho F-M. Functional changes in arteries induced by pulsed high-intensity focused ultrasound. IEEE transactions on ultrasonics, ferroelectrics, and frequency control 2009;56:2643-9.
[31] Tufail Y, Yoshihiro A, Pati S, Li MM, Tyler WJ. Ultrasonic neuromodulation by brain stimulation with transcranial ultrasound. Nat Protoc 2011;6:1453-70.
[32] Kampinga HH. Cell biological effects of hyperthermia alone or combined with radiation or drugs: a short introduction to newcomers in the field. Int J Hyperthermia 2006;22:191-6.
[33] Xu Z, Fowlkes JB, Rothman ED, Levin AM, Cain CA. Controlled ultrasound tissue erosion: The role of dynamic interaction between insonation and microbubble activity. The Journal of the Acoustical Society of America 2005;117:424-35.
[34] Kutty S, Xie F, Gao S, Drvol LK, Lof J, Fletcher SE, et al. Sonothrombolysis of intra-catheter aged venous thrombi using microbubble enhancement and guided three-dimensional ultrasound pulses. Journal of the American Society of Echocardiography 2010;23:1001-6.
[35] Böhmer M, Chlon C, Raju B, Chin C, Shevchenko T, Klibanov A. Focused ultrasound and microbubbles for enhanced extravasation. J Control Release 2010;148:18-24.
[36] Sirsi SR, Borden MA. State-of-the-art materials for ultrasound-triggered drug delivery. Adv Drug Del Rev 2013.
[37] Ricotti L, Cafarelli A, Iacovacci V, Vannozzi L, Menciassi A. Advanced micro-nano-bio systems for future targeted therapies. Current Nanoscience 2015;11:144-60.
[38] Ciofani G, Menciassi A. Piezoelectric nanomaterials for biomedical applications: Springer; 2012.
[39] Martin E. The Cellular Bioeffects of Low Intensity Ultrasound. Ultrasound 2009;17:214-9.
[40] Langer R, Tirrell DA. Designing materials for biology and medicine. Nature 2004;428:487-92.
[41] Culjat MO, Goldenberg D, Tewari P, Singh RS. A review of tissue substitutes for ultrasound imaging. Ultrasound Med Biol 2010;36:861-73.
[42] Zell K, Sperl J, Vogel M, Niessner R, Haisch C. Acoustical properties of selected tissue phantom materials for ultrasound imaging. Phys Med Biol 2007;52:N475.
[43] Doan N, Reher P, Meghji S, Harris M. In vitro effects of therapeutic ultrasound on cell proliferation, protein synthesis, and cytokine production by human fibroblasts, osteoblasts, and monocytes. J Oral Maxillofac Surg 1999;57:409-19.
[44] Thakurta SG, Kraft M, Viljoen HJ, Subramanian A. Enhanced depth-independent chondrocyte proliferation and phenotype maintenance in an ultrasound bioreactor and an assessment of ultrasound dampening in the scaffold. Acta Biomater 2014;10:4798-810.

[45] Ciofani G, Danti S, D'Alessandro D, Ricotti L, Moscato S, Bertoni G, et al. Enhancement of neurite outgrowth in neuronal-like cells following boron nitride nanotube-mediated stimulation. ACS nano 2010;4:6267-77.
[46] Ricotti L, Fujie T, Vazão H, Ciofani G, Marotta R, Brescia R, et al. Boron nitride nanotube-mediated stimulation of cell co-culture on micro-engineered hydrogels. PLoS One 2013;8:e71707.
[47] Cafarelli A, Miloro P, Verbeni A, Carbone M, Menciassi A. Speed of sound in rubber-based materials for ultrasonic phantoms. Journal of Ultrasound 2016:1-6.
[48] Duck FA. Physical properties of tissues: a comprehensive reference book: London: Academic Press, San Diego; 1990.
[49] Tsou JK, Liu J, Barakat AI, Insana MF. Role of ultrasonic shear rate estimation errors in assessing inflammatory response and vascular risk. Ultrasound Med Biol 2008;34:963-72.
[50] Prokop AF, Vaezy S, Noble ML, Kaczkowski PJ, Martin RW, Crum LA. Polyacrylamide gel as an acoustic coupling medium for focused ultrasound therapy. Ultrasound Med Biol 2003;29:1351-8.
[51] Dabbagh A, Abdullah BJJ, Ramasindarum C, Kasim NHA. Tissue-mimicking gel phantoms for thermal therapy studies. Ultrason Imaging 2014;36:291-316.
[52] Choi MJ, Guntur SR, Lee KI, Paeng DG, Coleman A. A Tissue Mimicking Polyacrylamide Hydrogel Phantom for Visualizing Thermal Lesions Generated by High Intensity Focused Ultrasound. Ultrasound Med Biol 2013;39:439-48.
[53] Lafon C, Zderic V, Noble ML, Yuen JC, Kaczkowski PJ, Sapozhnikov OA, et al. Gel phantom for use in high-intensity focused ultrasound dosimetry. Ultrasound Med Biol 2005;31:1383-9.
[54] Cafarelli A, Mura M, Diodato A, Schiappacasse A, Santoro M, Ciuti G, et al. A computer-assisted robotic platform for Focused Ultrasound Surgery: Assessment of high intensity focused ultrasound delivery. Engineering in Medicine and Biology Society (EMBC), 2015 37th Annual International Conference of the IEEE: IEEE; 2015. p. 1311-4.
[55] Madsen EL, Zagzebski JA, Banjavie RA, Jutila RE. Tissue mimicking materials for ultrasound phantoms. Med Phys 1978;5:391-4.
[56] Burlew MM, Madsen EL, Zagzebski JA, Banjavic RA, Sum SW. A new ultrasound tissue-equivalent material. Radiology 1980;134:517-20.
[57] Cannon LM, Fagan AJ, Browne JE. Novel tissue mimicking materials for high frequency breast ultrasound phantoms. Ultrasound Med Biol 2011;37:122-35.
[58] Browne J, Ramnarine K, Watson A, Hoskins P. Assessment of the acoustic properties of common tissue-mimicking test phantoms. Ultrasound Med Biol 2003;29:1053-60.
[59] Ross K, Pyrak-Nolte L, Campanella O. The effect of mixing conditions on the material properties of an agar gel—microstructural and macrostructural considerations. Food Hydrocolloids 2006;20:79-87.
[60] Palchesko RN, Zhang L, Sun Y, Feinberg AW. Development of polydimethylsiloxane substrates with tunable elastic modulus to study cell mechanobiology in muscle and nerve. PLoS One 2012;7:e51499.
[61] Genchi GG, Ciofani G, Liakos I, Ricotti L, Ceseracciu L, Athanassiou A, et al. A straightforward method for obtaining long term PDMS/muscle cell biohybrid constructs. Colloids Surf B Biointerfaces 2013;105:144-51.
[62] Wang P-Y, Tsai W-B, Voelcker NH. Screening of rat mesenchymal stem cell behaviour on polydimethylsiloxane stiffness gradients. Acta Biomater 2012;8:519-30.
[63] Engler AJ, Griffin MA, Sen S, Bönnemann CG, Sweeney HL, Discher DE. Myotubes differentiate optimally on substrates with tissue-like stiffness pathological implications for soft or stiff microenvironments. The Journal of cell biology 2004;166:877-87.
[64] Engler AJ, Sen S, Sweeney HL, Discher DE. Matrix elasticity directs stem cell lineage specification. Cell 2006;126:677-89.

[65] Ulrich TA, Jain A, Tanner K, MacKay JL, Kumar S. Probing cellular mechanobiology in three-dimensional culture with collagen–agarose matrices. Biomaterials 2010;31:1875-84.
[66] Mendes SF, Costa CM, Caparrós C, Sencadas V, Lanceros-Méndez S. Effect of filler size and concentration on the structure and properties of poly (vinylidene fluoride)/BaTiO3 nanocomposites. Journal of Materials Science 2012;47:1378-88.
[67] Huang X, Xie L, Hu Z, Jiang P. Influence of BaTiO 3 nanoparticles on dielectric, thermophysical and mechanical properties of ethylene-vinyl acetate elastomer/BaTiO 3 microcomposites. IEEE Transactions on Dielectrics and Electrical Insulation 2011;18:375-83.
[68] Galasso FS, Kestigan M. Barium Titanate, BaTiO3. Inorganic Syntheses: Nonmolecular Solids, Volume 30 1973:111-2.
[69] Ciofani G, Ricotti L, Canale C, D'Alessandro D, Berrettini S, Mazzolai B, et al. Effects of barium titanate nanoparticles on proliferation and differentiation of rat mesenchymal stem cells. Colloids Surf B Biointerfaces 2013;102:312-20.
[70] Bamber J. Attenuation and absorption. Physical Principles of Medical Ultrasonics, Second Edition 2005:93-166.
[71] Marczak W. Water as a standard in the measurements of speed of sound in liquids. J Acoust Soc Am 1997;102:2776-9.
[72] He P. Determination of ultrasonic parameters based on attenuation and dispersion measurements. Ultrason Imaging 1998;20:275-87.
[73] Timme R. Speed of sound in castor oil. J Acoust Soc Am 1972;52:989-92.
[74] Dunn F, Edmonds P, Fry W. Absorption and dispersion of ultrasound in biological media. Biological engineering 1969;205:332.
[75] Zaleska-DorobiszA U, KaczorowskiB K, PawluśB A, PuchalskaB A, InglotB M. Ultrasound elastography–review of techniques and its clinical applications. Brain 2013;6:10-4.
[76] Whittaker S, Lethbridge G, Kim C, Keon Cohen Z, Ng I. An ultrasound needle insertion guide in a porcine phantom model. Anaesthesia 2013;68:826-9.
[77] Leibinger A, Forte AE, Tan Z, Oldfield MJ, Beyrau F, Dini D, et al. Soft Tissue Phantoms for Realistic Needle Insertion: A Comparative Study. Ann Biomed Eng 2015:1-11.
[78] Discher DE, Janmey P, Wang Y-l. Tissue cells feel and respond to the stiffness of their substrate. Science 2005;310:1139-43.
[79] Her GJ, Wu H-C, Chen M-H, Chen M-Y, Chang S-C, Wang T-W. Control of three-dimensional substrate stiffness to manipulate mesenchymal stem cell fate toward neuronal or glial lineages. Acta Biomater 2013;9:5170-80.
[80] Ricotti L, Menciassi A. Engineering stem cells for future medicine. Biomedical Engineering, IEEE Transactions on 2013;60:727-34.
[81] Callister WD, Rethwisch DG. Materials science and engineering: an introduction: Wiley New York; 2007.
[82] Zhang D, Gong X-F. Experimental investigation of the acoustic nonlinearity parameter tomography for excised pathological biological tissues. Ultrasound Med Biol 1999;25:593-9.
[83] Mueller S, Sandrin L. Liver stiffness: a novel parameter for the diagnosis of liver disease. Hepat Med 2010;2:49-67.
[84] Tchelepi H, Ralls PW, Radin R, Grant E. Sonography of diffuse liver disease. J Ultrasound Med 2002;21:1023-32.
[85] Arda K, Ciledag N, Aktas E, Arıbas BK, Köse K. Quantitative assessment of normal soft-tissue elasticity using shear-wave ultrasound elastography. Am J Roentgenol 2011;197:532-6.
[86] Sartori S, Chiono V, Tonda-Turo C, Mattu C, Gianluca C. Biomimetic polyurethanes in nano and regenerative medicine. Journal of Materials Chemistry B 2014;2:5128-44.
[87] Shaw A, ter Haar GR. Telling it like it is. Journal of therapeutic ultrasound 2013;1:1.
[88] Ter Haar G. Basic physics of therapeutic ultrasound. Physiotherapy 1978;64:100.

[89] de Oliveira RF, Oliveira D, Soares CP. Effect of low-intensity pulsed ultrasound on l929 fibroblasts. Arch Med Sci 2011;7:224-9.
[90] Ciofani G, Danti S, Ricotti L, D'Alessandro D, Moscato S, Mattoli V. Applications of piezoelectricity in nanomedicine. Piezoelectric nanomaterials for biomedical applications: Springer; 2012. p. 213-38.
[91] Genchi GG, Marino A, Grillone A, Pezzini I, Ciofani G. Remote Control of Cellular Functions: The Role of Smart Nanomaterials in the Medicine of the Future. Advanced Healthcare Materials 2017.
[92] Marino A, Barsotti J, de Vito G, Filippeschi C, Mazzolai B, Piazza V, et al. Two-photon lithography of 3D nanocomposite piezoelectric scaffolds for cell stimulation. ACS applied materials & interfaces 2015;7:25574-9.
[93] Marino A, Arai S, Hou Y, Sinibaldi E, Pellegrino M, Chang Y-T, et al. Piezoelectric Nanoparticle-Assisted Wireless Neuronal Stimulation. ACS nano 2015;9:7678-89.
[94] Ciofani G, Ricotti L, Mattoli V. Preparation, characterization and in vitro testing of poly (lactic-co-glycolic) acid/barium titanate nanoparticle composites for enhanced cellular proliferation. Biomed Microdevices 2011;13:255-66.
[95] Genchi GG, Ceseracciu L, Marino A, Labardi M, Marras S, Pignatelli F, et al. P (VDF-TrFE)/BaTiO3 Nanoparticle Composite Films Mediate Piezoelectric Stimulation and Promote Differentiation of SH-SY5Y Neuroblastoma Cells. Advanced Healthcare Materials 2016.
[96] Ricotti L, das Neves RP, Ciofani G, Canale C, Nitti S, Mattoli V, et al. Boron nitride nanotube-mediated stimulation modulates F/G-actin ratio and mechanical properties of human dermal fibroblasts. J Nanopart Res 2014;16:1-14.
[97] Feril LB, Kondo T. Biological effects of low intensity ultrasound: the mechanism involved, and its implications on therapy and on biosafety of ultrasound. J Radiat Res (Tokyo) 2004;45:479-89.
[98] Padilla F, Puts R, Vico L, Guignandon A, Raum K. Stimulation of Bone Repair with Ultrasound. Therapeutic Ultrasound: Springer; 2016. p. 385-427.
[99] Khanna A, Nelmes RT, Gougoulias N, Maffulli N, Gray J. The effects of LIPUS on soft-tissue healing: a review of literature. Br Med Bull 2009;89:169-82.
[100] Xin Z, Lin G, Lei H, Lue TF, Guo Y. Clinical applications of low-intensity pulsed ultrasound and its potential role in urology. Translational andrology and urology 2016;5:255.
[101] Urita A, Iwasaki N, Kondo M, Nishio Y, Kamishima T, Minami A. Effect of low-intensity pulsed ultrasound on bone healing at osteotomy sites after forearm bone shortening. The Journal of hand surgery 2013;38:498-503.
[102] Ikai H, Tamura T, Watanabe T, Itou M, Sugaya A, Iwabuchi S, et al. Low-intensity pulsed ultrasound accelerates periodontal wound healing after flap surgery. J Periodontal Res 2008;43:212-6.
[103] Nakao J, Fujii Y, Kusuyama J, Bandow K, Kakimoto K, Ohnishi T, et al. Low-intensity pulsed ultrasound (LIPUS) inhibits LPS-induced inflammatory responses of osteoblasts through TLR4–MyD88 dissociation. Bone 2014;58:17-25.
[104] Sarvazyan AP, Rudenko OV, Nyborg WL. Biomedical applications of radiation force of ultrasound: historical roots and physical basis. Ultrasound Med Biol 2010;36:1379-94.
[105] Žauhar G, Duck F, Starritt H. Comparison of the acoustic streaming in amniotic fluid and water in medical ultrasonic beams. Ultraschall in der Medizin-European Journal of Ultrasound 2006;28:152-8.
[106] Alassaf A, Aleid A, Frenkel V. In vitro methods for evaluating therapeutic ultrasound exposures: present-day models and future innovations. Journal of Therapeutic Ultrasound 2013;1:21.

[107] Sena K, Leven RM, Mazhar K, Sumner DR, Virdi AS. Early gene response to low-intensity pulsed ultrasound in rat osteoblastic cells. Ultrasound Med Biol 2005;31:703-8.
[108] Katiyar A, Duncan RL, Sarkar K. Ultrasound stimulation increases proliferation of MC3T3-E1 preosteoblast-like cells. Journal of Therapeutic Ultrasound 2014;2:1-10.
[109] Yddal T, Cochran S, Gilja OH, Postema M, Kotopoulis S. Open-source, high-throughput ultrasound treatment chamber. Biomedical Engineering/Biomedizinische Technik 2015;60:77-87.
[110] Salgarella AR, Cafarelli A, Ricotti L, Capineri L, Dario P, Menciassi A. Optimal Ultrasound Exposure Conditions for Maximizing C2C12 Muscle Cell Proliferation and Differentiation. Ultrasound Med Biol 2017.
[111] Razavi B, Behzad R. RF microelectronics: Prentice Hall New Jersey; 1998.
[112] Capineri L. A 15 MHz bandwidth, 60 Vpp, low distortion power amplifier for driving high power piezoelectric transducers. Rev Sci Instrum 2014;85:104701.
[113] Miloro P. Development of non-invasive technologies for biomedical applications in the vascular system PhD Programme in BioRobotics, Scuola Superiore Sant'Anna; 11th September 2014.
[114] Yaffe D, Saxel O. Serial passaging and differentiation of myogenic cells isolated from dystrophic mouse muscle. Nature 1977;270:725-7.
[115] Puts R, Ruschke K, Kadow-Romacker A, Hwang S, Jenderka K-V, Knaus P, et al. Mechanosensitive response of murine C2C12 myoblasts to focused Low-Intensity Pulsed Ultrasound (FLIPUS) stimulation. Ultrasonic Characterization of Bone (ESUCB), 2015 6th European Symposium on: IEEE; 2015. p. 1-4.
[116] Puts R, Rikeit P, Ruschke K, Kadow-Romacker A, Hwang S, Jenderka K-V, et al. Activation of Mechanosensitive Transcription Factors in Murine C2C12 Mesenchymal Precursors by Focused Low-Intensity Pulsed Ultrasound (FLIPUS). 2016.
[117] Lin G, Reed-Maldonado AB, Lin M, Xin Z, Lue TF. Effects and Mechanisms of Low-Intensity Pulsed Ultrasound for Chronic Prostatitis and Chronic Pelvic Pain Syndrome. International Journal of Molecular Sciences 2016;17:1057.
[118] Duffy RM, Sun Y, Feinberg AW. Understanding the role of ECM protein composition and geometric micropatterning for engineering human skeletal muscle. Ann Biomed Eng 2016:1-14.
[119] Ricotti L, Polini A, Genchi GG, Ciofani G, Iandolo D, Vazao H, et al. Proliferation and skeletal myotube formation capability of C2C12 and H9c2 cells on isotropic and anisotropic electrospun nanofibrous PHB scaffolds. Biomedical Materials 2012;7:035010.
[120] Boonen KJ, Langelaan ML, Polak RB, van der Schaft DW, Baaijens FP, Post MJ. Effects of a combined mechanical stimulation protocol: value for skeletal muscle tissue engineering. J Biomech 2010;43:1514-21.
[121] Fujita H, Nedachi T, Kanzaki M. Accelerated de novo sarcomere assembly by electric pulse stimulation in C2C12 myotubes. Exp Cell Res 2007;313:1853-65.
[122] Abrunhosa VM, Soares CP, Possidonio ACB, Alvarenga AV, Costa-Felix RP, Costa ML, et al. Induction of Skeletal Muscle Differentiation In Vitro by Therapeutic Ultrasound. Ultrasound Med Biol 2014;40:504-12.
[123] Ikeda K, Takayama T, Suzuki N, Shimada K, Otsuka K, Ito K. Effects of low-intensity pulsed ultrasound on the differentiation of C2C12 cells. Life Sci 2006;79:1936-43.
[124] Wu Z, Woodring PJ, Bhakta KS, Tamura K, Wen F, Feramisco JR, et al. p38 and extracellular signal-regulated kinases regulate the myogenic program at multiple steps. Mol Cell Biol 2000;20:3951-64.
[125] Zetser A, Gredinger E, Bengal E. p38 mitogen-activated protein kinase pathway promotes skeletal muscle differentiation participation of the MEF2C transcription factor. J Biol Chem 1999;274:5193-200.

[126] Penn BH, Bergstrom DA, Dilworth FJ, Bengal E, Tapscott SJ. A MyoD-generated feed-forward circuit temporally patterns gene expression during skeletal muscle differentiation. Genes Dev 2004;18:2348-53.
[127] Porter GA, Makuck RF, Rivkees SA. Reduction in intracellular calcium levels inhibits myoblast differentiation. J Biol Chem 2002;277:28942-7.
[128] Nedachi T, Fujita H, Kanzaki M. Contractile C2C12 myotube model for studying exercise-inducible responses in skeletal muscle. American Journal of Physiology-Endocrinology and Metabolism 2008;295:E1191-E204.
[129] Burattini S, Ferri P, Battistelli M, Curci R, Luchetti F, Falcieri E. C2C12 murine myoblasts as a model of skeletal muscle development: morpho-functional characterization. European journal of histochemistry: EJH 2004;48:223.
[130] Fisher BD, Hiller CM, Rennie SG. A comparison of continuous ultrasound and pulsed ultrasound on soft tissue injury markers in the rat. Journal of Physical Therapy Science 2003;15:65-70.
[131] Matsumoto Y, Nakano J, Oga S, Kataoka H, Honda Y, Sakamoto J, et al. The non-thermal effects of pulsed ultrasound irradiation on the development of disuse muscle atrophy in rat gastrocnemius muscle. Ultrasound Med Biol 2014;40:1578-86.
[132] Nagata K, Nakamura T, Fujihara S, Tanaka E. Ultrasound modulates the inflammatory response and promotes muscle regeneration in injured muscles. Ann Biomed Eng 2013;41:1095-105.
[133] Markert CD, Merrick MA, Kirby TE, Devor ST. Nonthermal ultrasound and exercise in skeletal muscle regeneration. Arch Phys Med Rehabil 2005;86:1304-10.
[134] Wilkin L, Merrick M, Kirby T, Devor S. Influence of therapeutic ultrasound on skeletal muscle regeneration following blunt contusion. Int J Sports Med 2004;25:73-7.
[135] Duck F. Acoustic properties of tissue at ultrasonic frequencies. Physical Properties of Tissue: A Comprehensive Reference Book 1990:73-124.
[136] Hynynen K, Edwards D. Temperature measurements during ultrasound hyperthermia. Med Phys 1989;16:618-26.
[137] Ter Haar G. Ultrasound bioeffects and safety. Proceedings of the Institution of Mechanical Engineers, Part H: Journal of Engineering in Medicine 2010;224:363-73.
[138] Morris H, Rivens I, Shaw A, ter Haar G. Investigation of the viscous heating artefact arising from the use of thermocouples in a focused ultrasound field. Phys Med Biol 2008;53:4759.
[139] Guo D, Cai K. Gelcasting of Ferroelectric Ceramics: Doping Effect and Further Development: INTECH Open Access Publisher; 2012.
[140] Khokhlova TD, Wang Y-N, Simon JC, Cunitz BW, Starr F, Paun M, et al. Ultrasound-guided tissue fractionation by high intensity focused ultrasound in an in vivo porcine liver model. Proceedings of the National Academy of Sciences 2014;111:8161-6.
[141] Tempany CM, McDannold NJ, Hynynen K, Jolesz FA. Focused ultrasound surgery in oncology: overview and principles. Radiology 2011;259:39-56.
[142] Lynn JG, Zwemer RL, Chick AJ, Miller AE. A new method for the generation and use of focused ultrasound in experimental biology. The Journal of general physiology 1942;26:179.
[143] Fry WJ, Mosberg Jr W, Barnard J, Fry F. Production of Focal Destructive Lesions in the Central Nervous System With Ultrasound*. J Neurosurg 1954;11:471-8.
[144] Silverman RH. Focused ultrasound in ophthalmology. Clinical Ophthalmology (Auckland, NZ) 2016;10:1865.
[145] Schlesinger D, Benedict S, Diederich C, Gedroyc W, Klibanov A, Larner J. MR-guided focused ultrasound surgery, present and future. Med Phys 2013;40:080901.
[146] Ebbini ES, Ter Haar G. Ultrasound-guided therapeutic focused ultrasound: Current status and future directions. Int J Hyperthermia 2015;31:77-89.

[147] Tyshlek D, Aubry J-F, ter Haar G, Hananel A, Foley J, Eames M, et al. Focused ultrasound development and clinical adoption: 2013 update on the growth of the field. J Ther Ultrasound 2014;2:2.
[148] Couture O, Foley J, Kassell NF, Larrat B, Aubry J-F. Review of ultrasound mediated drug delivery for cancer treatment: updates from pre-clinical studies. Translational Cancer Research 2014;3:494-511.
[149] Martin E, Jeanmonod D, Morel A, Zadicario E, Werner B. High-intensity focused ultrasound for noninvasive functional neurosurgery. Ann Neurol 2009;66:858-61.
[150] Bauer R, Martin E, Haegele-Link S, Kaegi G, von Specht M, Werner B. Noninvasive functional neurosurgery using transcranial MR imaging-guided focused ultrasound. Parkinsonism Relat Disord 2014;20:S197-S9.
[151] Wu F, Wang Z-B, Chen W-Z, Bai J, Zhu H, Qiao T-y. Preliminary experience using high intensity focused ultrasound for the treatment of patients with advanced stage renal malignancy. The Journal of urology 2003;170:2237-40.
[152] Siciliano B, Khatib O. Springer handbook of robotics: Springer; 2016.
[153] Qiu Z, Xie C, Cochran S, Corner G, Huang Z, Song C, et al. The development of a robotic approach to therapeutic ultrasound. Journal of Physics: Conference Series: IOP Publishing; 2009. p. 012017.
[154] Koizumi N, Funamoto T, Seo J, Lee D, Tsukihara H, Nomiya A, et al. A novel robust template matching method to track and follow body targets for NIUTS. Robotics and Automation (ICRA), 2014 IEEE International Conference on: IEEE; 2014. p. 1929-36.
[155] Seo J, Koizumi N, Mitsuishi M, Sugita N. Ultrasound image based visual servoing for moving target ablation by high intensity focused ultrasound. The International Journal of Medical Robotics and Computer Assisted Surgery 2016.
[156] Chanel L-A, Nageotte F, Vappou J, Luo J, Cuvillon L, de Mathelin M. Robotized High Intensity Focused Ultrasound (HIFU) system for treatment of mobile organs using motion tracking by ultrasound imaging: An in vitro study. Engineering in Medicine and Biology Society (EMBC), 2015 37th Annual International Conference of the IEEE: IEEE; 2015. p. 2571-5.
[157] Tognarelli S, Ciuti G, Diodato A, Cafarelli A, Menciassi A. Robotic Platform for High-Intensity Focused Ultrasound Surgery Under Ultrasound Tracking: The FUTURA Platform. Journal of Medical Robotics Research 2017:1740010.
[158] Palmeri ML, Miller ZA, Glass TJ, Garcia-Reyes K, Gupta RT, Rosenzweig SJ, et al. B-mode and acoustic radiation force impulse (ARFI) imaging of prostate zonal anatomy: Comparison with 3T T2-weighted MR imaging. Ultrason Imaging 2015;37:22-41.
[159] Ebbini ES, Yao H, Shrestha A. Dual-mode ultrasound phased arrays for image-guided surgery. Ultrason Imaging 2006;28:65-82.
[160] Dasgupta S, Wansapura J, Hariharan P, Pratt R, Witte D, Myers MR, et al. HIFU lesion volume as a function of sonication time, as determined by MRI, histology, and computations. J Biomech Eng 2010;132:081005.
[161] Muller A, Petrusca L, Auboiroux V, Valette P, Salomir R, Cotton F. Management of respiratory motion in extracorporeal high-intensity focused ultrasound treatment in upper abdominal organs: current status and perspectives. Cardiovasc Intervent Radiol 2013;36:1464-76.
[162] Chanel L-A, Nageotte F, Vappou J, Luo J, Cuvillon L. Robotized High Intensity Focused Ultrasound (HIFU) system for treatment of mobile organs using motion tracking by ultrasound imaging: An in vitro study.
[163] Kalal Z, Mikolajczyk K, Matas J. Tracking-learning-detection. IEEE transactions on pattern analysis and machine intelligence 2012;34:1409-22.

[164] Holbrook AB, Ghanouni P, Santos JM, Dumoulin C, Medan Y, Pauly KB. Respiration based steering for high intensity focused ultrasound liver ablation. Magn Reson Med 2014;71:797-806.
[165] Hynynen K, Chung A, Fjield T, Buchanan M, Daum D, Colucci V, et al. Feasibility of using ultrasound phased arrays for MRI monitored noninvasive surgery. IEEE transactions on ultrasonics, ferroelectrics, and frequency control 1996;43:1043-53.
[166] Hynynen K, McDannold N, Vykhodtseva N, Jolesz FA. Noninvasive MR Imaging–guided Focal Opening of the Blood-Brain Barrier in Rabbits 1. Radiology 2001;220:640-6.
[167] Focused Ultrasound Foundation. "Blood-brain barrier opened non-invasively with focused ultrasound for the first time." ScienceDaily. 9 November 2015. www.sciencedaily.com/releases/2015/11/151109085103.htm.
[168] Alonso A. Ultrasound-induced blood-brain barrier opening for drug delivery. Translational Neurosonology: Karger Publishers; 2014. p. 106-15.
[169] Tran N. Blood-Brain Barrier. Encyclopedia of Clinical Neuropsychology: Springer; 2011. p. 426-.
[170] Pardridge WM. The blood-brain barrier: bottleneck in brain drug development. NeuroRx 2005;2:3-14.
[171] Rodriguez A, Tatter SB, Debinski W. Neurosurgical techniques for disruption of the blood–brain barrier for glioblastoma treatment. Pharmaceutics 2015;7:175-87.
[172] Appelboom G, Detappe A, LoPresti M, Kunjachan S, Mitrasinovic S, Goldman S, et al. Stereotactic modulation of blood-brain barrier permeability to enhance drug delivery. Neuro Oncol 2016;18:1601-9.
[173] McDannold N, Vykhodtseva N, Jolesz FA, Hynynen K. MRI investigation of the threshold for thermally induced blood–brain barrier disruption and brain tissue damage in the rabbit brain. Magn Reson Med 2004;51:913-23.
[174] Sheikov N, McDannold N, Sharma S, Hynynen K. Effect of focused ultrasound applied with an ultrasound contrast agent on the tight junctional integrity of the brain microvascular endothelium. Ultrasound Med Biol 2008;34:1093-104.
[175] Konofagou EE, Tung Y-S, Choi J, Deffieux T, Baseri B, Vlachos F. Ultrasound-induced blood-brain barrier opening. Curr Pharm Biotechnol 2012;13:1332.
[176] Aryal M, Arvanitis CD, Alexander PM, McDannold N. Ultrasound-mediated blood–brain barrier disruption for targeted drug delivery in the central nervous system. Adv Drug Del Rev 2014;72:94-109.
[177] Magnin R, Rabusseau F, Salabartan F, Mériaux S, Aubry J-F, Le Bihan D, et al. Magnetic resonance-guided motorized transcranial ultrasound system for blood-brain barrier permeabilization along arbitrary trajectories in rodents. Journal of therapeutic ultrasound 2015;3:22.
[178] Burgess A, Dubey S, Yeung S, Hough O, Eterman N, Aubert I, et al. Alzheimer disease in a mouse model: MR imaging–guided focused ultrasound targeted to the hippocampus opens the blood-brain barrier and improves pathologic abnormalities and behavior. Radiology 2014;273:736-45.
[179] Liu H-L, Fan C-H, Ting C-Y, Yeh C-K. Combining microbubbles and ultrasound for drug delivery to brain tumors: current progress and overview. Theranostics 2014;4:432-44.
[180] Burgess A, Hynynen K. Microbubble-assisted ultrasound for drug delivery in the brain and central nervous system. Therapeutic Ultrasound: Springer; 2016. p. 293-308.
[181] Hynynen K, McDannold N, Vykhodtseva N, Raymond S, Weissleder R, Jolesz FA, et al. Focal disruption of the blood–brain barrier due to 260-kHz ultrasound bursts: a method for molecular imaging and targeted drug delivery. J Neurosurg 2006;105:445-54.

[182] Choi JJ, Pernot M, Small SA, Konofagou EE. Noninvasive, transcranial and localized opening of the blood-brain barrier using focused ultrasound in mice. Ultrasound Med Biol 2007;33:95-104.
[183] Samiotaki G, Konofagou EE. Dependence of the reversibility of focused-ultrasound-induced blood-brain barrier opening on pressure and pulse length in vivo. IEEE transactions on ultrasonics, ferroelectrics, and frequency control 2013;60:2257-65.
[184] Hynynen K, McDannold N, Sheikov NA, Jolesz FA, Vykhodtseva N. Local and reversible blood–brain barrier disruption by noninvasive focused ultrasound at frequencies suitable for trans-skull sonications. Neuroimage 2005;24:12-20.
[185] McDannold N, Vykhodtseva N, Raymond S, Jolesz FA, Hynynen K. MRI-guided targeted blood-brain barrier disruption with focused ultrasound: histological findings in rabbits. Ultrasound Med Biol 2005;31:1527-37.
[186] Aryal M, Fischer K, Gentile C, Gitto S, Zhang Y-Z, McDannold N. Effects on P-Glycoprotein Expression after Blood-Brain Barrier Disruption Using Focused Ultrasound and Microbubbles. PLoS One 2017;12:e0166061.
[187] Aubry J-F, Tanter M. MR-Guided transcranial focused ultrasound. Therapeutic Ultrasound: Springer; 2016. p. 97-111.
[188] Lipsman N, Schwartz ML, Huang Y, Lee L, Sankar T, Chapman M, et al. MR-guided focused ultrasound thalamotomy for essential tremor: a proof-of-concept study. The Lancet Neurology 2013;12:462-8.
[189] Dallapiazza R, McKisic MS, Shah B, Elias WJ. Neuromodulation for movement disorders. Neurosurg Clin N Am 2014;25:47-58.
[190] Marsac L, Larrat B, Pernot M, Robert B, Fink M, Aubry J, et al. Adaptive focusing of transcranial therapeutic ultrasound using MR Acoustic Radiation Force Imaging in a clinical environment. Ultrasonics Symposium (IUS), 2010 IEEE: IEEE; 2010. p. 991-4.
[191] Timbie KF, Mead BP, Price RJ. Drug and gene delivery across the blood–brain barrier with focused ultrasound. J Control Release 2015;219:61-75.
[192] Nyborg WL. Biological effects of ultrasound: development of safety guidelines. Part II: general review. Ultrasound Med Biol 2001;27:301-33.
[193] Deng J, Huang Q, Wang F, Liu Y, Wang Z, Wang Z, et al. The role of caveolin-1 in blood–brain barrier disruption induced by focused ultrasound combined with microbubbles. J Mol Neurosci 2012;46:677-87.
[194] Vykhodtseva N, McDannold N, Hynynen K. Progress and problems in the application of focused ultrasound for blood–brain barrier disruption. Ultrasonics 2008;48:279-96.
[195] Wu S-Y, Tung Y-S, Marquet F, Downs ME, Sanchez CS, Chen C, et al. Transcranial cavitation detection in primates during blood-brain barrier opening-a performance assessment study. IEEE transactions on ultrasonics, ferroelectrics, and frequency control 2014;61:966-78.
[196] Standard I. 61161 Ed. 2, Ultrasonics-Power measurement-Radiation force balances and performance requirements. International Electrotechnical Commission, Geneva 2006.
[197] Sutton Y, McBride K, Pye S. An ultrasound mini-balance for measurement of therapy level ultrasound. Phys Med Biol 2006;51:3397.
[198] Frigo M, Johnson SG. The design and implementation of FFTW3. Proc IEEE 2005;93:216-31.
[199] Arvanitis CD, Livingstone MS, Vykhodtseva N, McDannold N. Controlled ultrasound-induced blood-brain barrier disruption using passive acoustic emissions monitoring. PLoS One 2012;7:e45783.
[200] Saunders NR, Dziegielewska KM, Møllgård K, Habgood MD. Markers for blood-brain barrier integrity: how appropriate is Evans blue in the twenty-first century and what are the alternatives? Front Neurosci 2015;9:385.

[201] Kudo N, Okada K, Yamamoto K. Sonoporation by single-shot pulsed ultrasound with microbubbles adjacent to cells. Biophys J 2009;96:4866-76.
[202] Fan Z, Kumon RE, Deng CX. Mechanisms of microbubble-facilitated sonoporation for drug and gene delivery. Ther Deliv 2014;5:467-86.
[203] Inserra C, Labelle P, Der Loughian C, Lee J-L, Fouqueray M, Ngo J, et al. Monitoring and control of inertial cavitation activity for enhancing ultrasound transfection: The SonInCaRe project. IRBM 2014;35:94-9.
[204] Prentice P, Cuschieri A, Dholakia K, Prausnitz M, Campbell P. Membrane disruption by optically controlled microbubble cavitation. Nature Physics 2005;1:107-10.
[205] Cafarelli A, Ricotti L, Menciassi A. Italian patent: Sistema di stimolazione ad ultrasuoni di un campione in vitro, filing no. 102016000052583, filing date: May 2016.